NANOMATERIALS TO BIOSENSORS:

A BENCH-TOP RAPID PROTOTYPING APPROACH

A Dissertation

by

WEI-SSU LIAO

Submitted to the Office of Graduate Studies of
Texas A&M University
in partial fulfillment of the requirements for the degree of

DOCTOR OF PHILOSOPHY

May 2009

Major Subject: Chemistry

NANOMATERIALS TO BIOSENSORS:

A BENCH-TOP RAPID PROTOTYPING APPROACH

A Dissertation

by

WEI-SSU LIAO

Submitted to the Office of Graduate Studies of
Texas A&M University
in partial fulfillment of the requirements for the degree of

DOCTOR OF PHILOSOPHY

Approved by:

Chair of Committee,	Paul S. Cremer
Committee Members,	D. Wayne Goodman
	James D. Batteas
	Winfried Teizer
Head of Department,	David H. Russell

May 2009

Major Subject: Chemistry

ABSTRACT

Nanomaterials to Biosensors:

A Bench-top Rapid Prototyping Approach. (May 2009)

Wei-Ssu Liao, B.S., National Cheng Kung University, Taiwan;

M.S., National Taiwan University, Taiwan

Chair of Advisory Committee: Dr. Paul S. Cremer

Nanofabrication has received substantial interest from scientists and engineers because of its potential applications in many fields. This was because nanoscale structures have unique properties that cannot be observed or utilized at other size scales. Our living environment and many of our daily necessities had been strongly influenced by these techniques. Computers, electronics, housewares, vehicles, and medical care are now all affected by this explosive nanotechnology. However, traditional methods in controlling nanoscale features and their properties were often time-consuming and expensive. The objective of my research was to design, fabricate, and test nanostructure platforms using a unique toolbox of bottom-up lithographic techniques recently developed in our laboratory. These novel methods can be utilized for the rapid prototyping of nanoscale patterns in a much easier and more economical way. Specifically, we also focused on applying these nanoscale patterns as sensor platforms. These platforms were easily produced with our unique methods, and provide ultra sensitive capability to detect diverse chemical or biological species.

The demonstration of capabilities and applications of our unique technologies includes the following projects. Chapters II and III describe a simple, inexpensive, and rapid method for making metal nanoparticles ranging between 10 nm and 100 nm in size through metal photoreduction with templates. The process can be completed in approximately 11 minutes without the use of a clean room environment or vacuum techniques. A simple label-free biosensor fabrication method based on transmission localized surface plasmon resonance (T-LSPR) of this platform is also demonstrated. Chapters IV and V present a nanoscale patterning technique for creating diverse features in polymers and metals. The process works by combining evaporative ring staining with a colloidal templating process. Well-ordered hexagonally arrayed nanorings, double rings, triple rings, targets, and holes were all easily prepared. A line width as thin as ~15 nm can repeatably be performed with this technology. Finally, Chapter VI demonstrates an ultra-sensitive plasmonic optical device based on hexagonal periodic nanohole metal films produced through our evaporative templating technique. The optical properties of these sub-wavelength periodic hole array metal films are discussed.

ACKNOWLEDGEMENTS

I would like to thank my committee chair, Dr. Cremer, and my committee members, Dr. Goodman, Dr. Batteas, and Dr. Teizer, for their guidance and support throughout the course of this research.

Thanks also go to my friends and colleagues and the department faculty and staff for making my time at Texas A&M University a great experience.

Finally, thanks to my mother and father for their encouragement and love.

TABLE OF CONTENTS

LIST OF FIGURES

FIGURE Page

FIGURE Page

FIGURE Page

LIST OF TABLES

CHAPTER I

INTRODUCTION

Objective

Over the past ten to twenty years, nanotechnology has created a revolution at the forefront of human life. Many useful applications in our daily necessities have been strongly influenced by these techniques. From common electronics to complicated medical treatments, nanomaterial and nanofabrication are getting more and more involved. Based on unique properties that cannot be observed or utilized at other size scales, nanoscale structures have become important in lot of fascinating fields. The fabrication of nanomaterials and nanopatterning features has drawn considerable attention because of both fundamental interests and potential applications. [1-15] Scientists and engineers have been especially interested in the fabrication process gaining control over their size and geometry. This is because a well controlled nanostructure provides correct and useful information for its potential applications in many fields.[1-15] Therefore, tons of remarkable achievements in nanostructure fabrication have been demonstrated and utilized to achieve many special necessities.[16-28]

Depending on the exact size and shape of the intended materials, elaborate and time-consuming processes are often required to achieve highly uniform patterns. It should be noted that the current approaches for fabricating uniform nano-size features

---

This dissertation follows the style of *Journal of the American Chemical Society.*

often require sophisticated preparation, and relatively specialized equipments or environments. It is therefore desirable to design bench-top techniques that could be performed rapidly with minimal equipments and without specialized facilities. Furthermore, large scale production of highly uniform features is also required. In this research, we will introduce two simple, inexpensive, and rapid methods for making uniform sub 100 nm metal features. The overall objective of this study is to design bench-top techniques for nanomaterial fabrication, property examination, and study their prospective applications in biosensing based upon novel rapid-prototyping methods we developed.

Micro/Nano Fabrication

The central interest of micro/nano fabrication is focused on gaining control over feature size and geometry during the fabrication process. Conventionally, photolithographic methods provide a convenient route to fabricate precise structures down to the 100 nm scale.[21, 29, 30] In brief, a photomask with special features was first produced through traditional photography. A thin layer of UV-sensitive material (photoresist) was spun-coated on the flat substrate. The photomask was then carefully aligned on top of the photoresist coated substrate and the whole chip was exposed to a UV light. After treated with the developing solution, the features on the mask could be transferred to the photoresist layer. This photoresist layer was then used as a mold for transferring features to the underneath substrate or other interested platforms. The whole process is demonstrated in Figure 1.1.[30]

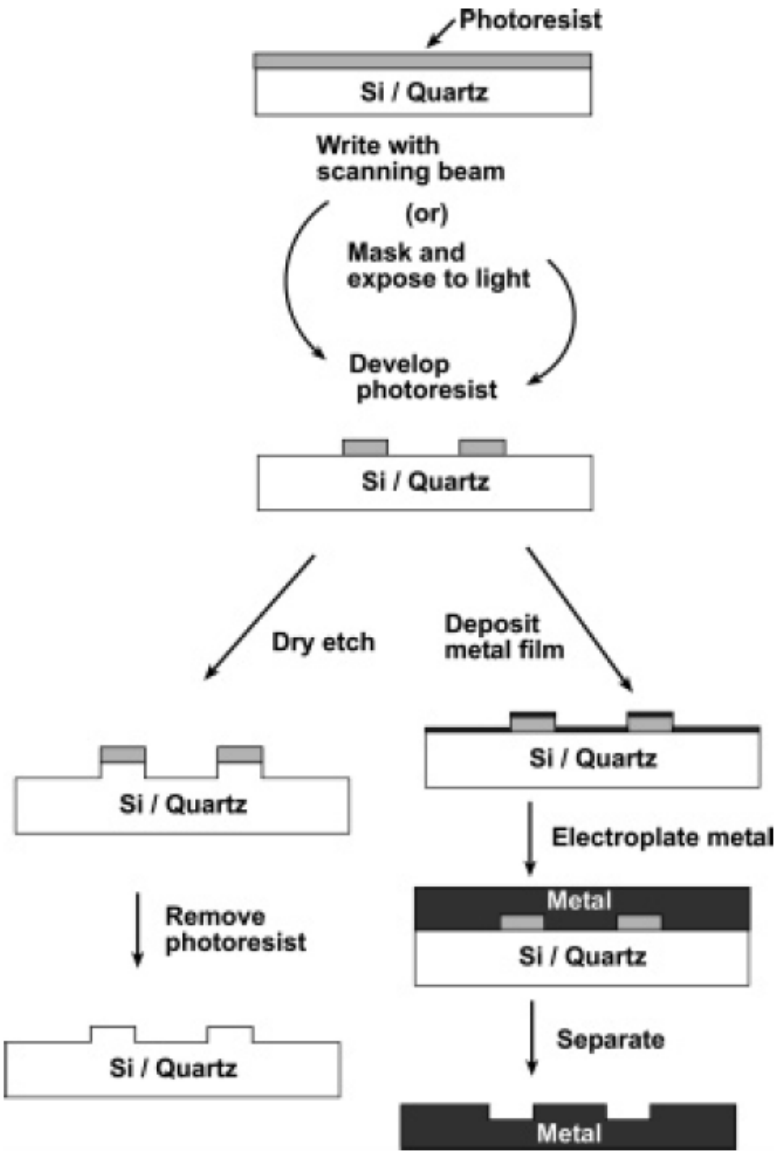

Figure 1.1. Schematic illustration of structure fabrication and transfer through conventional photo/e-beam lithography. The top image was adapted from reference 30.

Although photolithographic methods created a very useful route in fabricating micro/sub-micro features, the application of this technique is still restricted to the diffraction limit of light (100 nm). On the other hand, electron-beam lithography is able to fabricate features down to sub 100 nm scale.[30, 31] This technique relies on writing a mask directly into a polymer film on the substrate with an electron beam. The polymer layer with features can thereafter be used as a mold for transferring features to the underneath substrate or as a mask to deposit other material and then washed away, as demonstrate in Figure 1.1. This technique offers the advantage of creating arbitrary geometries, sizes, and spacing down to sub 100 nm.[30] Although such a high resolution can be reached, it is always time consuming to make large arrays. In addition, the expensive facility requirement restricts its applications.

Various synthetic methods have been used in past to prepare nearly monodisperse particles up to approximately 10 nm in diameter. [16, 17, 20, 25, 26] Moreover, chemical syntheses through changing the reaction conditions and the stabilizing surfactants successfully produced a diversity of structures such as nanocubes, nanoprisms, nanotriangles, tetrahedral, bipyrimids, nanostars, etc.[32-37]

There are, however, fewer methods for easily fabricating highly uniform feature arrays on an intermediate length scale. Previous fabrication efforts on the 10 to 100 nm scale have included reduction synthesis and nanolithography.[18, 19, 22, 23, 27, 28] Useful techniques such as extreme-UV lithography,[38, 39] interference lithography,[40-42] nanocontact printing,[43] and dip-pen nanolithography[44] could be used to reach this range at specific conditions.[21, 30] However, it should be noted that the approaches described

above often require sophisticated synthetic preparation, and/or relatively specialized equipments/environments.

In nanoscale fabrication, template-based techniques have provided a very simple and economical way to produce well controlled nanostructures.[28, 45-55] Useful templates such as nanospheres,[46-49, 52-54] nanoporous anodic aluminum oxide (AAO),[45, 50, 56] nanochannels,[51, 57] or nanoholes[55] were utilized to produce a diversity of nanostructures like nanorods,[58, 59] nanotubes,[50, 59-68] nanoelectrodes,[69] and nanoparticles.[70, 71]. These templates are also advantageous in terms of being inexpensive, convenient to use, comparably uniformity, and well-tunablity. They were typically combined with other techniques such as electrochemical deposition,[50, 55] chemical vapor deposition,[46-48] ion-beam bombardment,[51, 56] selective wetting,[52, 53] and edge spreading[49] methods to fabricate a large family of nanostructures. Large areas with minute features were therefore much easier to fabricate under the precise template confinement.

One example of these useful templating techniques is to utilize monodispersed polystyrene or silica spheres for fabricating nanostructures. A variety of interesting structures were made through this simple phenomenon.[46-49, 52-54] Nanosphere lithography (NSL) is one of the successful examples demonstrating the capability of applying self-assembly micro/nano spheres as templates for nanofabrication.[46, 47] In short, as demonstrated in Figure 1.2,[72] the uniform sphere suspension solution was applied to a clean substrate. As the solvent evaporate, the capillary force drew the spheres together and a self-assembled hexagonal close packing array was formed. This array was then used as a mask for fabricating different uniform nanostructures through metal deposition

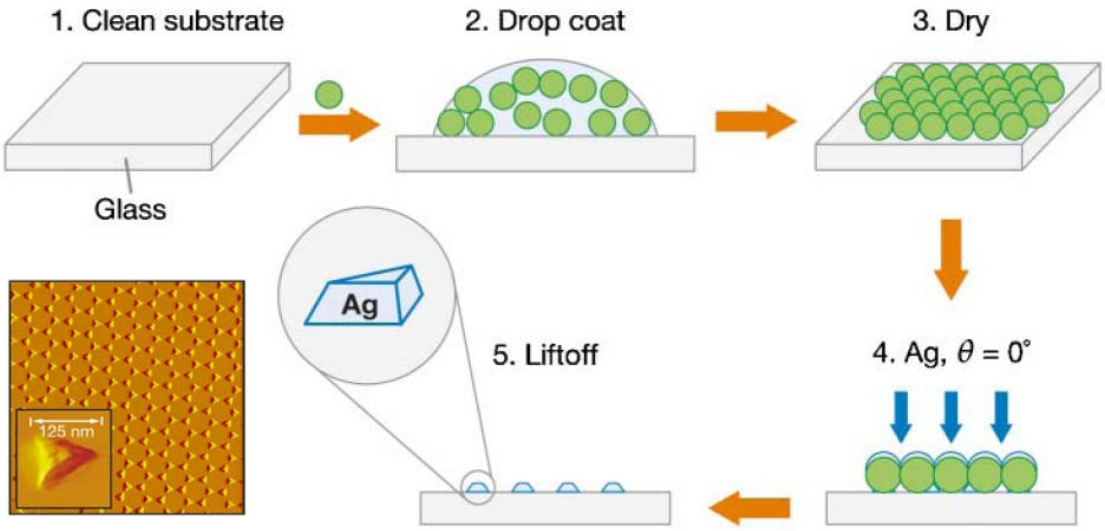

Figure 1.2. Schematic diagram of the example of templating technique: nanosphere lithography. The top image was adapted from reference 72.

and the following template lift-off process. Interesting nanostructures such as triangles or metal films over nanosphere (FON) could be easily performed by this technique.[3, 46, 47, 73, 74] Depending on the template size, nanostructures with different geometrical parameters could be easily produced. In the case of all naturally packing patterns, the nanosphere mask contains some common defects such as point defects (vacancies), line defects, and crystalline domains. The typical defect-free domain sizes are in the 10-100 μm range.[73] In addition to nanosphere lithography, techniques combining sphere templates and other methods such as shadow lithography,[48] edge spreading,[49] ion etching,[56] etc. were all successfully demonstrated in fabricating and studying interesting nanostructures. Furthermore, randomly packed spheres could also be used in manipulating other fascinating features such as nanorings, nanoholes, etc. which are known to show some fascinating optical and physical properties.[75-80]

Surface Plasmon Resonance (SPR)

Metal nanostructures possess many unique physical, electrical, optical, photonic, magnetic, and catalytical properties.[2-4, 6-8, 11, 13, 15, 73] These properties are strongly dependent on nanostructure material composition, geometrical parameters, and dimensions scale. One of the fascinating properties of nanostructures is called surface plasmon resonance (SPR). Surface plasmon resonance is a coherent oscillation of metal conduction electrons with the introduced electromagnetic wave. This phenomenon has been applied to a variety of applications such as chemical and biological sensing,[4, 73, 81-87] surface plasmon enhanced spectroscopies,[88-90] and lithographical fabrication.[91, 92] There

are two types of surface plasmons called propagating plasmon (plasmon polariton), and localized plasmon.[72] These two types of plasmons are demonstrated schematically in Figure 1.3.[72] In surface plasmon polaritons, plasmons propagate in the x and y directions along the metal-dielectric interface and decays evanescently in the z direction. In localized surface plasmons, the introduced light interacts with the particles which are much smaller than the light wavelength. A plasmon oscillating locally with the nanoparticles is therefore produced.[72] Both surface plasmon polariton and localized surface plasmon are sensitive to local dielectric environment changes. This leads to the application of surface plasmons in ultrasensitive chemical and biological sensing.[3, 4, 72, 73, 81, 93, 94]

Generally, surface plasmon polariton experiments were performed through smooth and thin films of Au or Ag with thickness in the range of 10-200 nm.[72, 73, 93] The interaction between the metal surface-confined electromagnetic wave and molecular surface layer was observed through angle, wavelength, or image modes.[73, 84] A 10-100 times field enhancement and ~1000 nm field spatial range were expected.[73, 93] On the other hand, localized surface plasmon resonance experiments were performed through 10-200 nm Au or Ag nanoparticles.[72, 73, 93] A 100-10000 times field enhancement and 10-50 nm spatial range were expected depending on particle geometries.[73, 93] Overall, surface plasmon polariton is more sensitive to the bulk refractive index changes. However, the much smaller sensing volume of localized surface plasmon resonance due to the much shorter (40-50 times) electromagnetic field decay length leads to

comparable response of these two techniques when measuring short range refractive index changes such as a molecular adsorption layer.[72, 93]

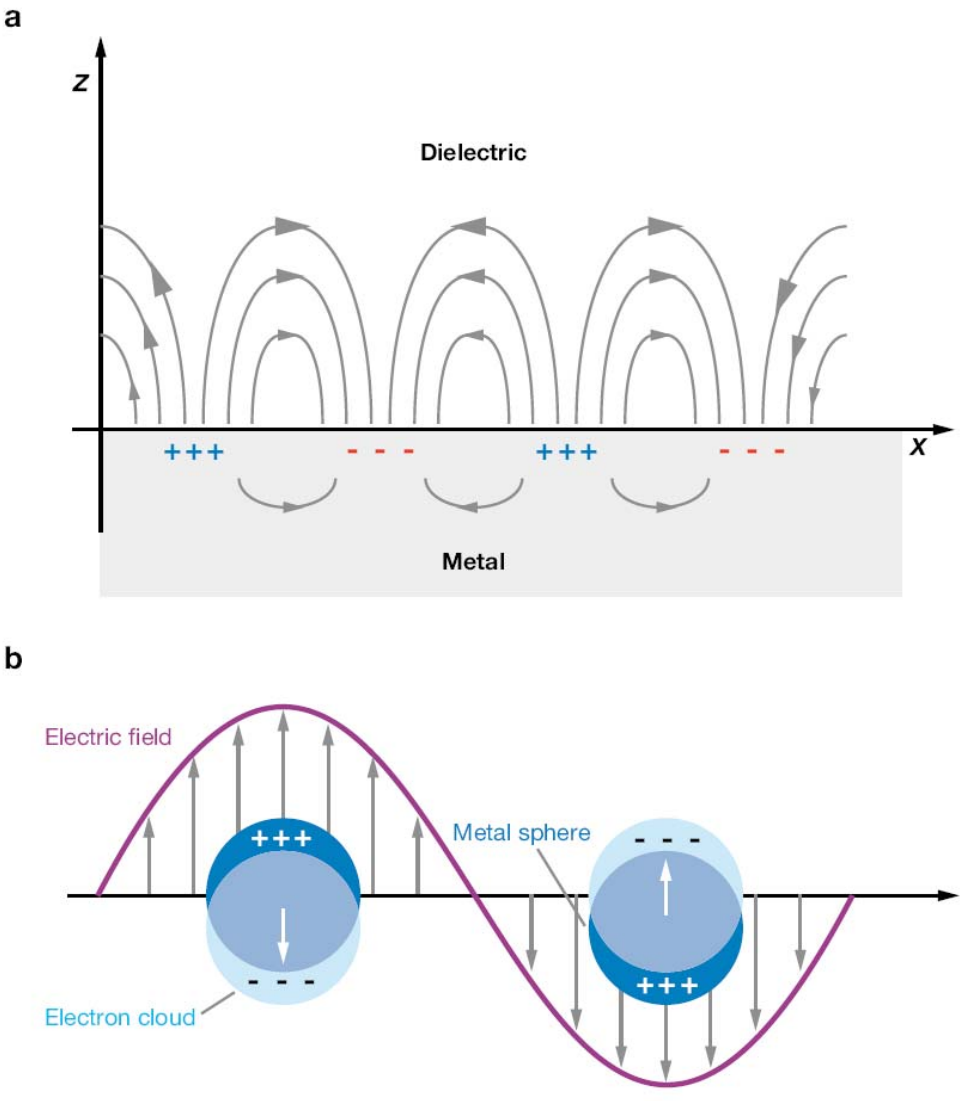

Figure 1.3. Schematic diagram of (a) surface plasmon polariton and (b) localized surface plasmon. The top image was adapted from reference 72.

Applications of Nanostructures

In the analytical chemistry field, nanoscale features have been widely used in biosensing because of their unique properties and size.[4, 72, 73, 81-87, 93, 94] An ideal biosensor should be very sensitive, highly selective, simple to fabricate, and easy to read. One unique property of these highly uniform nanofeature arrays is to be used as a platform for transmission localized surface plasmon resonance (T-LSPR) biosensors. A representative experimental setup and procedure is demonstrated in Figure 1.4.[94] The coherent oscillation between metal conduction electrons and the introduced electromagnetic wave can induce photon absorption and scattering, both of which are very sensitive to the dielectric properties of the surrounding medium.[82, 95] Through well control of nanostructure geometry, size, and composition, this plasmonic band could be adjusted to a wide range of wavelength.[72, 93, 96] This provides a variety of useful applications in photonics, electronics, optics, and biosensing. [1-15, 72, 73, 93] For a biosensor purpose, platforms can work in transmission mode whereby conduction electrons in the metal collectively oscillate when an electromagnetic wave is introduced through the sample. This technique is simpler to use than traditional SPR conducted in reflectance mode (Kretchmer geometry). This is because a planar LSPR sample can be directly placed into a standard UV-visible spectrometer to carry the absorption measurement. Several laboratories have reported successfully use of this technique for chemical and biological sensing to date.[4, 73, 81-87] Nevertheless, the sensing platforms fabrication is always elaborate, time consuming, and requires specialized equipments and/or environments. Therefore, it would be important to design a simple, inexpensive, and

rapid method for T-LSPR biosensor fabrication. Furthermore, techniques which maintain high sensitivity and specificity for protein detection are also required.

In addition to biosensor applications, intrinsic nanostructure properties are also a matter of interest among scientists. A better understanding of material properties on the nanoscale level could provide unknown new physical properties and related applications in the optical, material, electrical, chemical and biological sciences. In order to study these interesting phenomenon, nanofabrication techniques should afford precise control of structures and also provide high throughput efficiency. With the advancements in nanofabrication techniques, systematic studies of nanomaterial properties could be well examined and the potential applications could be better utilized.

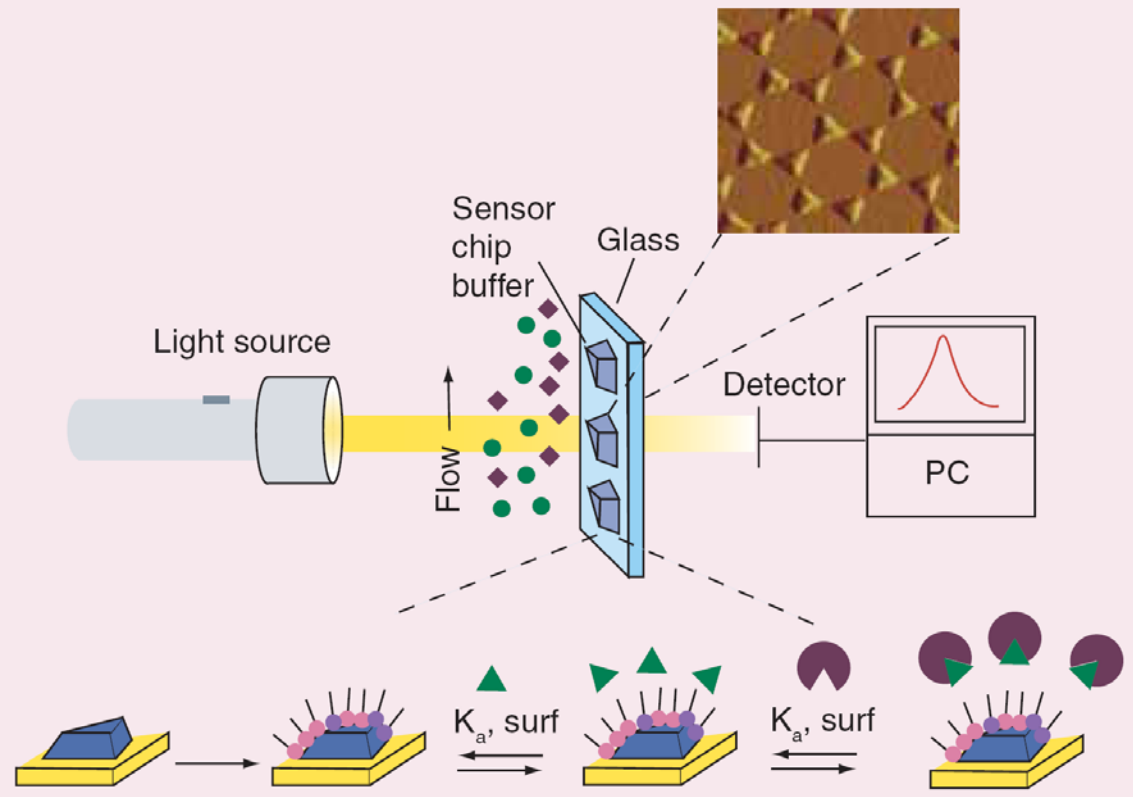

Figure 1.4. Schematic diagram of the example of localized surface plasmon resonance sensing. The top image was adapted from reference 94.

CHAPTER II

A RAPID PROTOTYPING APPROACH TO AG NANOPARTICLE FABRICATION IN THE 10-100 NM RANGE*

Introduction

Metal nanoparticles possess unique physical, magnetic, optical, electrical and catalytic properties.[2, 4, 11, 13, 15] Gaining control over their size and geometry during the fabrication process is of central interest. This has led to remarkable achievements in the preparation of nearly monodispersed particles up to ~10 nm in diameter by employing synthetic methods.[16, 17, 20, 25, 26] Moreover, photolithographic methods now make it possible to precisely control geometries down to the 100 nm scale.[19, 21, 24, 27] There are, however, fewer methods for easily fabricating highly uniform metal nanoparticle arrays on an intermediate length scale.

Previous fabrication efforts on the 10 to 100 nm scale have included reduction synthesis and nanolithography.[18, 22, 23, 28] Also, template approaches have been used to synthesize nanotubes,[50, 60-68] nanorods,[58, 59] nanoelectrodes,[69] and nanoparticles.[70, 71] Some of these techniques depend on wet electrochemical methods to deposit metal onto a uniform nanoporous template,[50, 59-61, 63-68] while others apply thermal or e-beam

*Reproduced with permission from "A Rapid Prototyping Approach to Ag Nanoparticle Fabrication in the 10-100 nm Range" by Liao, W. S.; Yang, T. L.; Castellana, E. T.; Kataota, S.; Cremer, P. S. *Advanced Materials,* **2006**, *18,* 2240-2243. Copyright 2006 John Wiley & Sons, Inc.

evaporation followed by etching procedures.[70, 71] Anodic aluminum oxide (AAO) templating has been widely exploited in these applications because of its uniformity, rigidity, and size controllable properties.

It should be noted that the approaches described above require a vacuum chamber for evaporating metal, a clean room environment, sophisticated preparation, relatively specialized equipment and/or etching steps. It was therefore deemed desirable to design a benchtop technique that could be performed rapidly with minimal equipment and without specialized facilities, while still achieving large arrays of highly uniform particles. Herein, a simple templating method is described for photoreducing metal from aqueous solutions onto TiO_2 thin films through a nanoporous filtration membrane.

TiO_2 has well-studied photocatalytic properties, which makes it an excellent choice for reducing metal ions from solution by UV illumination.[97, 98] Most often it has been used in the form of nanoparticles for reducing metal ions in solution.[99-102] More recently the process has been demonstrated with a thin TiO_2 film on a silica substrate.[103] In both cases the metal particles that are synthesized are typically 50 nm to 200 nm, where the average size can be tuned to some extent by the solution conditions. Although the particles are not monodispersed, it should be emphasized that the process can be performed under mild conditions (i.e. at room temperature in aqueous solution and neutral pH).

Experimental Section

Porous alumina filtration membrane templates were purchased from Synkera Technologies (Longmont, CO). The templates were 1.3 cm in diameter and 50 μm thick. Four different pore diameters were employed 18 nm, 35 nm, 55 nm, and 73 nm. The template with the smallest pores contained approximately 5 x 10^{10} pores/cm^2. The others had 1 x 10^{10}, 5 x 10^9, and 4 x 10^9 pores/cm^2, respectively. We independently verified the manufacture's pore size and density by scanning electron microscopy.

Ethanol was obtained from AAPER Alcohol and Chemical Co. (Shelbyville, KY), while $AgNO_3$ was purchased from Sigma Aldrich (Milwaukee, WI).

Polished Pyrex 7740 wafers (25.4 mm^2, 0.5 mm thick) were supplied by Precision Glass and Optics (Santa Ana, CA).

Purified water (≥18.2 MΩ·cm) was prepared with a NANOpure Ultrapure Water System (Barnstead, Dubuque, IA).

As stated above, the precursor solution consisted of 1 g of titanium (IV) isopropoxide (Sigma Aldrich, Milwaukee, WI), 0.15 g of HCl (EM Industries, Gibbstown, NJ), and 8.0 g of isopropanol (Acros, Geel, Belgium). The solution was prepared by first adding titanium (IV) isopropoxide followed by the acid. All solutions were used within two weeks. A TiO_2 film was made by depositing approximately 150

μL of the TiO_2 precursor solution onto the Pyrex sample as described above. The reduction of silver from a 0.1 M aqueous silver nitrate solution was performed with a standard 100 W Hg Arc lamp as the UV source. The light was illuminated onto the TiO_2 interface through the Pyrex side of the sample (Figure 2.1). The Pyrex sample is transparent in the near UV (~365 nm), which is the critical wavelength region from reducing silver ions from solution.

AFM measurements of nascently formed Ag nanoparticle arrays were made by using a Nanoscope IIIa (Digital Instruments, Santa Barbara, CA). All measurements were made by tapping mode in air with a type E scanner employing etched silicon tips, NSC15/No Al (Mikro Masch, Wilsonville, OR). TiO_2 film thickness was measured with a Dektak 3 Stylus profilometer (Veeco Tucson Inc., Tucson, AZ). XPS was performed on a Kratos Axis Ultra Imaging X-ray photoelectron spectrometer (Kratos Analytical Inc., Chestnut Ridge, NY).

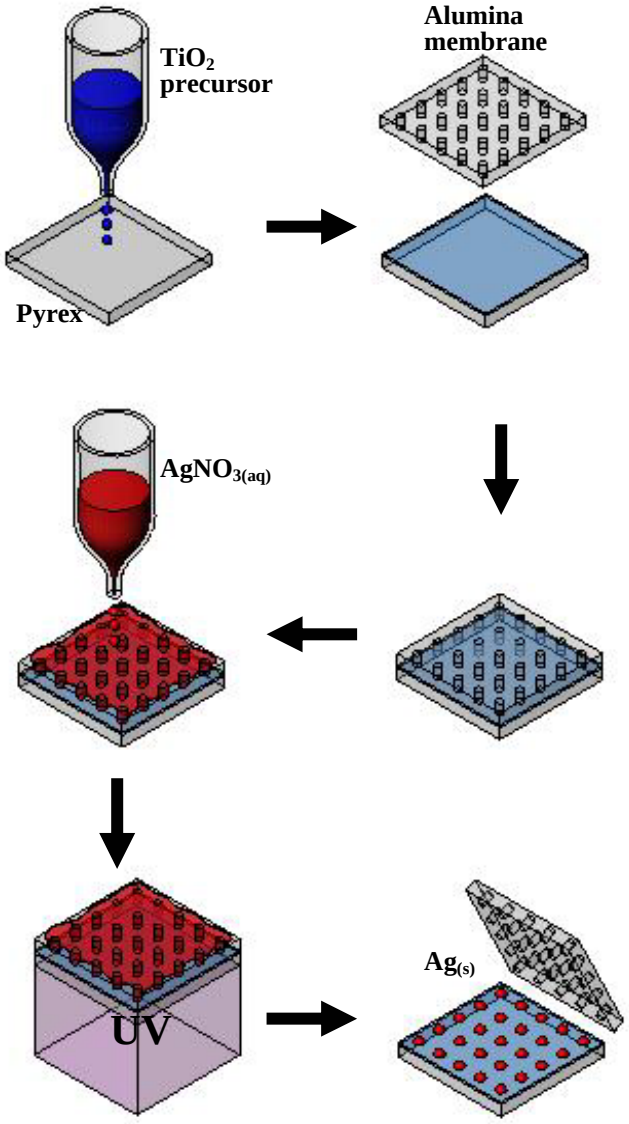

Figure 2.1. Schematic diagram of the process for fabricating silver nanoparticle arrays.

Results and Discussion

Our strategy for forming uniform size arrays of metal nanoparticles is outlined in Figure 2.1. In a first step, a TiO_2 precursor was deposited onto the surface of a Pyrex slide in a dropwise fashion from an alcohol solution. The precursor solution consisted of 1 g of titanium (IV) isopropoxide, 0.15 g of HCl and 8.0 g of isopropanol. Approximately 150 μL of this mixture quickly and completely wetted the surface of a 2.5 cm x 2.5 cm planar Pyrex substrate. Next, a circular nanoporous alumina filtration membrane with 18 nm diameter pores was placed on top of the wet glass slide and the system was allowed to dry under ambient conditions for 6 minutes. As the isopropanol evaporated, the TiO_2 film formed spontaneously on the Pyrex and its presence was directly verified by x-ray photoelectron spectroscopy (XPS). Profilometry measurements showed that the film was approximately 200 nm thick. Atomic force microscopy (AFM) measurements revealed that the coating was very flat with a root mean squared roughness of 0.72 nm over a 1 μm^2 area (Figure 2.2a). This surface roughness was identical to a control experiment where the precursor solution was allowed to evaporate from the substrate in the absence of the alumina membrane. Indeed, no evidence of pillar formation caused by the nanoporous template could be detected. Moreover, only trace amounts of TiO_2 could be found on the alumina surface by XPS. It should be noted that the alumina template was gently pealed off the substrate by a pair of tweezers before AFM and XPS data were obtained.

When forming a silver nanoparticle array, the alumina membrane was left in place on the Pyrex substrate and a 0.1 M $AgNO_3$ aqueous solution was introduced

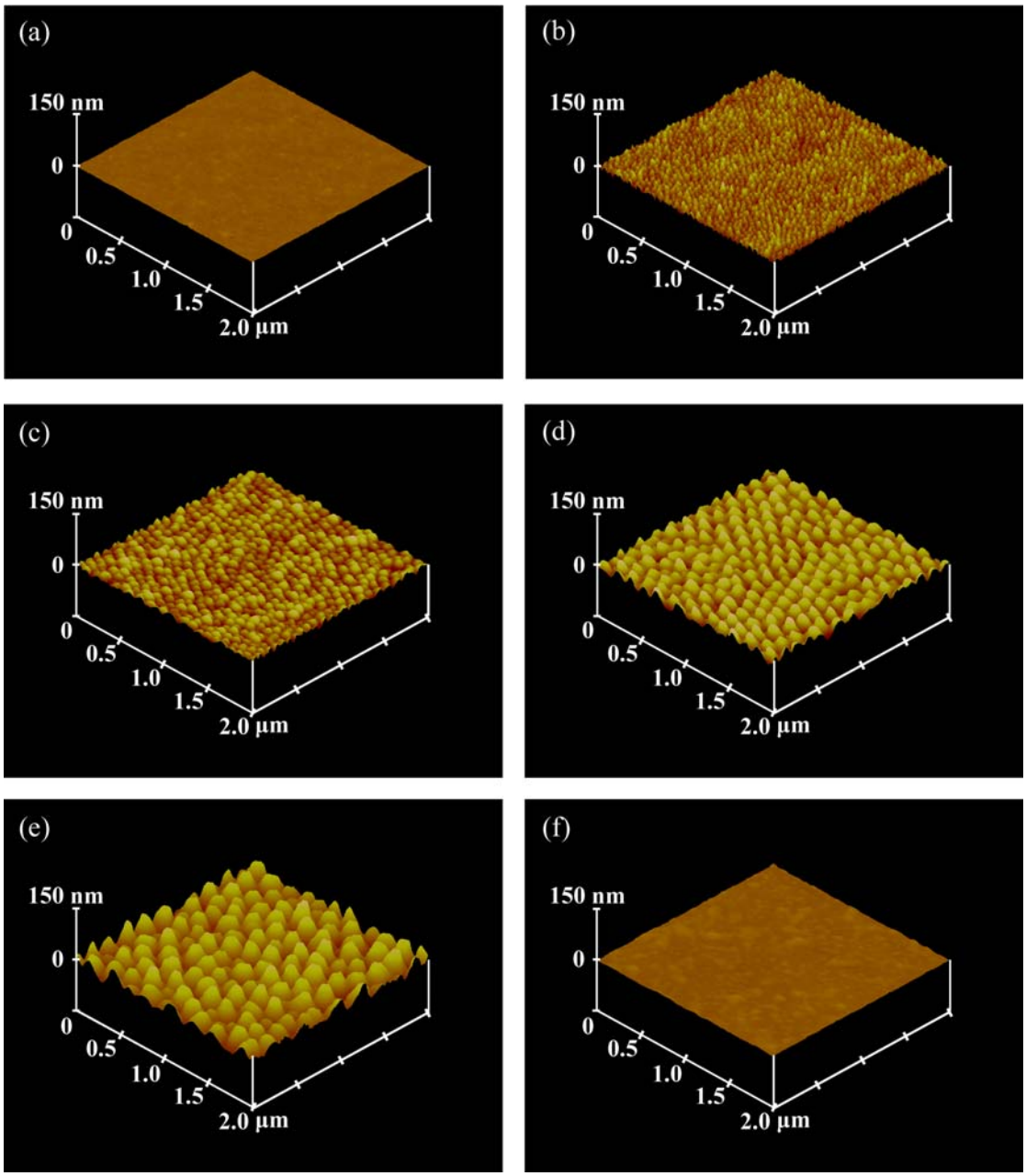

Figure 2.2. AFM micrographs of Ag nanoparticle arrays made by using different pore size templates: (a) bare TiO_2/Pyrex surface, (b) 18 nm template, (c) 35 nm template, (d) 55 nm template, (e) 73 nm template, and (f) a control experiment without UV illumination of the sample.

dropwise above it (~150 μL) after waiting 6 minutes for the precursor solution to dry. This essentially immersed the hydrophilic alumina membrane in bulk aqueous solution. UV radiation was then illuminated onto the alumina/glass interface through the Pyrex substrate to reduce metal from solution for 5 minutes. Finally, the alumina template was gently pealed away from the glass surface and washed with ethanol and deionized water. XPS measurements confirmed the deposition of Ag onto the Pyrex support.

Atomic force microscopy was performed over a 2 μm x 2 μm area in order to access the size, shape, and density of the Ag nanoparticles. The results indicated that the metal nanoparticles were ~19 nm in diameter (Figure 2.2b). This compares favorably with the known template size of the alumina filtration membrane specified by the manufacturer (18 ± 3 nm). Next, several control experiments were performed. For example, the above conditions were repeated exactly, but the surface was left in the dark for 5 minutes instead of being illuminated with UV. This demonstrated that no nanoparticles were formed on the substrate (Figure 2.2f). Also, a control experiment was performed with UV illumination, but without $AgNO_3$ in the aqueous solution. Again, no evidence for nanoparticle formation was found. A final control without a TiO_2 thin film, but with a $AgNO_3$ solution and UV illumination also showed no evidence for metal deposition (AFM data looked identical to Figure 2.2f).

The photoreduction of Ag nanoparticles was repeated with alumina filtration membranes that contained 35 nm, 55 nm, and 75 nm diameter nanopores. The corresponding AFM images are provided in Figure 2.2c-e. Again, the sizes of the

nanoparticles were determined by AFM. The results closely corresponded to the known pore diameters in the alumina template (Table 2.1).

Table2.1. Template pore sizes and resultant mean nanoparticles diameters.

Template pore size (nm)	Mean nanoparticle diameter (nm)
18 ± 3	**19**
35 ± 3	**34**
55 ± 6	**55**
73 ± 7	**72**

To determine information about the particle size distribution, the AFM data were employed to assemble histograms from the arrays of nominally 18 nm, 35 nm, 55 nm, and 73 nm Ag nanoparticles. The number of particles analyzed was 590, 309, 216, and 117, respectively. The bin sizes were 2 nanometers and the results, normalized to 100 total counts, are shown in Figure 2.3. As can be seen from the data, the particle distributions were quite narrow. In each case the vast majority of particles fit into just two bins. Indeed, between 73% and 83% of the nanoparticles were within this range for the three smallest pore sizes and 61% of particles fit within it for the largest filter. In all cases the distributions were slightly skewed toward the low end. This should be expected because the templates provide an upper bound to particle size, while it should be possible to grow nanoparticles on the TiO_2 surface that do not completely fill the pore.

This effect is most pronounced for the largest pore-size where the average particle size would be only modestly larger than 73 nm even in the absence of a template under otherwise similar conditions. It should be emphasized, however, that these results represent some of the narrowest particle distributions achieved to date using any technique.

It was found that the particle arrays were highly uniform over large regions of the Pyrex sample. Data were gathered from multiple 25 μm^2 scan regions on different samples and over areas that were several millimeters apart on single samples. Representative area images are shown as inserts in each histogram in Figure 2.3. Of equal significance, we found that the membrane templates could be used repeatedly. To do this, each alumina template was washed with water and ethanol after being pealed away from the surface. The template was then used with a new precursor solution and Pyrex substrate. The results revealed no perceptible loss in fidelity of the array even after several uses. The alumina membranes were checked for the presence of Ag by XPS and the peak corresponding to Ag was extremely weak (barely above the noise level), when it could be found at all.

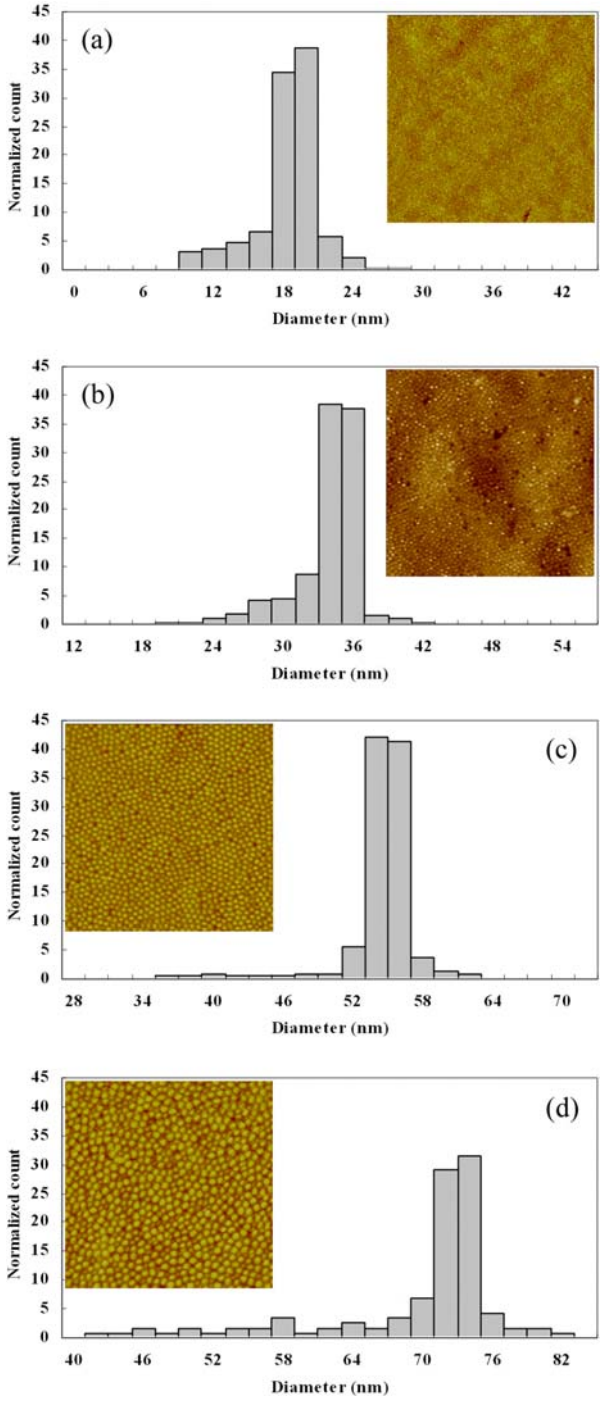

Figure 2.3. Histograms of Ag nanoparticle diameters formed with (a) 18 nm, (b) 35 nm, (c) 55 nm, and (d) 73 nm alumina templates. The insets show representative 5 μm x 5 μm AFM micrographs.

Conclusion

In summary, we have demonstrated a reliable and simple method for the rapid prototyping of metal nanoparticles onto thin TiO_2 films on Pyrex substrates by using UV illumination. All experiments could be performed at a laboratory benchtop with commercially available and relatively inexpensive materials. Moreover, the entire process could be performed from start to finish in about 11 min. The uniform size and shape control of the nanoparticles over large areas suggest that this approach could be employed for biosensor development as well as in catalytic applications. Finally, it should be straight forward to apply this method for producing arrays of other metal nanoparticles such as Au, Pd, and Cu.

CHAPTER III

BENCHTOP CHEMISTRY FOR THE RAPID PROTOTYPING OF LABEL-FREE BIOSENSORS: TRANSMISSION LOCALIZED SURFACE PLASMON RESONANCE DEVICES

Introduction

Surface plasmon resonance (SPR) has recently become a popular method for designing chemical and biological sensors because it affords label-free detection with relatively highly sensitivity.[73, 96, 104-106] Classical SPR applications exploit refractive index changes at the sensor/fluid interface to detect analyte molecules.[107-111] The required reflectometry setup, however, somewhat limits the widespread employment of this type of platform. Recently, a simpler setup, transmission localized surface plasmon resonance (T-LSPR), has been demonstrated.[82, 112-114] T-LSPR can be achieved with noble metal nanoparticles spread on a transparent substrate. The surface nanoparticle conduction electrons collectively oscillate when an electromagnetic wave is introduced. This coherent oscillation can induce photon absorption and scattering, both of which are very sensitive to the dielectric properties of the surrounding medium.[82, 95] This effect is typically present only when the metal particle size is smaller than the wavelength of the incident light. Moreover, this optical phenomenon is strongly sensitive to nanoparticle size, shape, and composition.[115-117]

In previous LSPR work, Okamoto and coworkers used colloidal gold nanoparticles spread on glass substrates for sensing polymer coatings.[112] Rubinstein and coworkers demonstrated the use of evaporated gold island films for chemical sensing.[113, 118, 119] Van Duyne and coworkers employed silver nanotriangles fabricated by nanosphere lithography for sensing proteins,[82] while Chilkoti and coworkers have demonstrated a successful colloidal gold nanoparticle SPR biosensor.[114] Other researchers have also used similar transmission approaches for mono/multilayer film sensing,[112, 113, 118-120] protein binding assays,[3, 82, 95, 114, 115] DNA hybridization,[121, 122] as well as polymer studies.[123] Because very simple instrumentation such as a conventional UV-Vis spectrometer can be used in conjunction with the LSPR approach, biosensing has certainly become more convenient. Nevertheless, the fabrication of the sensing platforms is still an elaborate and time consuming which requires specialized equipment and/or environments. Therefore, it would be important to design a simple, inexpensive, and rapid method for T-LSPR biosensor fabrication, which could still maintain high sensitivity for protein detection.

We have recently demonstrated a rapid prototyping approach for the fabrication of monodisperse silver nanoparticle arrays on TiO_2 thin films. TiO_2 is a well-studied photocatalyst, which has been widely used for metal nanoparticle preparation.[97-103, 124] The process involves the photoreduction of metal by UV illumination of the oxide thin film.[97-99, 103, 124, 125] The size, shape, and density of the metal nanoparticles in our method can be controlled by using nanoporous alumina filtration membranes as templates. The alumina template confines the size and shape of the nanoparticles during their

production. The entire fabrication process can be completed at a standard laboratory benchtop within 11 min without the need for vacuum techniques or a clean-room environment. Moreover, highly monodisperse metal particles in a size range between 10 and 100 nm can be easily produced.

We reasoned that our metal nanoparticle arrays should be a convenient platform for creating T-LSPR biosensor substrates (Figure 3.1). To investigate this, a monodisperse silver nanoparticle array was fabricated by the template photoreduction process and then treated with a ligand-linked thiol for protein capture from solution. The well-studied biotin/streptavidin binding pair was chosen for the purposes of demonstration. It was found that the size of the silver nanoparticles employed was critical for obtaining high quality binding data. Specifically, smaller particles (~19 nm), which had narrower plasmon bands were found to be superior to larger particles (>50 nm). To the best of our knowledge, the platform we employ has one of the narrowest particle arrays used to date for protein detection. The results clearly demonstrate high signal-to-noise ratios from a single layer of metal particles. Binding curves could be constructed for determining the equilibrium dissociation constant.

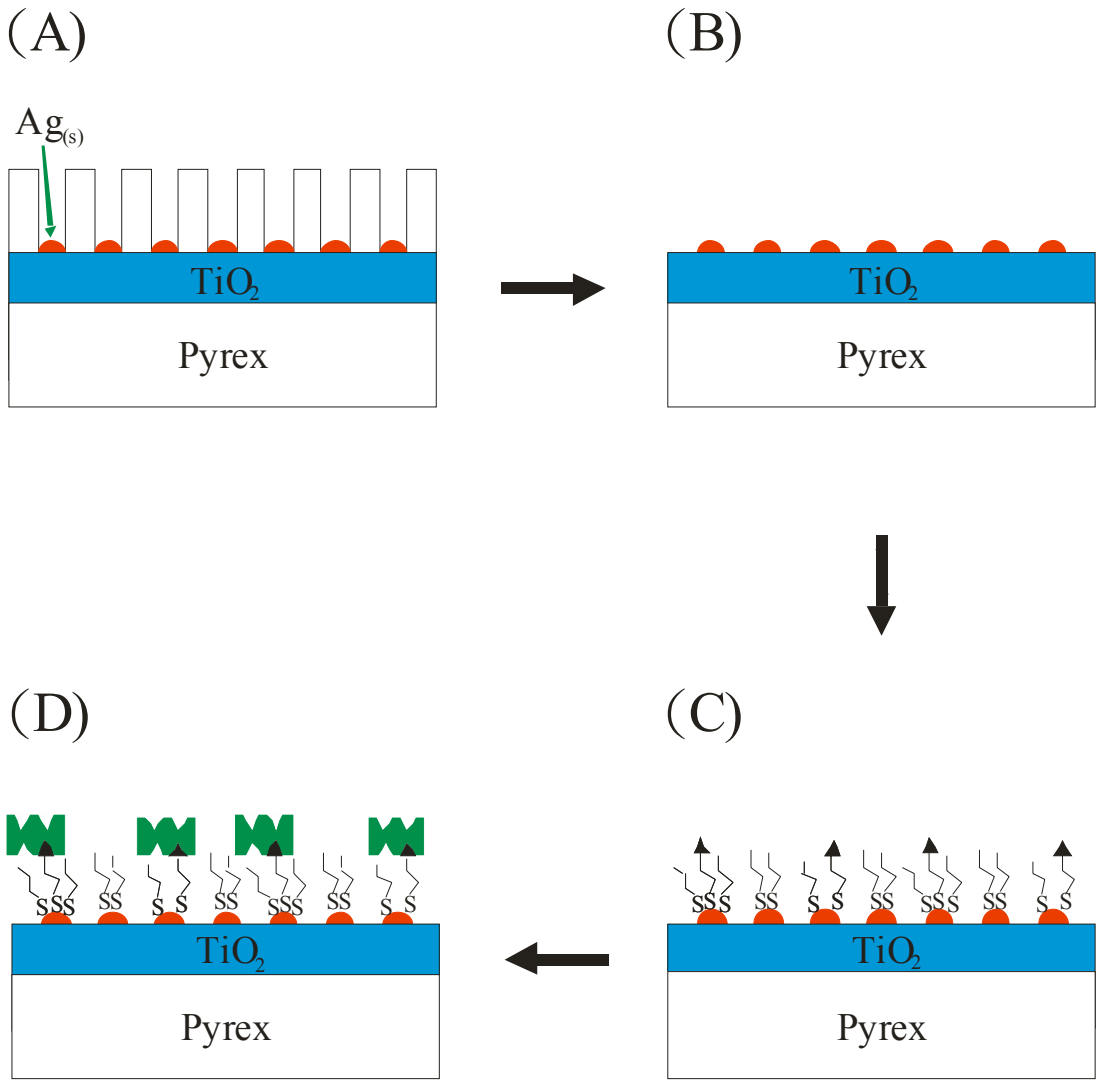

Figure 3.1. Schematic diagram of the process for fabricating monodisperse silver nanoparticle based T-LSPR biosensors. (A) Silver nanoparticle array templated by an alumina membrane on thin TiO_2 film during the photoreduction process. (B) Monodisperse silver nanoparticle array after alumina membrane lift off. (C) Biotin/PEG modified silver nanoparticle biosensing array. (D) Sensing of streptavidin molecules.

Experimental Section

Materials

Polished Pyrex 7740 wafers (25.4 mm^2, 0.5 mm thick) were purchased from Precision Glass and Optics (Santa Ana, CA) and the nanoporous alumina filtration membrane templates came from Synkera Technologies (Longmont, CO). The nanotemplates had pore sizes of 18 nm, 35 nm, 55 nm, and 73 nm (1.3 cm diameter, 50 μm thickness). The templates had pore densities of 5 x 10^{10}, 1 x 10^{10}, 5 x 10^9, and 4 x 10^9 pores/cm^2, respectively, according to the manufacturer. We confirmed these values in house by scanning electron microscopy (Zeiss 1530 VP FE-SEM). Titanium (IV) isopropoxide, $AgNO_3$, 4-(2-hydroxyethyl)piperazine-1-ethane sulfonic acid (HEPES buffer salt), bovine serum albumin (BSA), sodium phosphate, and sodium chloride were purchased from Sigma-Aldrich (Milwaukee, WI). HCl was purchased from EM Industries (Gibbstown, NJ) and isopropanol was purchased from Acros (Geel, Belgium). Ethanol was obtained from AAPER Alcohol and Chemical Co. (Shelbyville, KY). Purified water (≥18.2 MΩ·cm) was prepared with a NANOpure Ultrapure Water System (Barnstead, Dubuque, IA). H_2O_2 and H_2SO_4 were purchased from EMD Chemicals Inc. (Gibbstown, NJ). Biotin PEG disulfide (Figure 3.2, structure 1) and PEG propionate disulfide (Figure 3.2, structure 2) were obtained from BioVectra Inc. (Prince Edward Island, Canada). Streptavidin and Texas Red-labeled streptavidin were purchased from Invitrogen (Eugene, OR).

Structure 1: Biotin PEG Disulfide

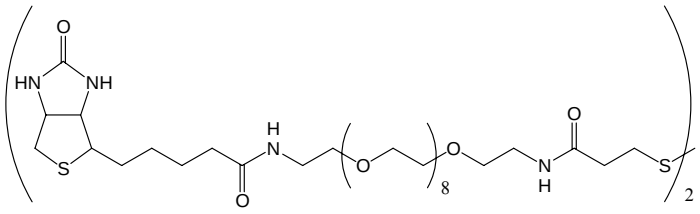

Structure 2: PEG Propionate Disulfide

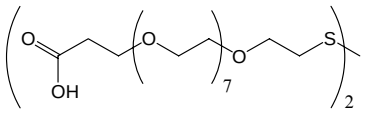

Figure 3.2. Biotin PEG disulfide (structure 1) and PEG propionate disulfide (structure 2) structures.

Solution Preparation

HEPES buffer solution was made with purified water (10 mM, pH 7.4), while 10 mM phosphate buffered saline (PBS) was slightly less basic (pH 7.2). Biotin PEG disulfide and PEG propionate disulfide solutions were prepared as 2 mg/mL and 10 mg/mL stock solutions in HEPES buffer, respectively. These solutions were prepared immediately before use. Streptavidin, Texas Red labeled streptavidin, and bovine serum albumin (BSA) solutions were prepared in PBS buffer, and were prepared as stock solutions at 1 mg/ml before dilution to the appropriate concentration.

Preparation of Biosensor Substrates

A transparent Pyrex wafer was used as the substrate and was soaked in piranha solution (1:3 ratio of 30% H_2O_2 and H_2SO_4) to remove organic contaminants from the

surface. Caution: piranha solution is a vigorous oxidant and should be used with extreme care. Next, the substrate was rinsed with copious amounts of purified water and dried with nitrogen gas. At this point ~150 μL of a TiO_2 precursor solution was deposited onto the surface of the slide with a pipette. This solution was made from 1 g of titanium (IV) isopropoxide, 0.15 g of HCl and 8.0 g of isopropanol. Next, a nanoporous alumina filtration membrane was placed on top of the solution-covered Pyrex slide and the liquid was allowed to evaporate under ambient conditions for 6 min. Following this, 300 μL of 0.1 M $AgNO_3$ solution was introduced to the top side of the alumina membrane and the entire system was exposed to UV irradiation, which was applied through the Pyrex side for 5 min. This was done with a standard 500 W Mercury Arc lamp (Newport Oriel Instruments, Stratford, CT). After photoreduction of the metal particles onto the TiO_2 thin film, the alumina template was gently peeled away and the supported silver nanoparticle array was washed with ethanol and purified water. In the penultimate step, the substrate was incubated overnight in a solution of 0.5 mg/mL biotin PEG disulfide solution, which also contained 5 mg/mL PEG propionate disulfide (10 mM HEPES, pH 7.4).[103] To prevent oxidation of the biotin molecules, the incubation was performed in the dark and the solution was surrounded by a N_2 atmosphere. Finally, the nanosensor array was washed with ethanol and distilled water. At this point it was ready for protein biosensing.

Fluorescence control experiments were performed to ensure that biotin was appropriately presented on the nanoparticle array. A 1.0 μM solution of Texas Red-labeled streptavidin was introduced above the sample, incubated for 30 minutes, and

then washed away with HEPES buffer. A strong fluorescent signal was detected from the sensing array under an upright fluorescence microscope (Eclipse E800, Nikon). The fluorescence response was almost completely absent when the same system was placed under the microscope without the presence of biotin ligands at the interface.

SPR Measurements and Substrate Imaging

AFM measurements of Ag nanoparticle arrays were made with a Nanoscope IIIa from Digital Instruments (Santa Barbara, CA). These experiments were done in tapping mode in air with a type E scanner employing etched silicon tips (NSC15/No Al, Mikro Masch, Wilsonville, OR). UV-Vis spectra were taken with a Lambda 35 UV/Vis spectrometer (PerkinElmer Instruments, Shelton, CT). Since the Pyrex substrates were transparent, the chips could be directly and conveniently seated inside the spectrometer.

Results

T-LSPR Spectrum of Monodisperse Silver Nanoparticle Arrays

In a first set of experiments, a silver nanoparticle array was prepared with an alumina membrane template containing 18 nm pores. As can be seen from the AFM image, the nanoparticles were nearly uniform with an average full width at half height (FWHH) of ~19 nm (Figure 3.3). The nearly monodisperse supported particle array was then tested for T-LSPR. The absorption peak at 480 nm in the UV-Vis spectrum (Figure 3.4b) is consistent with the plasmon resonance of the Ag nanoparticles reported earlier in literature.[126-128] It suggests that SPR properties of the Ag nanoparticles is not

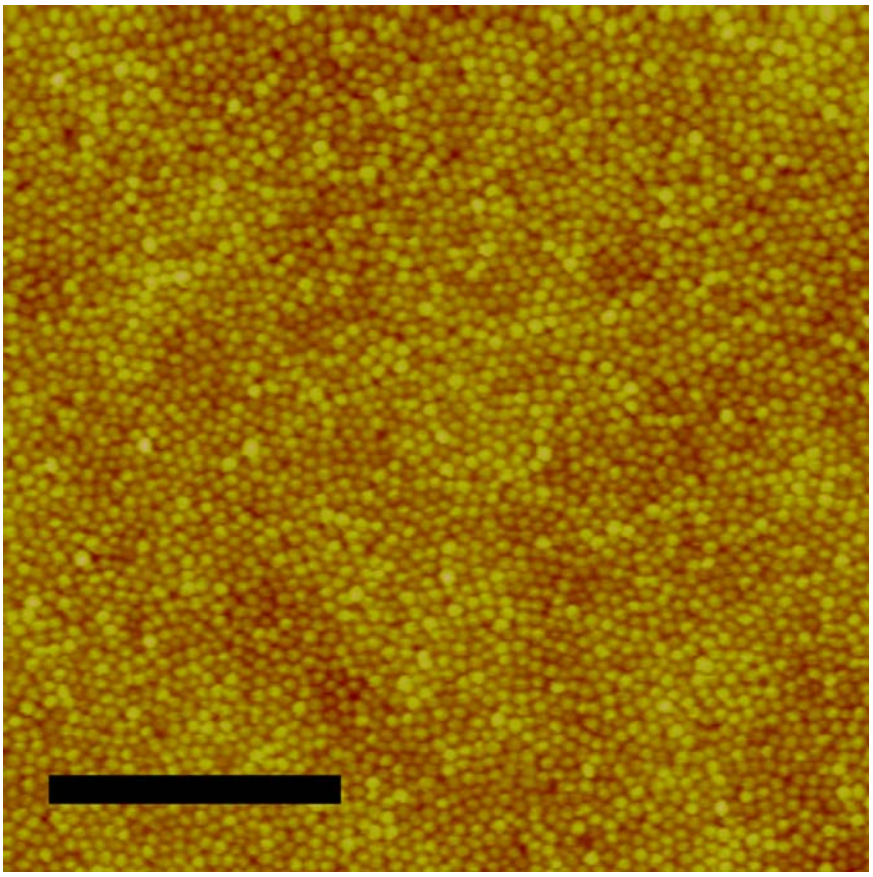

Figure 3.3. AFM micrograph of a Ag nanoparticle array using 18 nm pore size template. The dome-shaped nanoparticles are very uniform in size and with a full width at half height of 19 nm. Scale bar: 1 μm.

significantly changed by the TiO_2 substrate. It should also be noted that bare TiO_2 surfaces had no such absorption features in this frequency range (Figure 3.4a).

Arrays with silver nanoparticles of different sizes were fabricated by using nanoporous alumina templates with different pore sizes (35 nm, 55 nm, and 73 nm). The silver nanoparticles made from them had an average particle size (FWHH) of 34 nm, 55 nm, and 72 nm, respectively, as determined by AFM. The plasmon resonance absorption peak was found to red-shift with increasing size of the silver nanoparticles (Figure 3.4). Moreover, the peak intensity increased and the peak width broadened with increasing particle size. Such observations are consistent with theory.[129-131] The red shift of the absorption with increasing nanoparticle size is expected with a quantum confinement effect. Both the dipole and quadrupole resonance modes should contribute to this. The resonance of the quadrupole moment appears at longer wavelength than that of dipole moment. Increasing contribution from quadrupole resonance modes with increasing size of the nanoparticles, will make the peak appear much broader and apparently red-shift. Similar observations have been made previously with similar systems.[18, 23, 132-134] Here we demonstrated that such spectral properties can be achieved with nanoparticles made by rapid prototyping methods. In fact, the optical properties appear to be comparable with, if not better than, those obtained with metal particles which were fabricated by more complex and time-consuming strategies.

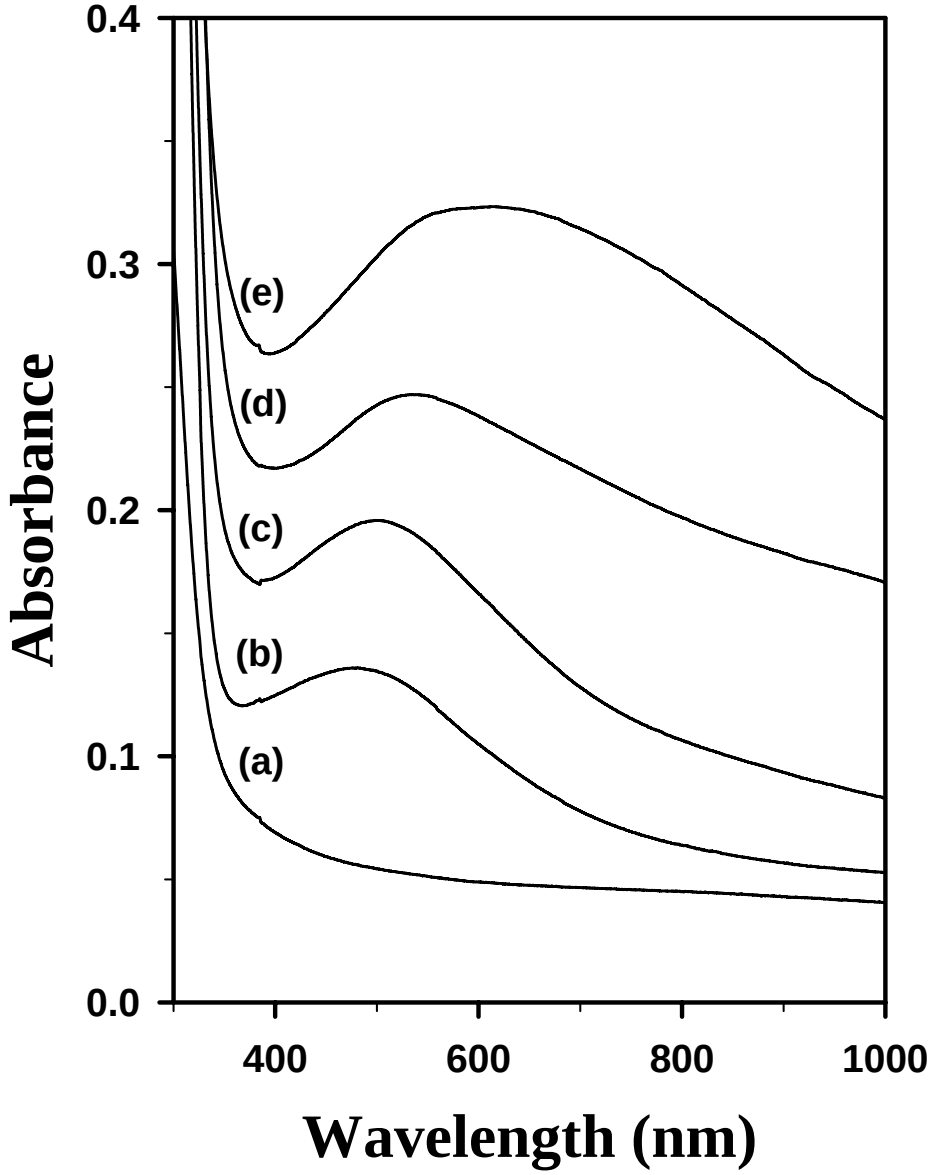

Figure 3.4. UV/Vis spectrum of (a) TiO_2 background, and four different diameter silver nanoparticle arrays fabricated by (b) 18 nm, (c) 35 nm, (d) 55 nm, and (e) 73 nm templates, respectively.

T-LSPR Biosensors

The monodisperse silver nanoparticle array was incubated overnight in a solution containing 0.5 mg/mL biotin PEG disulfide and 5 mg/mL PEG propionate disulfide in 10 mM HEPES buffer (pH 7.4) to obtain a biotin terminated surface as shown schematically in Figure 1c. The biotin terminated nanoparticle array was then incubated with streptavidin solutions of varying concentrations for 30 min. Absorption spectra were taken before and after each incubation. Fig. 3.5 shows a typical experiment performed with a 19 nm silver nanoparticle array. It was found that the plasmon band red-shifted upon protein adsorption until the surface was saturated with protein. We also noted in most experiments that the plasmon peak intensity increased upon adsorption; however, the peak intensity was not as reliable an indicator of protein binding as the frequency shift, in agreement with previous works.[3]

Fig. 3.6 shows the binding curve for the biotin-streptavidin binding system using the 19 nm diameter silver nanoparticles. Again, the metal nanoparticles were terminated with biotin moieties diluted into PEG in a ratio of 10:1. The curve was obtained by introducing streptavidin solutions above the sample in a concentration range from 10^{-16} M to 10^{-6} M. In order to achieve equilibrium, all the protein incubation experiments were performed in a dark, hermetically sealed environment for a minimum of 3 hr.[3] At the lowest protein concentration (10^{-16} M), it was incubated for 24 hours to insure equilibrium had been achieved.

As can be seen from the data, the plasmon resonance shifted with increasing protein concentration, and a simple Langmuir isotherm could be used to fit the data:[3]

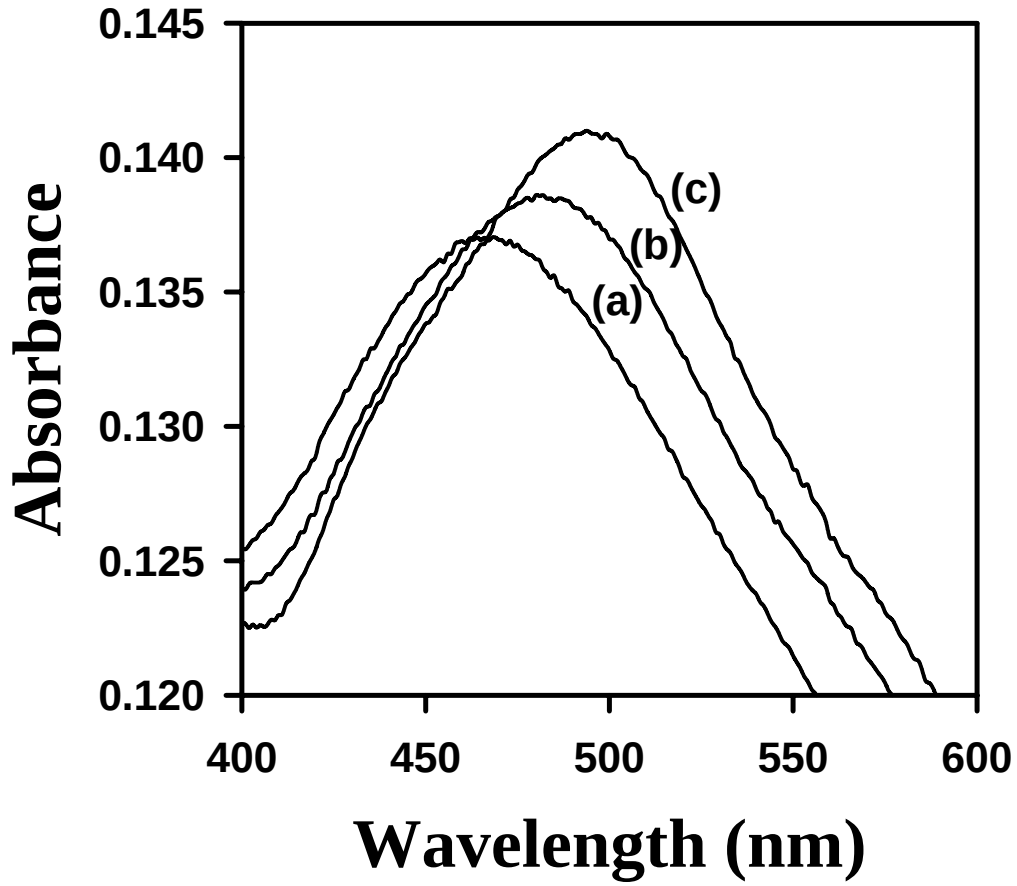

Figure 3.5. UV/Vis spectra of 19 nm diameter Ag nanoparticle biosensor array (a) before, and after incubated with (b) 10^{-12} M, and (c) 10^{-6} M streptavidin solutions, respectively.

$$\Delta\lambda / \Delta\lambda_{max} = K [SA] / (1 + K [SA])$$

where $\Delta\lambda$ is the wavelength shift caused by the addition of protein and $\Delta\lambda_{max}$ is the wavelength shift which was observed at saturation. K is the equilibrium binding constant and [SA] is the concentration of streptavidin applied to the system. Using this equation gave a value of $K = 2 \times 10^{12}$ M^{-1}, which is consistent literature values for similar surface systems measured with other methods.[135]

Several control experiments were run to ensure that the data in Figure 3.6 were not the result of non-specific adsorption. First, 1 mg/mL bovine serum albumin (BSA) in PBS buffer (10 mM PBS, pH 7.2) was added to the biotin-PEG-conjugated 19 nm silver nanoparticle array. No discernable SPR peak shift was observed under these conditions. In a second control experiment, a 5 mg/mL PEG propionate disulfide solution was incubated over a Ag nanoparticle array in the absence of biotinylated ligands. This system was challenged with a 10^{-6} M streptavidin solution for 30 minutes. Again, no evidence for an SPR shift could be found within experimental error. As expected, nonspecific binding of protein molecules to the PEG-covered nanoparticles was quite low.[103]

By applying the same preparation methods, different diameter silver nanoparticle biosensors were also examined. Interestingly, the sensitivity of the sliver nanoparticle sensors was particle size dependent. Fig. 3.7 shows the absorption spectra of three different diameter silver nanoparticle biosensors prepared by the same procedures as the 19 nm silver nanoparticle array. Absorbance data are displayed both before and after a

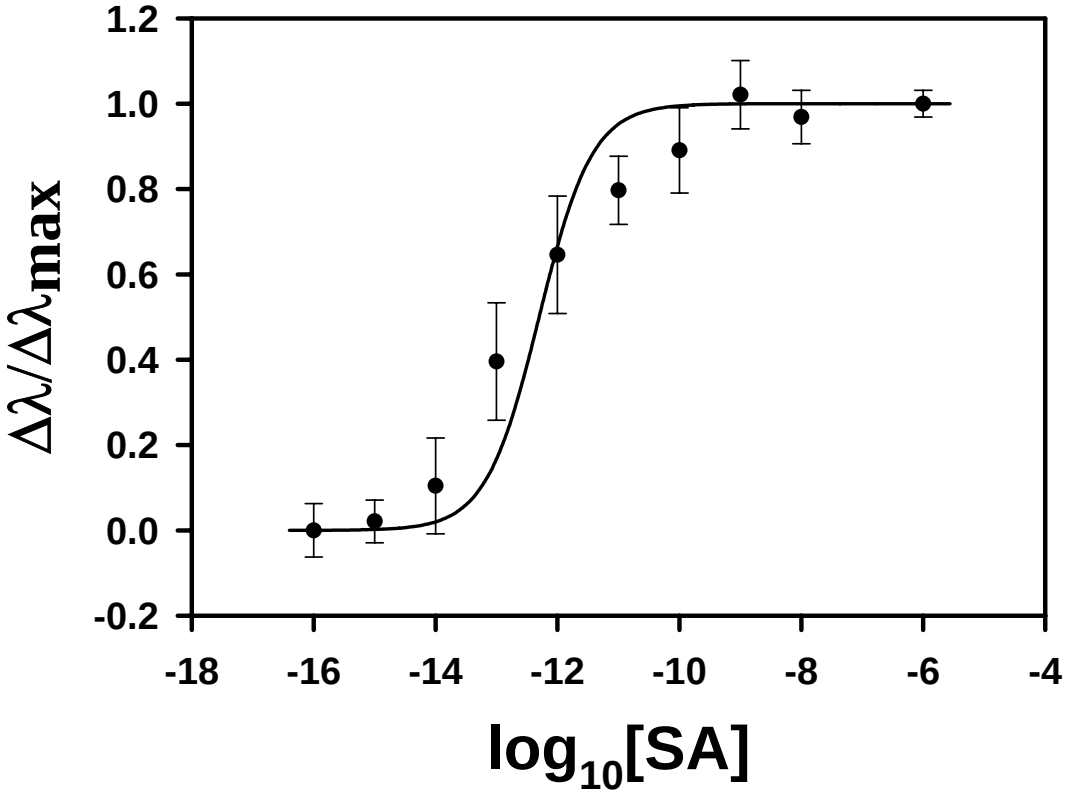

Figure 3.6. Binding curve of biotin-streptavidin interaction using 19 nm diameter Ag nanoparticle biosensor array. Solid dots represented experimental points while the curve was a Langmuir fitting.

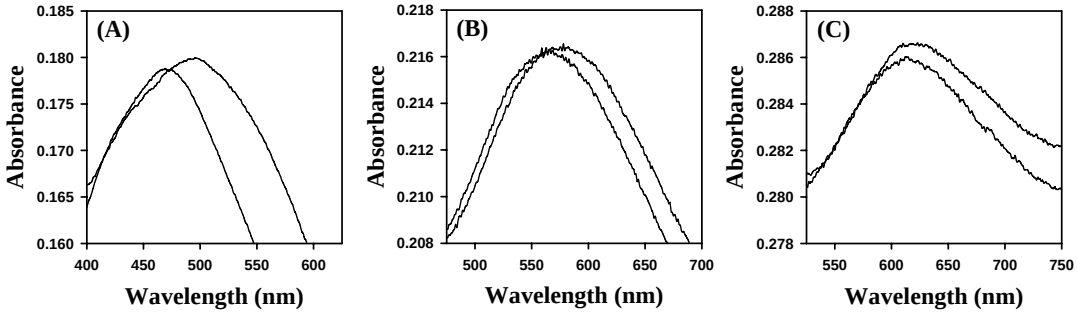

Figure 3.7. UV/Vis spectrum of different diameter Ag nanoparticle biosensor arrays before, and after incubated with 10^{-6} M streptavidin solutions, respectively. (A) 34 nm, (B) 55 nm, (C) 72 nm Ag nanoparticle.

30 min. incubation of the sensor platform with a 1.0 μM streptavidin solution. This concentration should be more than enough to cause saturation binding under the conditions employed. As can be seen, protein binding caused a red shift in the plasmon resonance for all three diameters of Ag nanoparticles employed. However, the degree of red shift, $\Delta\lambda_{max}$ is size dependent. A very distinct decrease in $\Delta\lambda_{max}$ was observed with increasing metal particle size. The values of $\Delta\lambda_{max}$ for each metal particle size are provided in Table 1. As can be seen, the sensitivity is virtually same for the 19 nm array and the 31 nm array. The sensitivity drops quickly as the size increased further, suggesting that the larger particles became increasingly less useful as SPR sensors. This was the case in spite of the fact that the absorbance maximum of the plasmon resonance increased with size (Table 3.1). Therefore, for practical sensor design, it appears that smaller nanoparticle sizes (at least down to 30 nm) appear to be more useful than larger ones. Our current results may seem somewhat different than those reported by Nath and Chilkoti, where they found that the nanoparticles with 39 nm diameters had optimal sensitivity. One possibility for the apparent discrepancy may result from the different shapes of nanoparticles used in the two studies. Nath and Chilkoti made spherical gold nanoparticles in solution and load them on the substrate, while our nanoparticles are dome-shaped. Note that the full widths of these dome-shape particles were significantly larger than the FWHH values we reported here.

Table 3.1. Maximum wavelength shifts ($\Delta\lambda_{max}$) with different size Ag nanoparticles.

Particle size FWHH (nm)	**Maximum wavelength shift $\Delta\lambda_{max}$ (nm)**	**Absorbance at λ_{max}**
19	**24 ± 4**	**0.137**
34	**21 ± 3**	**0.179**
55	**12 ± 4**	**0.216**
72	**10 ± 2**	**0.285**

Discussion

Ideal biosensors should be extremely sensitive, highly selective, simple to fabricate, and easy to use. Moreover, they should operate with tiny sample volumes in a label free fashion with low background response. Surface plasmon resonance techniques have, at least in principle, many of these features, which would allow them to compare favorably with conventional labeling techniques such as fluorescence.[136] In particular, T-LSPR should be easier to employ than reflectometry SPR because of its very simple setup. The combination of transmission mode detection, rapid metal nanoparticle fabrication, and surface passivation with a PEG-thiol appear to make this platform attractive. However, it is important to compare the advantages and drawbacks of the present design with previous biosensor platforms.

For T-LSPR sensors, Au/Ag nanostructures are common choices. Among the several T-LSPR experiments based on Au/Ag nanoparticles reported previously, two general strategies were employed to fabricate nanoparticles arrays on substrates. First, nanoparticles can be made in solution with standard procedures and load to the substrate with specific linkage or non-specific adsorption. This strategy requires certain adhesion chemistry, which may complicate the sample preparation and affect the SPR properties of the nanoparticles. Alternatively, the nanoparticles can be directly fabricated in situ on substrates. However, direct deposition usually offers less than ideal control of geometry and uniformity of the nanoparticles. Our current method combines the advantages of several methods, by fabricating the particles in situ with template. The size distribution of the resulting particles (Figure 3.3) is extremely narrow. In fact, it is one of most

uniform nanoparticles assembles reported in the literature. It should be pointed out that nanosphere lithography employs the same concept of the template deposition, and therefore the nanotriangle arrays made share the similar high uniformity. However, the surface coverage of the nanoparticles in typical nanosphere lithography ~10% is much lower than that of the current method, > 60%, and high-vacuum CVD device is needed. Our current procedure requires no special device and takes no more than 11 min.

The detection limit is estimated to be $\sim 5\times10^{-14}$ M for stretropvion binding to the biotinated surface. (Figure 3.6) It is better than several systems previously reported where the same binding pair was tested.[137-139] The detection limit, however, is directly related to the binding affinity that may vary in different systems. To better evaluate our system, we estimate that protein coverage of 10% or less of saturation conditions can be detected with the 19 nm Ag nanoparticle array in the present setup. Under those conditions there are roughly 10^9 metal nanoparticles in a 1 mm^2 area and ~10 available biotin sites/particle. Because the biotin binding sites are fairly dilute under the present conditions, most binding events between biotin and streptavidin should be monovalent. For a 1 mm^2 beam diameter in the UV-Vis, this technique would monitor $\sim10^9$ streptavidin molecules.

Conclusion

A fast and convenient preparation method was developed to fabricate uniform metal nanoparticle arrays, which are superior platforms for label-free biosensing based on transmission localized surface plasmon resonance (T-LSPR). The nanoparticle arrays were fabricated through a combination of templating and photoreduction in a matter of a few minutes without any complicated instrumentation or sophisticated preparation procedures. A 24 nm wavelength shift in the LSPR was observed upon protein binding with surface modified thiol-linked ligand moieties. A detection limit in the low pM range could be achieved without any loss of sensitivity with this convenient and cheap rapid-prototyping method. Moreover, the LSPR sensitivity was found to be particle size dependent.

CHAPTER IV

TEMPLATING WATER STAINS FOR NANOLITHOGRAPHY*

Introduction

Well-defined nanoscale features have received substantial interests from scientists and engineers because of their potential applications in photonics,[7, 8] electronics,[6] material science,[14] and biotechnology.[1, 3, 5, 9, 10, 12] A variety of methods now exist to create nanoscale structures.[29, 31, 44, 57, 140-143] For example, photolithography provides a top-down method for creating large areas of well-defined features.[29] The capabilities of conventional photolithography are, however, typically restricted to the diffraction limit of light (>100 nm). On the other hand, electron-beam lithography is able to create features of nearly arbitrary two-dimensional geometry on a scale below 100 nm.[31] Despite its high resolution, e-beam lithography is time consuming when large arrays are required. Moreover, the process must take place at a dedicated facility in a vacuum environment with relatively expensive equipment. These restriction have motivated the search for alternative pathways to fabricating large areas of ordered patterns.[47, 49, 144]

Irreversible solvent evaporation has recently been employed to create patterns via the dynamic self-assembly of nonvolatile dispersed solute particles.[145-147] This technique has been used to make intricate patterns, but with random size, spacing, and periodicity.

---

*Reproduced with permission from "Templating Water Stains for Nanolithography" by Liao, W. S.; Chen, X.; Chen, J.; Cremer, P. S. *Nano Letters,* **2007**, *7,* 2452-2458. Copyright 2007 American Chemical Society.

Precise control over feature morphology has been very difficult to achieve because of instabilities in the evaporation process.[148] On the other hand, concentric micron-size patterns can be formed through the solvent evaporation process using a sphere-on-flat geometry combined with repetitive stick-slip motion under the control of a motor.[149-151] These non-conventional patterning techniques provide an alternative route for fabricating large area features. Nevertheless, the use of the solvent evaporation process under well controlled conditions for nanoscale patterning is still a major challenge.

Template-based techniques have provided a very easy and inexpensive way to fabricate nanoscale structures.[45-56, 125] These techniques use nanospheres,[46-49, 52-54] nanoporous anodic aluminum oxide (AAO),[45, 50, 56, 125] nanochannels,[51, 57] or nanoholes[55] as templates. They can typically be combined with chemical vapor deposition,[46-48] ion-beam bombardment,[45, 51, 54, 56] edge spreading,[49] electrochemical deposition,[50, 55] selective wetting,[52, 53] and photoreduction[125] methods to fabricate nanoscale structures. Under precise template confinement, these techniques can easily fabricate large areas with minute features. We therefore reasoned that it might be possible to combine solvent evaporation with a templating approach to design a simple, yet powerful new nanoscale patterning technique.

Herein we demonstrate the use of water stain lithography (WSL) to create large areas of twin features. Arrays of nanoscale double rings could be produced by localized solute accumulation during the solvent evaporation process, using self-assembled polystyrene spheres as templates. The double-ring structures could be formed in about 90 min with very simple equipment. Line widths under 30 nm were achieved with this

method. The specific geometry of double-ring features could be precisely controlled by varying solution conditions during fabrication (Figure 4.1). This included the center-to-center distance between double rings (D), the radii of the rings (r_1 and r_2), the gap size between concentric rings (d), and the width of the individual rings (w_1 and w_2). It was even possible to eliminate the presence of the outer ring.

Experimental Section

Our procedure for making hexagonally arrayed patterns of nanoscale double-rings is outlined in Figure 4.2. First, a thin layer of photoresist was spin-coated on top of a supporting substrate. Next, a polystyrene sphere suspension solution was introduced in a dropwise fashion on top of the polymer. The solution was an aqueous/organic mixture, which served to soften the photoresist surface.[152] The whole chip was then allowed to dry under ambient conditions. After the solution evaporated from the surface, the polystyrene spheres were removed by sonication in pure water and the hexagonally arranged double-ring features remained impressed in the underlying film. The entire process could be completed within 90 minutes without any additional instruments.

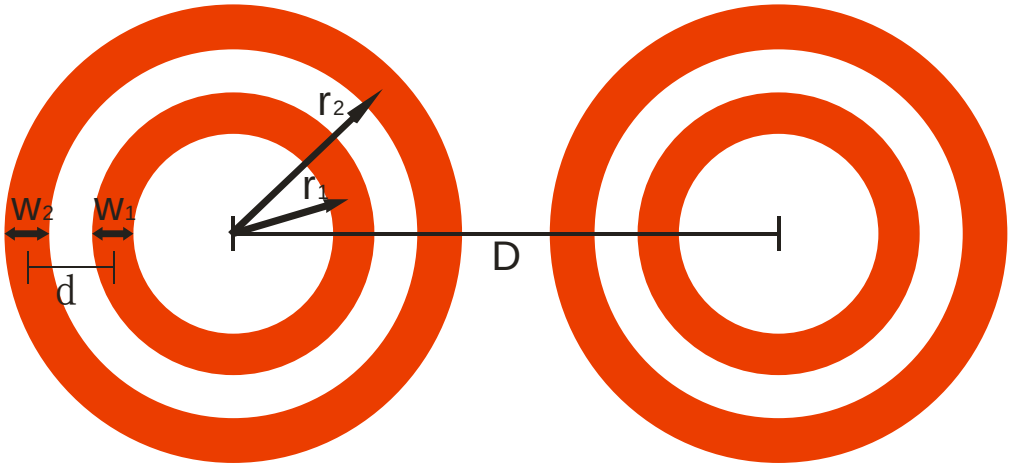

Figure 4.1. Parameters for double-ring features.

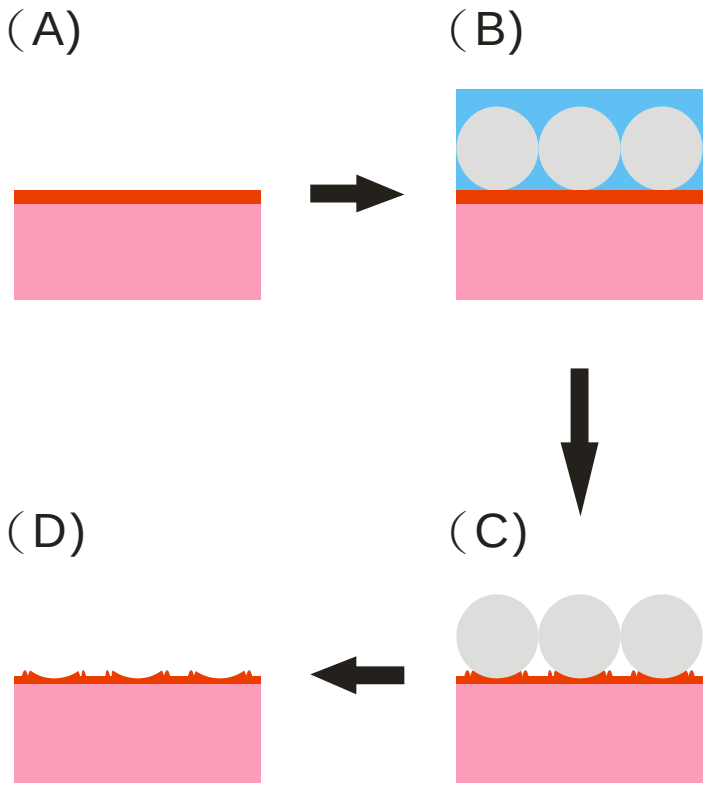

Figure 4.2. Schematic diagram of the process for fabricating double-ring features. (A) Spin-coating a thin layer of polymer onto a substrate. (B) Polystyrene spheres are spread on top of the chip. (C) The chip is allowed to dry under ambient conditions. (D) The spheres are removed by sonication under water.

Results and Discussion

Forming Double Rings

To perform double-ring array patterning, a stock polymer solution of Shipley 1805 (Microchem, MA) was diluted by Thinner P solution (Microchem, MA) to a 1:5 volumetric ratio in a first step. Five drops of the solution were spread on top of a 1 in. × 1 in. Au coated glass slide and spin-coated at 2000 rpm for 2 min. Following this, the polymer coated chip was baked at 90 ˚C for 1 min., ramped to 120 ˚C for another 1 min, and then allowed to cool to ambient temperature. This created a polymer layer with a thickness of ~100 nm on top of the substrate. The thickness was verified by measuring the depth of a scratch on the polymer surface with an atomic force microscopy (AFM). After the chip cooled to room temperature, a 10.0 μL solution containing suspended monodisperse polystyrene spheres (Duke Scientific, CA) was mixed with a 10.0 μL aqueous solution containing 20% acetone by volume. This final mixture (10% acetone by volume) was introduced dropwise onto the surface. Four particle sizes were employed: 600 nm, 800 nm, 1 μm, and 2 μm.

The solvent was allowed to completely evaporate under ambient conditions over the course of 1 hr. This should leave a monolayer of hexagonally close packed polystyrene spheres behind on the surface[153, 154] and such packing was confirmed by AFM. At this point the polystyrene spheres were removed by bath sonication in deionized water for 5 min. The samples were dried and then imaged by AFM (Figure 4.3). As can be seen in these 5 μm × 5 μm images, well defined double-ring features were obtained with high resolution. The features formed hexagonal arrays with a characteristic lattice spacing of

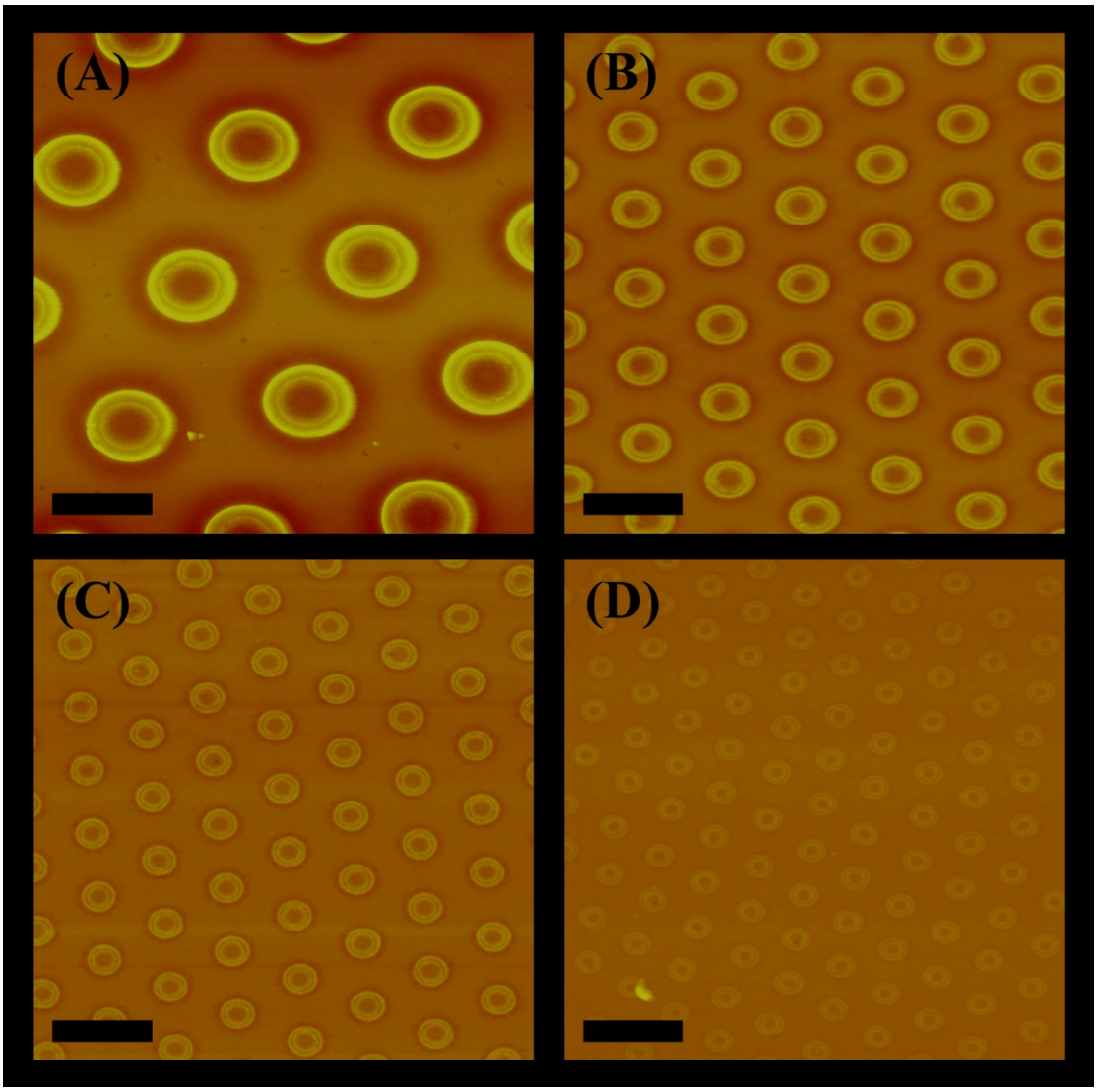

Figure 4.3. 5 μm × 5 μm AFM images of double-ring features fabricated by applying polystyrene spheres of varying diameters: (A) 2 μm (B) 1 μm (C) 800 nm (D) 600 nm. Scale bars: 1 μm.

(A) 2 μm, (B) 1 μm, (C) 800 nm, and (D) 600 nm, which corresponded exactly to the size of the polystyrene spheres from which they were templated. The diameters of the double ring features, however, were significantly smaller. For example, for the 800 nm lattice spacing (Figure 3C), the inner (D_{inner}) and outer (D_{outer}) ring diameters were 217 nm and 309 nm, respectively. The inner and outer rings, therefore, had an aspect ratio of ~0.27 and ~0.39 with respect to the 800 nm template sphere. The gap between the two rings was 48 nm and the thickness of each ring was 33 nm. Interestingly, the aspect ratio between the ring diameters and the template sphere diameter remained unchanged within experimental error for all sphere sizes. The average aspect ratio obtained at all sizes was of 0.28 ± 0.03 for the inner ring and 0.41 ± 0.03 for the outer ring. Therefore, the ratio of the diameters for the outer and the inner ring must also remain constant (D_{outer}/D_{inner} ~1.46) and both rings should be regarded as replicas of the template spheres.

The quality of the double ring patterns remained high over macroscopic dimensions (~1 cm^2). This lithographic technique, however, is subject to the same types of defects found in all assays which employ monolayer arrays of hexagonally packed spherical particles. Namely, missing features are occasionally observed as well as line defects.[73] The domain size for well-ordered double ring arrays in the present experiments were approximately 25 μm × 25 μm. It is, however, difficult to discern individual double ring features from images with wide fields of view because of the narrow width of individual rings as well as the small gap between them. The details of individual double rings can still, however, be made out in 10 μm × 10 μm images when the template sphere diameters are 1 μm or larger (Figure 4.4).

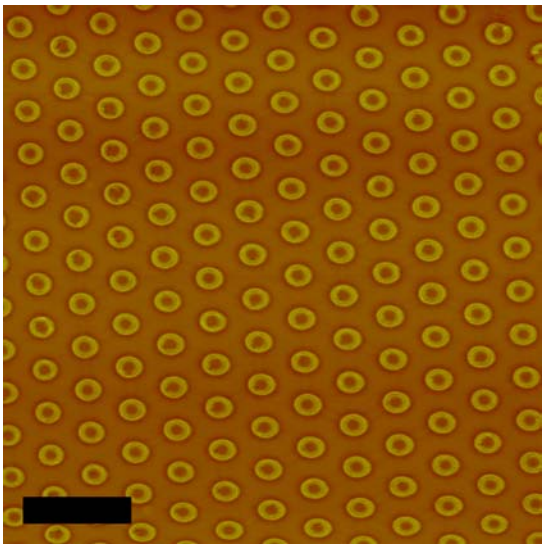

Figure 4.4. 10 μm × 10 μm AFM image of double-ring features fabricated by applying 1 μm polystyrene spheres. Scale bar: 2 μm.

Controlling the Gap

The gap, *d*, between the two concentric rings could be fine-tuned by adjusting the acetone concentration in the polystyrene sphere suspension solution. Figure 4.5 shows a series of 2 μm × 2 μm AFM images as the concentration of acetone is increased stepwise from 0 to 30% by volume. In this case the size of the template spheres was fixed at 800 nm. The height of the outer and inner rings increased substantially with acetone concentration. Moreover, the width of the inner ring also expanded, while the position of the outer ring showed less dramatic changes. This meant the gap between the inner and outer ring shank with increasing acetone concentration. Without acetone, the interval between rings was 94 nm, as shown in Figure 4.5A. As the acetone concentration increased, this distance narrowed to 48 nm for 10% acetone and to 38 nm for 20% acetone. At 30% acetone, the inner and outer rings nearly merged together, which left a single ring with a thicker width as shown in Figure 4.5D. The hexagonal geometry of the double rings, however, remained unaffected. This was expected since the array spacing was inherited from the hexagonal packing of the template sphere, which was unaffected by acetone concentration.

Forming Single-Ring Features

A critical aspect of forming double-ring features involves the use of hydrophobic template spheres. If hydrophilic silica spheres were used instead, then only single rings were formed. Figure 4.6 shows a side-by-side comparison of results for 1 μm spherical templates of polystyrene and silica. Both samples were made from solutions containing

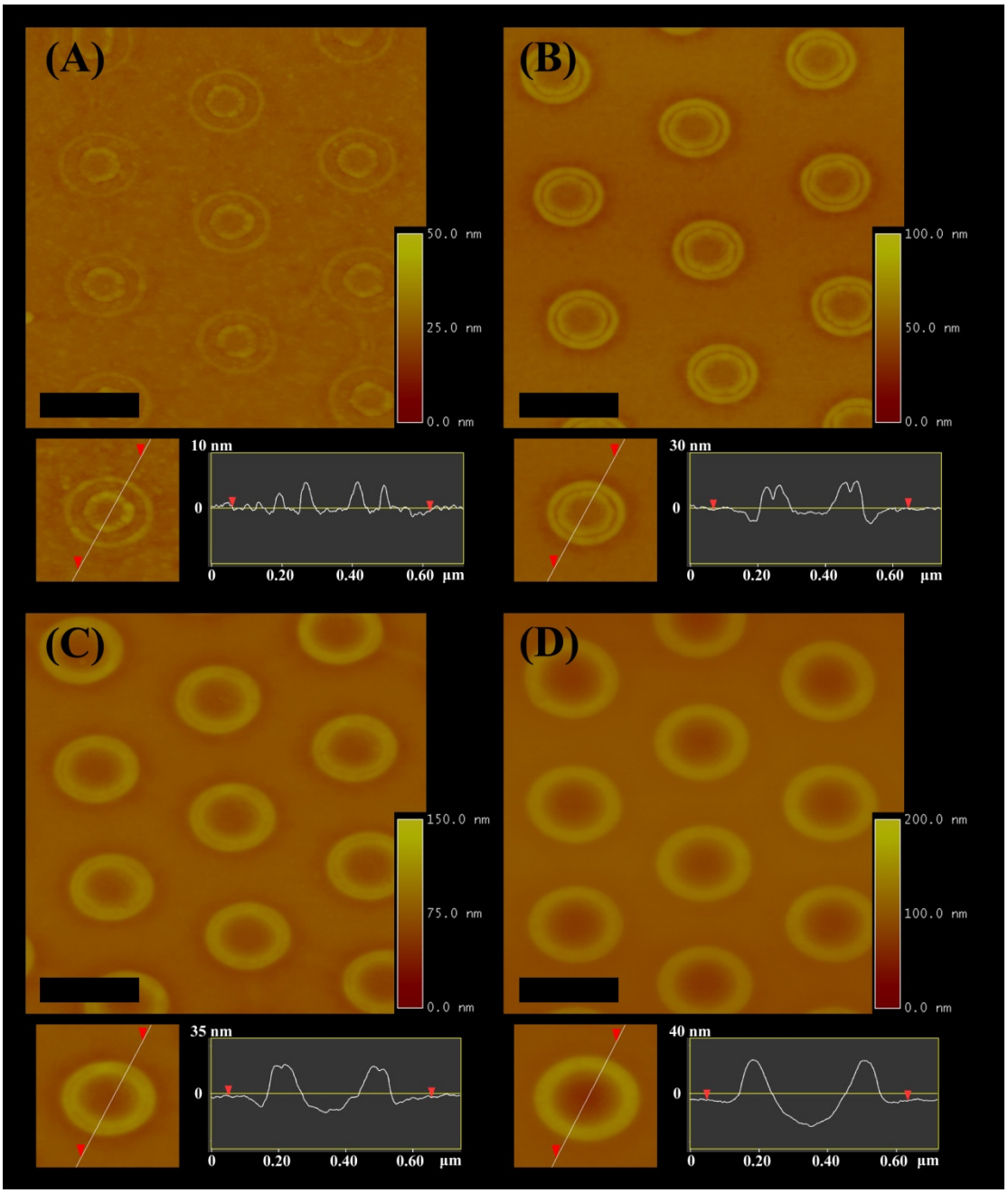

Figure 4.5. A series of 2 µm × 2 µm AFM images showing the effect of acetone concentration on double rings formed from 800 nm polystyrene spheres with (A) 0 %, (B) 10 %, (C) 20 %, and (D) 30 % acetone by volume. Scale bars: 500 nm.

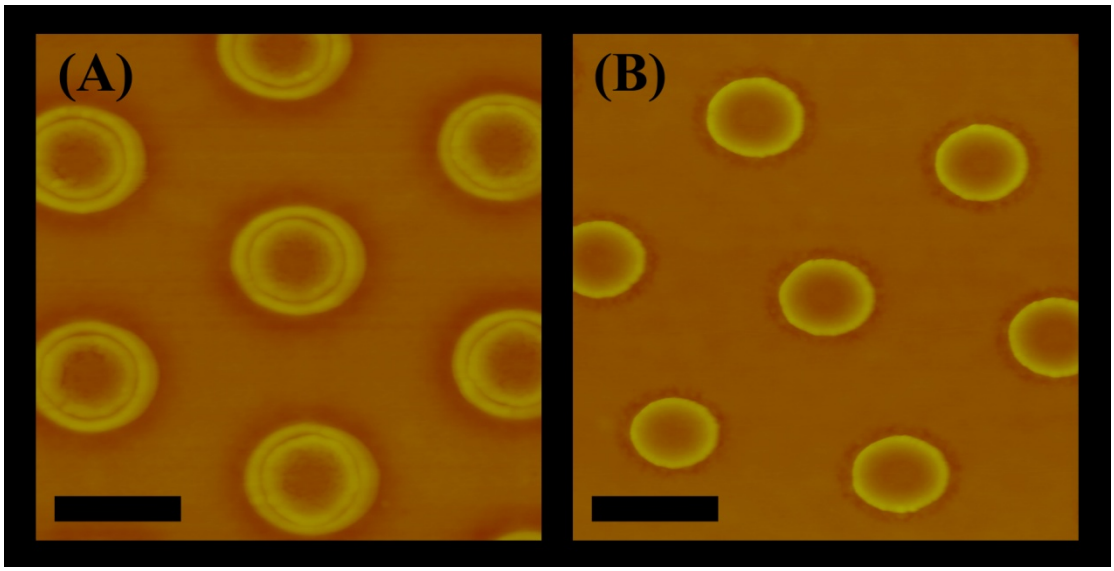

Figure 4.6. 2 μm × 2 μm AFM images of polymer features fabricated by (A) 1 μm polystyrene, and (B) 1 μm silica spheres. Scale bar: 500 nm.

10% acetone by volume. A double-ring array was formed from the polystyrene spheres, but silica spheres yielded single-ring features. Significantly, the diameters of the single rings matched those of the inner ring from polystyrene. It should be noted that we also tried different substrate materials such as SU-8 and polyethylmethacrylate instead of Shipley 1805. In each case, double-ring features were obtained when using polystyrene spheres, but single rings were formed when silica spheres were employed.

Mechanism for Double Ring Formation

The data in Figures 4.3, 4.5, & 4.6 suggest that the inner and outer rings of individual double-rings were produced by two different mechanisms. A schematic representation of our proposed ring formation mechanism with polystyrene spheres is shown in Figure 4.7A. Under this model the use of a dilute acetone solution leads at first to slight amount of material being dissolved from the spin-coated Shipley 1805 layer. As the solvent evaporates the acetone/water solution becomes saturated with polymer. The last stage of evaporation leads to polymer precipitation back onto the substrate. The precipitation is localized to the region around the base of the polystyrene spheres because this is the last location from which solvent evaporates. Such a process should form the outer ring in a manner analogous to the phenomenon by which coffee becomes enriched at the outer edge of a coffee stain.[145-147]

By contrast, the inner ring is most likely the result of a surface tension effect. This idea is consistent with the observation that the inner edge of the inner ring outlines a segment of a circle which has a diameter corresponding exactly to that of the template

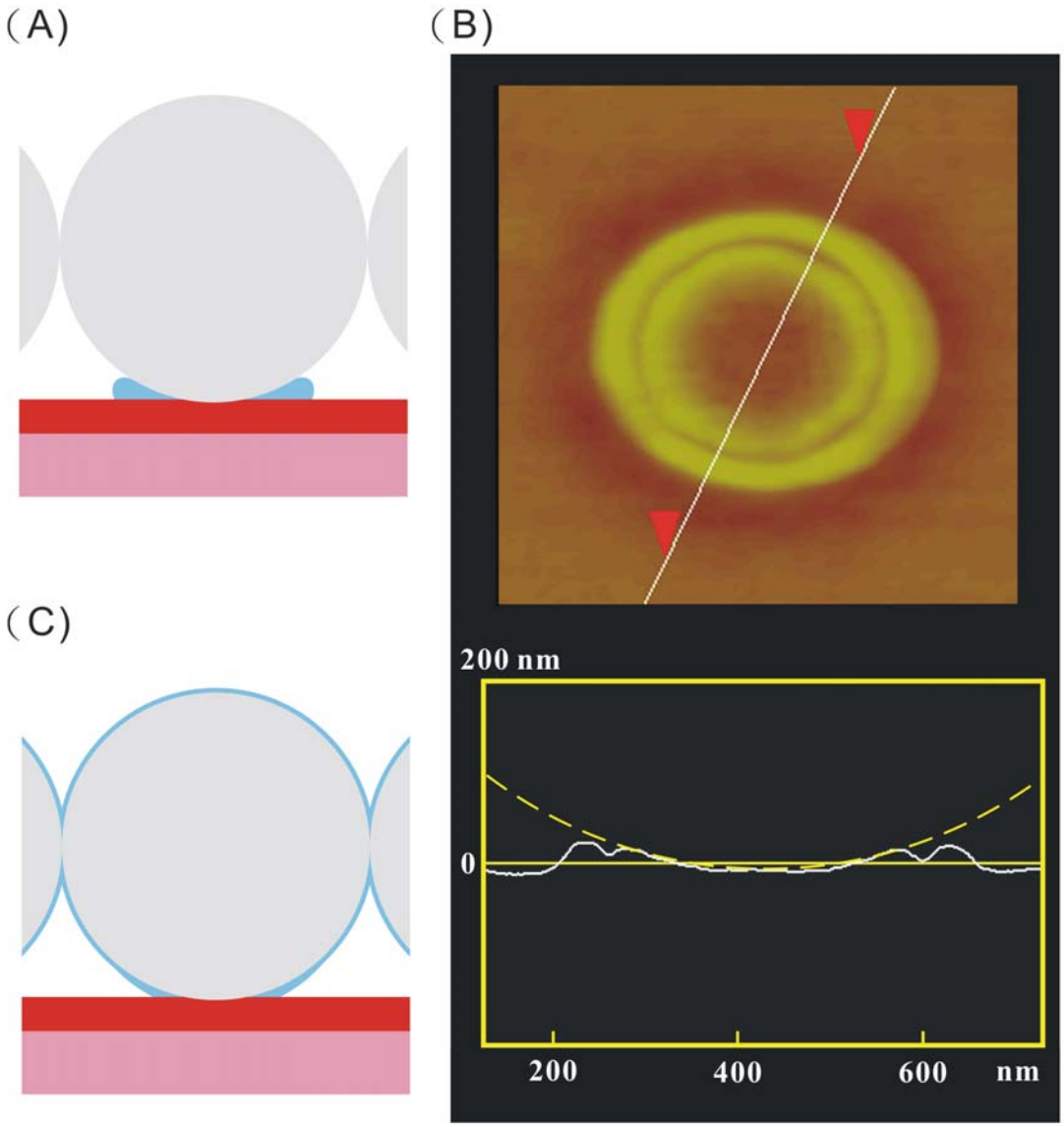

Figure 4.7. (A) Schematic diagram of the putative final step of the templated evaporation process with polystyrene spheres. (B) AFM image and line profile of one double-ring feature fabricated by a 1 μm polystyrene sphere. The dashed yellow line is an overlay of the outline of a 1 μm sphere on the line profile. (C) The putative final step of the template evaporation process with silica spheres.

spheres (Figure 4.7B). Therefore, the inner ring appears to be formed when acetone softens the photoresist layer and allows the polymer sphere to partially mold around it. This presumably occurs because it lowers the surface energy at the solvent/substrate interface.

The effect of acetone concentration provides corroborating evidence for the proposed double-ring formation mechanism. Acetone is a better solvent for Shipley 1805 than water. Therefore, more material should dissolve into solution as the acetone concentration is increased. Consequently, more material precipitates from solution upon solvent evaporation. This causes an increase in mass to be found at outer ring. The higher acetone concentration also leads to a greater softening of the photoresist layer. This in turn causes the polystyrene spheres to mold more deeply into the spin-coated film. Both of these effects cause increases in feature height and the deeper embedding of the spheres leads to a shrinking of the gap between the rings as can be seen from the line profiles in Figure 4.5.

Both the polystyrene spheres and the underlying photoresist substrate were hydrophobic. This should cause a liquid toroid to form uniformly around the base of the sphere during the last step of solvent evaporation (Figure 4.7A). However, when silica was employed instead, the final stage of the drying process should be markedly different. In this case, the remaining liquid should preferentially coat the silica spheres and avoid the hydrophobic substrate (Figure 4.7C). Under these circumstances, the photoresist precipitated out onto the spheres. Once the spheres were sonicated away, the material left on the surface would be expected to shadow its original dimensions.

Forming Gold Double Rings

Polymeric double-ring arrays could be employed as templates to create corresponding features in an underlying metal film. As a demonstration, we transferred double-ring features to a gold layer. The idea is shown schematically in Figure 4.8A. First, double-ring features were fabricated in photoresist on top of a Au film. For this purpose, a 20 nm Au layer was evaporated onto a 3 nm thick Cr layer coated onto a glass substrate (BOC Edwards Auto 306 Metal Evaporation Chamber). A 1:20 dilution of Shipley 1805 photoresist was coated onto the surface to a thickness of 20 nm and 1 μm polystyrene spheres were used as the evaporation templates. The solvent was pure water.

After the formation of the polymeric features, the chip was dried and placed into a 25 W oxygen plasma for 32 sec with 0.2 Torr O_2. This should uniformly remove the outer most layers of photoresist. In fact, photoresist should only remain in raised locations where templating had taken place. At this point the chip was immersed into a 1:200 (volumetric) diluted aqueous Au etching solution (NaI/I_2) for 40 sec to conduct a wet chemical etch. Finally, the chip was washed with copious amounts of deionized water and acetone to remove the photoresist. This procedure should leave only gold rings on the surface. In fact, AFM imaging revealed a hexagonal array of double rings on the surface (Figure 4.8B). The width of each ring was 29 nm. The outer ring had a diameter of 384 nm, while the inner ring diameter was 238 nm. The spacing between concentric rings was 73 nm and the adjacent ring distance was 1 μm.

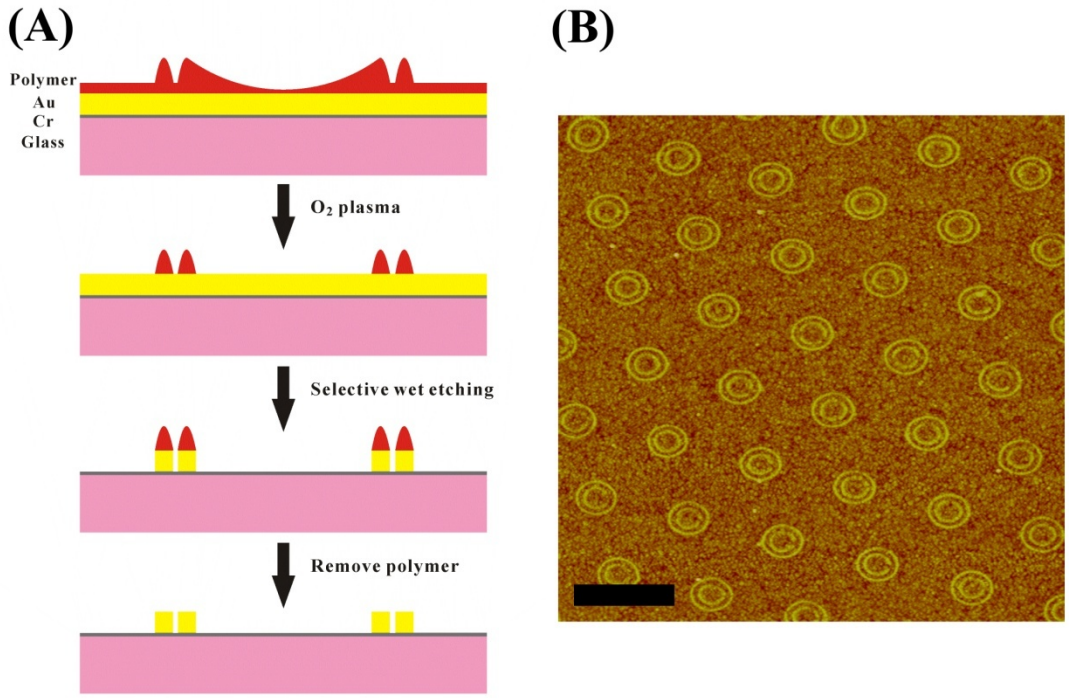

Figure 4.8. (A) Schematic diagram of Au double-ring formation. (B) 5 μm × 5 μm AFM image of hexagonally arrayed Au double rings fabricated from 1 μm polystyrene spheres. Scale bar: 1 μm.

Conclusion

We have demonstrated a simple patterning technique, water stain lithography, to fabricate well-ordered nanoscale single and double-ring features in photoresist and Au. The ring size and spacing could be controlled by tuning the size of the template spheres and adjusting the acetone concentration in solution. This technique provides the possibility to fabricate large arrays of patterned features in a highly reproducible fashion with line widths well below 100 nm. Although spherical templates were used in these experiments, other shapes such as elongated nanorods should also be possible.

CHAPTER V

EVAPORATIVE TEMPLATING IN CONFINED GEOMETRIES

Introduction

Irreversible solvent evaporation has recently received interests from scientists and engineers because of its potential applications in fabricating useful features. These features could be successfully applied to electronics, photonics, and biotechnology related fields.[1, 3, 5, 6, 8-10, 14, 155] The non-conventional patterning phenomena provide an alternative route for fabricating large area features in a simple and inexpensive way. This straightforward process has been employed to create patterns of nonvolatile dispersed solute particles via the dynamic self-assembling.[145-147] However, the lack of precise control over size, spacing, and periodicity of the patterns created restricts its potential applications. These limitations could be due to instabilities in the evaporation process.[148] Recently, the use of a solvent evaporation process has been successfully demonstrated in fabricating micron-scale features via mechanical methods.[149-151, 156] In the mean time, utilizing this evaporation phenomena and a different fabricating procedure we have successfully produced nano-scale patterns with relatively precise control over size, spacing, and periodicity for the first time.[157]

Water stain lithography (WSL) combines the features of template confinement and the irreversible evaporation process. This process allows the creation of large areas with single or twin minute geometries of confined water stains. The strategy of preparing

nanoring-like structural arrays is shortly described as follows. A layer of polymer was first spun on top of a solid substrate, as shown in Figure 5.1. After this, a monodispersed sphere suspension solution, which was premixed with a surfactant solution, was introduced dropwise onto the surface. The solvent was then allowed to evaporate completely. Following this, the template spheres were removed by bath sonication in deionized water. The nanoring-like feature arrays patterned on the surface were then dried by N_2. The whole process could be accomplished within about 90 min with very simple equipment and under ambient conditions. Feature line-widths of <30 nm were easily achieved with this method. Furthermore, the specific geometry of double-ring features could also be precisely controlled by varying experiment conditions during fabrication.

Although the uses of this technique have been successfully demonstrated, systematic studies of confining water stains in nano-scale have not been sufficiently investigated. In this paper, we present a more detailed analysis of the water stain confinement strategy. We found that both the existence of surfactant in the working solution and the relative humidity played an important role in controlling the feature formation. Furthermore, a diversity of nano-size geometries could all be easily prepared by manipulating these parameters. Nanosingle rings, nanodouble rings, nanotriple rings, nanotargets, and nanoholes could all be simply fabricated. In addition, a <15 nm line-width was achieved by moderately adjusting experiment conditions.

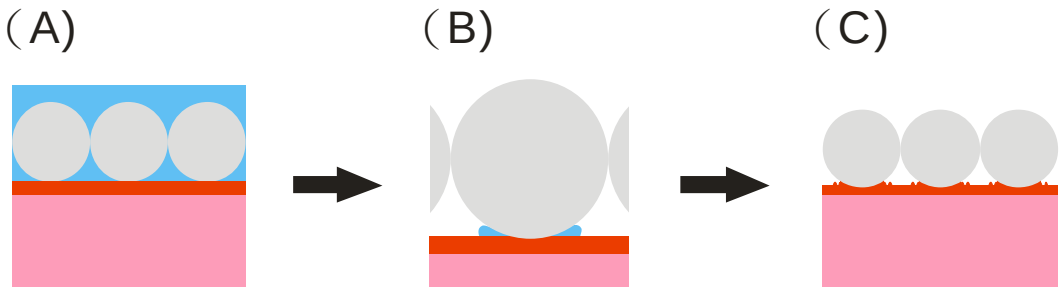

Figure 5.1. Schematic diagram of the double-ring features fabrication. (A) Polystyrene spheres are spread on top of a polymer spun-coated substrate. (B) The last stage of drying process on the surface. (C) The double-ring features were formed surrounding the template spheres when the solvent was gone.

Experimental Section

In these experiments, a glass slide coated with 50 nm Au was chosen as the substrate. The substrate was then spun-coated with Shipley 1805 polymer producing a 20 nm thick layer. The templating polystyrene spheres (Duke Scientific, CA) were first pretreated by repeated washing, sonication, and centrifugation in deionized water (10 times) to remove existing surfactant from the suspension solution. (Note: The original existing surfactant in the sphere suspension solution may affect the result.) After the cleaning procedure, a 10.0 μL solution containing suspended monodispersed polystyrene spheres was mixed with a 10.0 μL aqueous solution containing a certain concentration of the selected surfactant. This solution was then gently spread onto the substrate dropwise, and the whole slide was allowed to dry in a closed system which was maintained at a specific relative humidity. After the substrate dried, the whole slide was placed into a water bath to sonicate off the template spheres, and then dried by N_2.

Results

Inside a drying droplet, the existence of internal capillary flow moves the solute to stack at the edge of the droplet and thus cause the characteristic ring shaped coffee stain.[145] In order to precisely confine the resulting staining process in nano-scale, highly uniform templates were utilized. In addition, a surface dissolving solvent was applied to partially dissolve the polymer surface which provided the ring stain material. In this section the effects of surfactants and environmental relative humidity on the confinement of water stains will be demonstrated.

The Existence of Surfactants

Figure 5.2 demonstrated the use of surfactant in water stain confinement for nano-ringlike structure formation. It is important to note that several interesting features such as small single rings, large gap double rings, small gap double rings, large single rings, nanotargets, and nanoholes could all be produced by simply tuning the surfactant content in solution. In order to make accurate comparisons, only the surfactant concentrations were varied while all the experiment conditions and sample preparation methods (e.g. relative humidity, substrate, sphere size, etc.) were kept the same as described in experimental section.

In this segment of experiments the surfactant Triton XQS-20 (Sigma-Aldrich, MO) was added in varying concentrations (by mass) and the relative humidity was fixed at ~ 60%. As can be seen in Figure 5.2A, a very low concentration of surfactant (0.001%) would only cause the formation of small single-ring features. As the surfactant concentration was elevated to 0.0015% the double-ring features began to appear, Figure

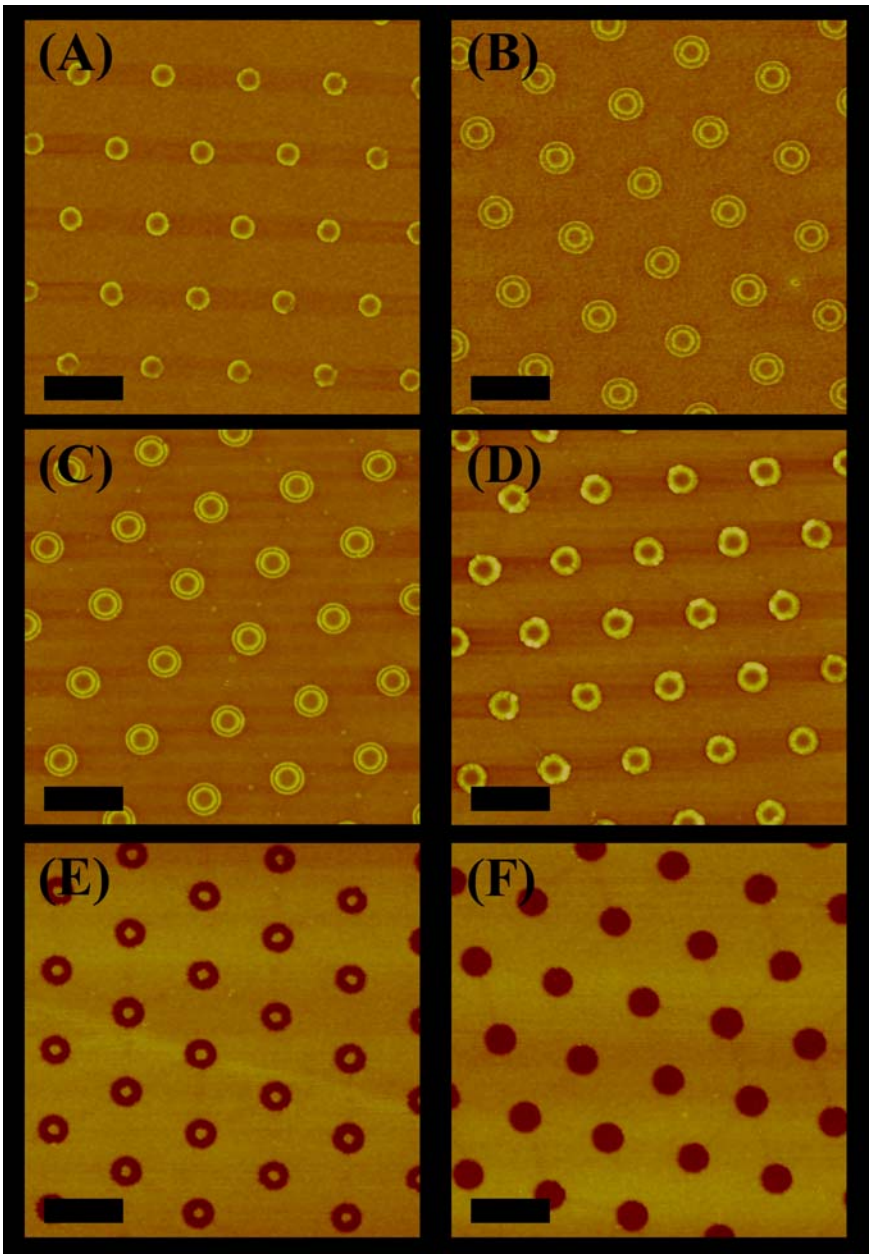

Figure 5.2. The influences of surfactant content in nanoring-like feature formation. 5 μm × 5 μm AFM images showing features fabricated by applying 1 μm polystyrene spheres containing different concentration of Triton XQS-20 surfactant: (A) 0.001 % (B) 0.0015 % (C) 0.002 % (D) 0.003 % (E) 0.004 % (F) 0.006 %. All experiments were maintained in a ~60 % relative humidity. Images are at the same height scale. Scale bars: 1 μm.

5.2B. By increasing the surfactant concentration further (0.002-0.003%), the gap (d) between two concentric rings would shrink and the two rings would eventually merge into larger single rings, Figure 5.2C-5.2D. By elevating the concentration of surfactant to 0.004% nanotarget features could be formed, Figure 5.2E. Finally, nanohole features were produced by using a surfactant concentration of 0.006%, Figure 5.2F. A detailed discussion of the mechanism believed to be responsible for the production of these features will be presented later.

We have also independently tested different types of commonly used surfactants, results summarized in Table 5.1. It is important to know that many kinds of surfactants were suitable for making double-ring-like features. Independently, different surfactants have different abilities to dissolve the polymer surface. Each surfactant demonstrated its own optimum working range of both concentration and relative humidity for double-ring-like feature formation. In addition to surfactants with complex structures, we also examined a surfactant with relatively a simpler structure, sodium docusate, regularly used as stool softer. It was observed that even a simple structure surfactant worked with this technique. Finally, we also tested common hand-washing soap that also contained certain mixtures of industrial surfactants. Double-ring features were produced by the hand-washing soap as well. These results provide the evidence that this nano-scale patterning technique could be performed with inexpensive reagents.

It is interesting to note that the gel-like surfactants would simply cause the formation of double-ring features. However the salt-like surfactants, such as sodium dodecyl sulfate (SDS) and sodium ethyl sulfate (SES), were not suitable to form these

features. The salt-like surfactants would crystallize on the surface during solvent evaporation. This crystallization of surfactants interrupts the final solute precipitation process preventing the formation of the double-ring features.

Table 5.1. Different types of surfactants tested for double-ring feature formation.

1. Dial is a trade make of The Dial Corporation.

Surfactant	Surfactant Type	Double-ring formation
Tween 20	Polyoxyethylenesorbitan monolaurate	Yes
Triton X-100	Octylphenol ethoxylate	Yes
Triton X-200	Polyether sulfonate	Yes
Triton XQS-20	Phosphate polyether ester	Yes
Triton QS-15	Polyether sulfate	Yes
Triton QS-44	Polyether phosphate ester	Yes
Sodium Docusate	Sulfosuccinate	Yes
Dial Soap[1]	Mixture	Yes
SDS	Sodium Dodecyl Sulfate	No
SES	Sodium Ethyl Sulfate	No

The Influence of Relative Humidity

Inside a drying droplet, the evaporation speed occurring at the edge dominates the whole drying process.[145-147] The control of solvent evaporation rate in the droplet plays an important role in feature formation. By controlling relative humidity in the sample environment one can cause alteration of the droplet evaporation speed, and thus a systematic study of the effect of humidity on feature fabrication was performed. An interesting relationship was observed between feature formation and relative humidity, Figure 5.3.

The experiment conditions and sample preparation methods were kept consistent while only the relative humidity parameter was fluctuated. In this series of experiments 0.002% Triton XQS-20 was utilized. Figure 5.3A-5.3D demonstrates the difference in fabricated features produced under various relative humidities. This study revealed that only single-ring features would form when the relative humidity was <40%. As the humidity was increased, double-ring features were formed. The mechanism by which relative humidity impacts feature formation will be discussed in a later section.

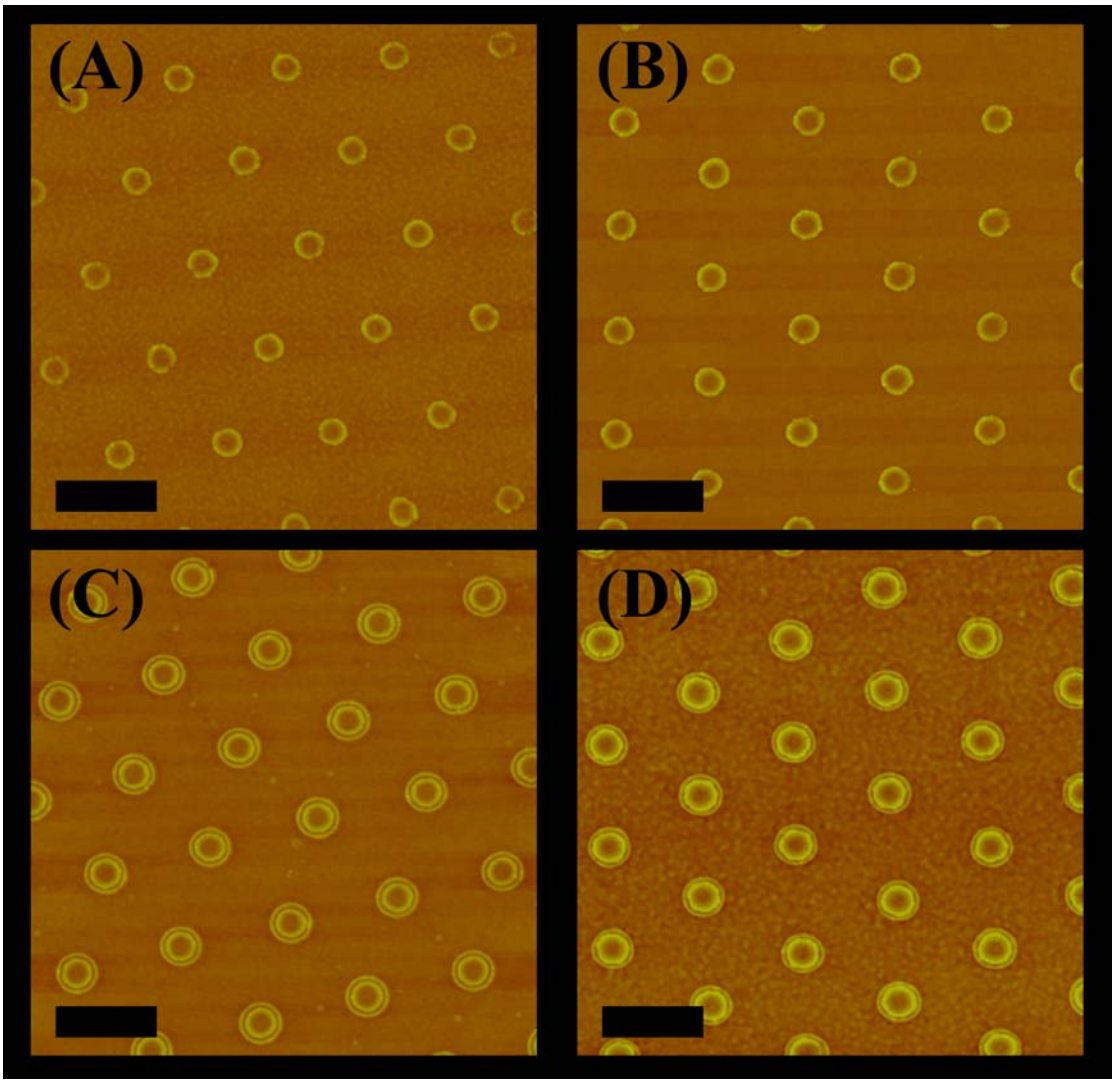

Figure 5.3. 5 μm × 5 μm AFM images showing the influences of relative humidity in feature formation: (A) 20 % (B) 40% (C) 60 % (D) 80 %. All experiments were accomplished by 1 μm polystyrene spheres with 0.002 % of Triton XQS-20 surfactant. Images are at the same height scale. Scale bars: 1 μm.

Features at Very High Humidity

When the relative humidity was maintained at a very high level (~90%), a similar trend in feature morphology was produced as in the lower humidity systems (~60%), Figure 5.4. As previously observed, the features changed from small single rings to double rings, and finally to large merged single rings via higher surfactant content. However, a novel morphology appeared when 0.001% Triton XQS-20 was used in a 90% relative humidity atmosphere. These unique conditions produced a triple-ring feature as shown in Figure 5.5.

Real-time Observation of Double Ring Formation

In order to capture the double-ring feature formation process, we designed a real-time experiment under a standard optical microscope. In order to observe the progression of this process on the surface, a transparent glass slide coated with ~ 200 nm Shipley 1805 polymer was chosen as the supporting substrate. A 20.0 μL aqueous solution containing monodispersed 50 μm polystyrene spheres and 0.02 % Triton XQS-20 surfactant was then spread onto the substrate. This system was evaporated in a ~98 % relative humidity environment. This drying process was monitored from the backside of the substrate by a standard inverted epifluorescence microscope. (Eclipse TE2000-U, Nikon; Sensys CCD, Princeton Instruments, NJ) Since the Shipley 1805 polymer was a fluorescent material, the surface substance movement could be simply monitored by this fluorescence microscope setup.

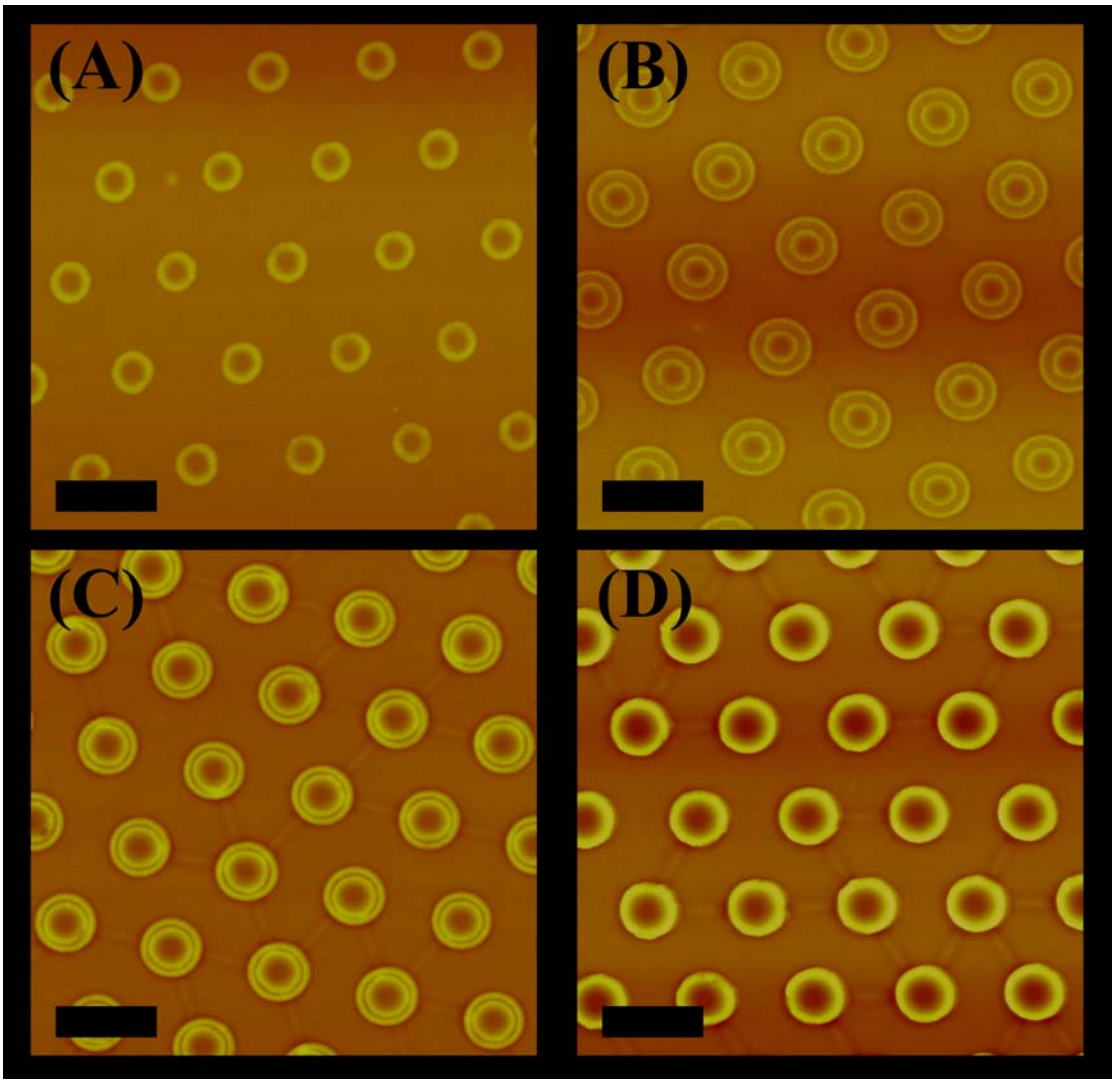

Figure 5.4. The influences of surfactant content in nanoring-like feature formation. 5 μm × 5 μm AFM images showing features fabricated by applying 1 μm polystyrene spheres containing different concentration of Triton XQS-20 surfactant: (A) 0.0005 % (B) 0.0025 % (C) 0.005 % (D) 0.01 %. All experiments were maintained in a ~90 % relative humidity. Images are at the same height scale. Scale bars: 1 μm.

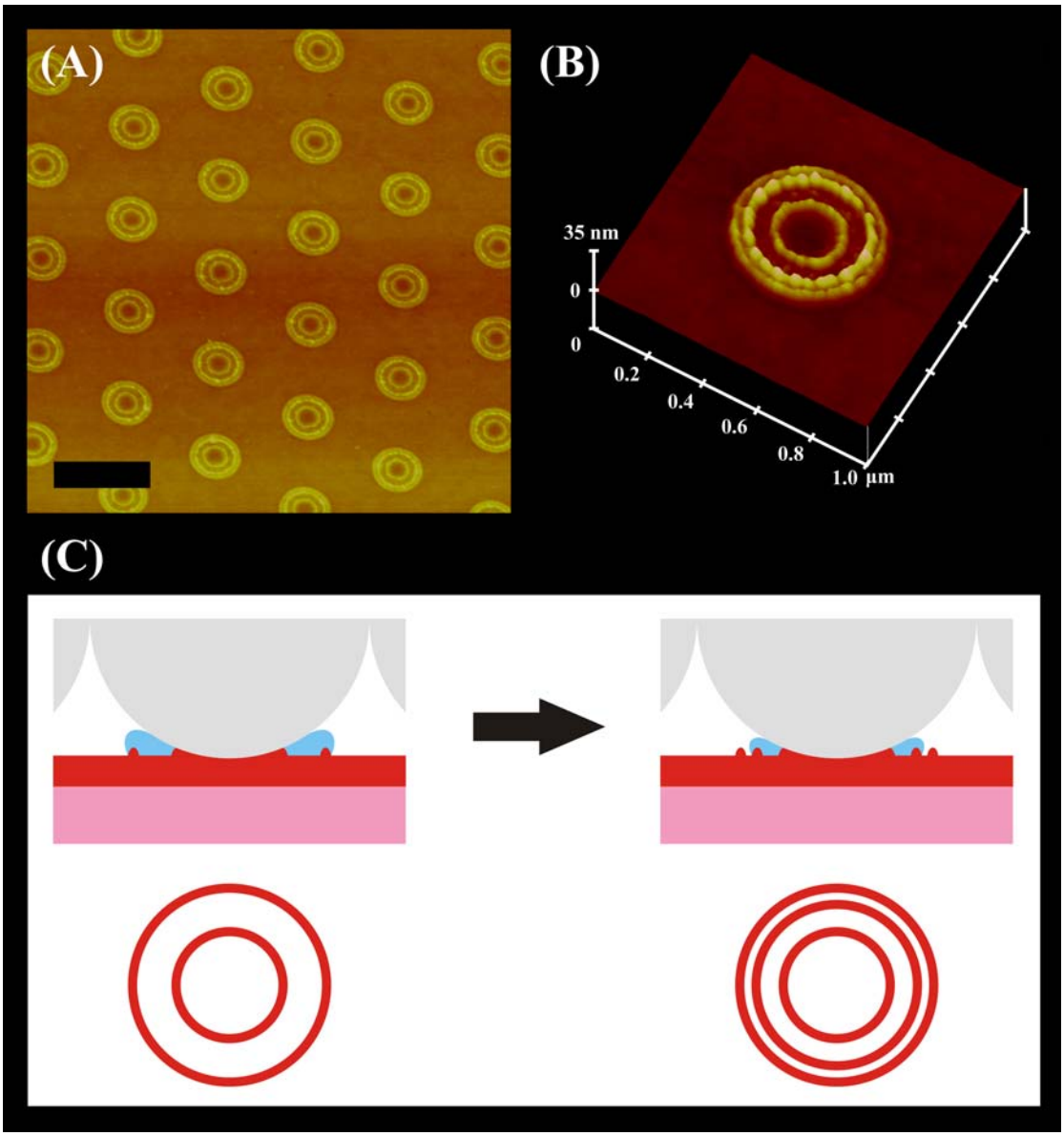

Figure 5.5. (A) 5 µm × 5 µm AFM image showing triple-ring feature array fabricated by 1 µm polystyrene spheres with 0.001% Triton XQS-20 surfactant at 90 % relative humidity condition. Scale bar: 1 µm. (B) A zoom-in AFM image of a triple-ring feature. (C) Schematic demonstration of the formation of triple rings.

Figure 5.6 demonstrates the real-time gradual drying process of the polymer surface. The right column contains schematic representations of the actions occurring at the surface for each respective row of images. Since the relative humidity was maintained at a very high level, the solvent evaporation occurred very slowly. Figure 5.6A was a fluorescence image captured after 14 hours and 52 min of drying. The hexagonal close packing of the polystyrene spheres has been maintained at this moment, indicated by the dark regions in the picture. The brighter parts of this image represent the remaining solution filled spaces. Figure 5.6B shows the surface morphology present 3 min after Figure 5.6A. The drying liquid caused the contrast change in the brighter solution filled spaces due to light refraction. Simultaneously, small single-ring features began forming at the inner ring position below the template spheres. After 5 more minutes, continuing evaporation induced contraction of surface liquid, as seen in the right and left corners of

Figure 5.6C. In the following 2 minutes, Figure 5.6D-5.6E, the remaining solution began accumulating around the outer boundaries of each spherical pattern. An interesting observation was that the remaining water bridges between adjacent spheres caused the formation of parallel double lines. It is important to note that the surface features discussed thus far in this figure are nearly saturated liquids and not solidified patterns. As evaporation proceeded, the liquid regions continued to recede towards the template spheres, Figure 5.6F. The parallel double lines merged into single lines between the spheres. As the remaining solution became saturated material started to precipitate back to the surface, leading to the production of the double-ring features. Upon complete evaporation, the water bridge lines broke and solidified double-ring features were formed, as shown in Figures 5.6G-5.6H. The time lapse images of this process, shown in Figure 5.6, were taken from a movie available in the supporting material.

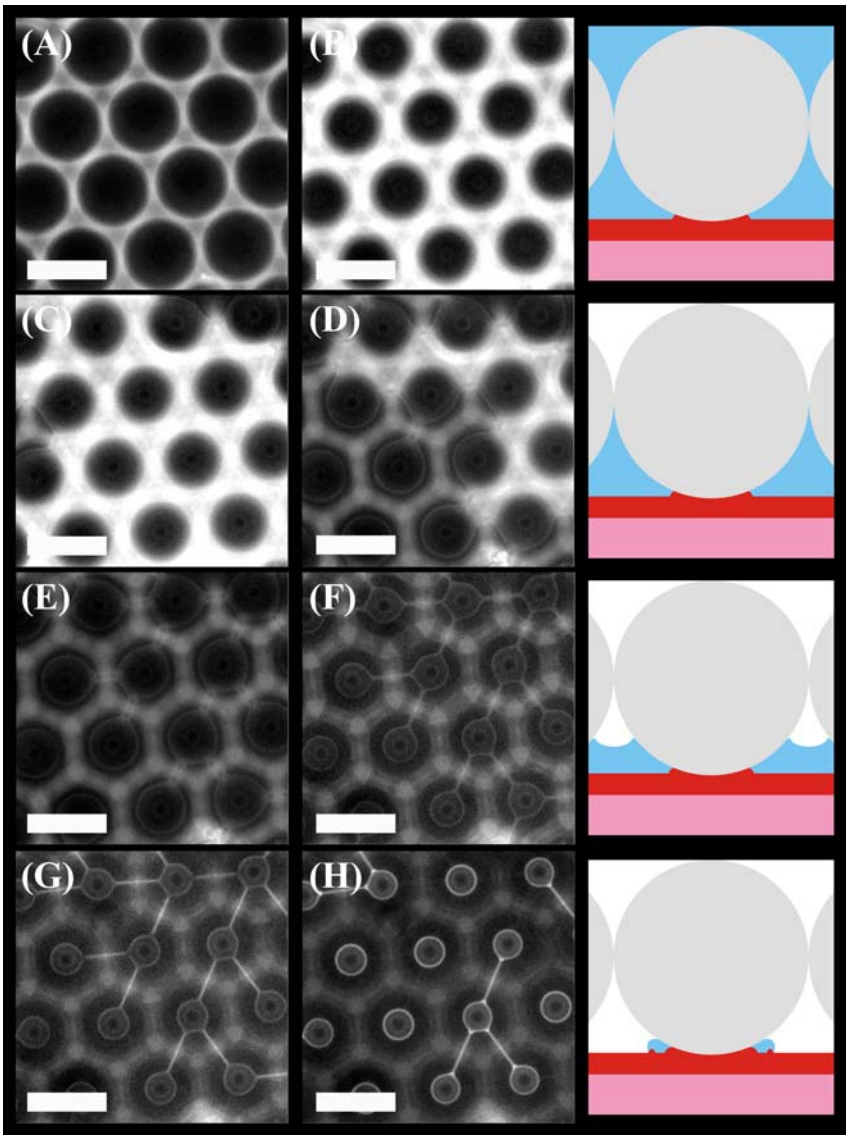

Figure 5.6. Fluorescence images showing double-ring feature formation process at different time scale after starting drying: (A) 14 hours 52 min (B) 14 hours 55 min (C) 15 hours (D) 15 hours 1 min (E) 15 hours 2 min (F) 15 hours 9 min (G) 15 hours 22 min (H) 15 hours 52 min. The right column demonstrated the corresponding surface situations, independently. The experiment was performed by applying 50 μm polystyrene spheres with 0.02 % of Triton XQS-20 surfactant at ~98 % relative humidity. Scale bar: 50 μm.

Discussion

Confining Water Stains in Nano-Scale

Our experimental results indicate several important factors dominating the confinement of water stain geometries. Existence of surfactant, surfactant type and amount, and environmental relative humidity are all major coefficients of confining water stains in nano-scale.

In the double-ring features, the inner and outer rings of individual double-rings were produced by two different mechanisms.[157] It has been shown that an increase in surfactant concentration increases the amount of surface polymer layer dissolved. As solvent evaporated, the solution became saturated and polymer precipitated back onto the surface. The polystyrene sphere template positions were the last place where the remaining solution localized. The following precipitation was thus restricted to those regions. The schematic representation of our proposed ring formation mechanism was shown in Figure 5.1B. The polystyrene spheres and the underlying polymer substrate were both hydrophobic. This led to a liquid toroid forming around the base of the sphere during the last moments of solvent evaporation. Consequently, solute would stack at the outer edge of this liquid toroid once precipitation began, producing the outer rings of the double-ring features.

On the other hand, the production of the inner ring is believed to be dominated by surface tension effects. It was observed that the inner edge of the inner ring exactly corresponds to the template sphere's arc.[157] Therefore, the inner ring features could be treated as a print of the templating spheres on polymer surface. It is believed that when

surfactant softened the polymer layer, the template sphere sank into the polymer producing a mold around it which gives rise to the inner ring. [152, 157]

The formation of a toroidal liquid region in this process, via the use of a hydrophobic template, would lower the surface energy at the solvent/substrate interface. On the contrary, the final stage of the drying process should be markedly different when hydrophilic templates are employed instead. The remaining liquid should preferentially coat the hydrophilic spheres to avoid the hydrophobic substrate.[157] This caused the polymer to precipitate out onto the sphere's surface, and the material left on the substrate surface would be expected to silhouette its original dimensions. This led to the formation of only single-ring features when surfactant was applied to the system with silica spheres at any relative humidity.

The Role of Surfactant

Since the surfactant has the ability to dissolve the polymer surface, the existence of surfactants in the system would dominate the geometric parameters in water stain confinement. The major role of the surfactant was the ability to bring the surface material into solution. The ability of surfactant to dissolve the polymer surface led to the surface molding and water staining effect. As presented in the previous section, Figure 5.2 and Table 5.1, various amounts and types of surfactants successfully produced well confined water stain features.

The formation of double-ringlike features was believed to form by two major mechanisms. The inner ring was mainly caused by the surface tension effect. The outer

ring was formed by coffee stain effect instead. Both phenomena were based on the partial dissolving of the polymer surface. As a control concentrated surfactant alone was shown to easily dissolve the polymer surface, results not shown. Since surfactant can soften and dissolve the polymer surface, the inner rings formed first during the drying process underneath the template spheres as they slightly mold into the surface. When surfactant concentration was low (0.001%), only a little material was dissolved from the polymer surface, Figure 5.2A. The dissolved material was not rich enough to form obvious outer ring features when precipitated. This caused the single rings produced to resemble the inner rings of the double-ring features. When higher surfactant concentration was utilized (0.0015%), outer rings could be easily observed as well, Figure 5.2B. This was because the remaining toroid liquid, commonly formed between the hydrophobic template and the surface, contained a sufficient amount of dissolved material to form a clearly visible coffee stain edge upon evaporation.[145, 157] When the surfactant content was elevated to 0.002%, Figure 5.2C, the change of the inner ring's diameter became increasingly obvious while the outer ring experienced insignificant change, which therefore shrunk the gap, *d*, between the two concentric rings. In addition, the thickness and height of the walls were also substantially enhanced. When the surfactant concentration reached 0.003%, there was an increase in the amount of dissolved polymer deposited on both the inner and outer rings. This concentration of surfactant also caused the template spheres to sink further into the polymer. The synergy of these phenomena are believed to cause the merging of the two rings, forming a thicker single ring, as shown in Figure 5.2D.

The formation of the nanotargets at a surfactant concentration of 0.004% is believed to occur by the disintegration of the polymer regions immediately surrounding the template spheres during the sonication step. The precipitating material stacking on the surface is believed to consist of both polymer and surfactant, which decreases the structural integrity of this stacked region. The decrease in structural integrity allows this region to delaminate from the surface when exposed to water bath sonication. However, the contacting point between the sphere and polymer surface was protected from this phenomenon. After sonication the disk left behind in the center of the trench feature produced the nanotarget feature shown in Figure 5.2E. Finally, at a surfactant concentration of 0.006% the protection provided by the contact point diminishes, which allows for the dissolving of the regions centered below the template spheres. Consequently, a nanohole feature was left on the surface, Figure 5.2F.

An important role of surfactant in the drying process was its edge pinning ability.[158, 159] This edge pinning effect is most commonly seen in the structure of coffee stains on surfaces.[146, 147] In our system, we believe the existence of surfactant helped to pin down the remaining liquid edge which maintained a lower contact angle for the remaining liquid. This effect oriented the stacking of precipitating materials toward the fixed droplet edge and thus formed the outer-ring features.

Surfactant protection on the droplet surface should theoretically slower the evaporation rate in a droplet.[160, 161] However, the inverse was observed. When two droplets maintaining the same total volume were spread on the surface over the same initial area, faster evaporation was observed in the drop containing the higher

concentration of surfactant.[159, 162, 163] After 30 minutes of evaporation under ambient conditions, the higher surfactant system displayed a smaller droplet contact angle and a more flat droplet shape.[159, 160, 163, 164] In addition the edge remained pinned to its original position. On the other hand, the system with less surfactant kept a higher contact angle and the droplet edge retracted on the hydrophobic surface. The system with the higher surfactant content also became completely dry the fastest, probably due to the increased evaporative surface area. This observation supported the pinning effect caused by surfactants, and was consistent with the outer ring formation in the double-ring feature.

Influence of Relative Humidity

Another important factor in controlling water stain formation was the relative humidity of the working environment. As previously mentioned, the remaining surface liquid would form a toroidal shape to reduce the surface tension when hydrophobic templates were applied. It was observed only single-ring features would form when the relative humidity was kept <40%, Figure 5.3A-5.3B. This is because evaporation rates are inversely proportional to environmental relative humidity. The accelerated evaporation does not allow time for the dissolved species to precipitate out before the remaining liquid's edge has retreated to the position of the inner ring. Thus the outer ring is virtually unobservable under these conditions and only an inner ring is observed. On the other hand, when higher humidity conditions (~60-80%) were applied, evaporation was slow enough to allow the dissolved species to precipitate out at the liquid's periphery producing the double-ring features, Figure 5.3C-5.3D.

It is also important to note that the relative humidity would also alter the ring diameters, feature heights, and ring wall thickness. This was again related to the extended duration of evaporation. These three parameters are produced from the deposition of dissolved materials. An increase in evaporation time allows more material to be dissolved into solution and permits more deposition to occur in the designated regions. Also the extended evaporation time enables the template spheres to sink further into the softened polymer surface causing the enlargement of both inner and outer rings. In addition, the wall thickness and heights were also increased by these phenomena.

The Spontaneous-Stick-Slip Forms Triple Rings at Very High Humidity

As demonstrated in Figure 5.5, interesting triple-ring geometry could be fabricated by selecting appropriate experimental conditions. This geometry is only presented at the surfactant concentrations between ~0.001-0.002% while in an environment with a relative humidity of ~90% or higher. A schematic of the triple-ring feature formation is shown in Figure 5.5C. As can be seen, the hydrophobic template and polymer surface would restrict the remaining liquid to form toroid shape surrounding the templates. The coffee stain effect and surface tension would cause the formation of double-ring features as previously discussed. However, as solutes deposit at the outer edge the concentration of surfactant remaining in solution decreases which increases the contact angle of the droplet on the surface. At this point, a stick-slip process would occur, and the boundary would shrink to a smaller concentric edge.[150, 151] The process of solute deposition begins

again at the new edge producing an intermediate ring by the same phenomena that produced the outer ring.

It should be noted that if the surfactant concentration was too high, only smaller gap double rings would be formed. This was consistent with the observed relationship between surfactant concentration and evaporation rate, as discussed in previous section and Figure 5.7. The spontaneous-stick-slip phenomenon would only happen when the whole process was slow down, i.e. less surfactant content and higher humidity conditions. The narrower linewidth (~15nm) of the observed triple rings can be attributed to the lower surfactant content condition because this would reduce the amount of dissolved material available for deposition in the three regions.

This unique stick-slip process was reported in fabricating microscale features in a mechanical way.[150, 151] Herein is the first demonstration of applying this phenomenon to a nano-scale confinement with a ~15 nm linewidth capability via a spontaneous-stick-slip process. This implied the possibility of controlling water stains in patterning sub-30 nm features in a very simple manner, which was difficult to reach by commonly used techniques, e.g. photolithography.

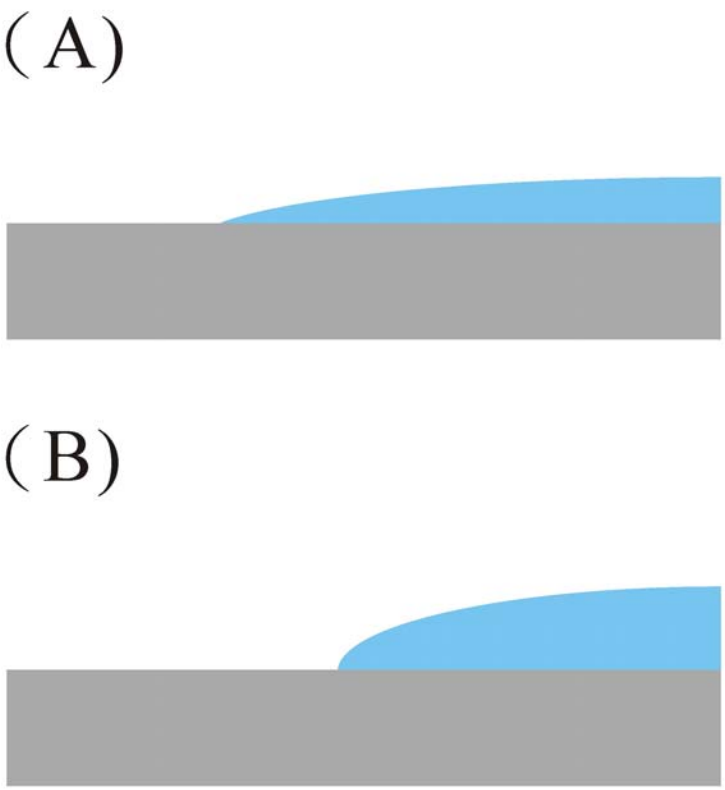

Figure 5.7. Schematic diagrams showing the difference between droplets containing different concentration of surfactants on a hydrophobic surface after a period of drying in a same condition. (A) Higher surfactant concentration droplet. (B) Lower surfactant concentration droplet.

Forming Diverse Geometries

By precisely controlling surfactant content and relative humidity conditions, a variety of features could be prepared by this technique. The effect of these parameters on the features produced was plotted as a feature diagram, Figure 5.8. As can be seen, only small single-ring features would form when the surfactant concentration and relative humidity were maintained at low levels (Region I). When these two factors were moderately adjusted, the feature formation became diverse. As demonstrated, double-ring features were easily observed in the region of higher relative humidity and moderate surfactant content (Region II). Interestingly, a triple-ring sub-region exists when very high humidity was applied and the surfactant content was relatively low (Region III).

Once the surfactant content was high enough, the double rings would merge to form large single rings, which were demonstrated as the double-ring feature region boundary in Figure 5.8. If higher surfactant concentration was applied, a nanohole feature region would dominate at all humidity conditions (Region V). Intermediately, a nanotarget region would exist between the hole and single ring feature regions in the lower humidity area (Region IV).

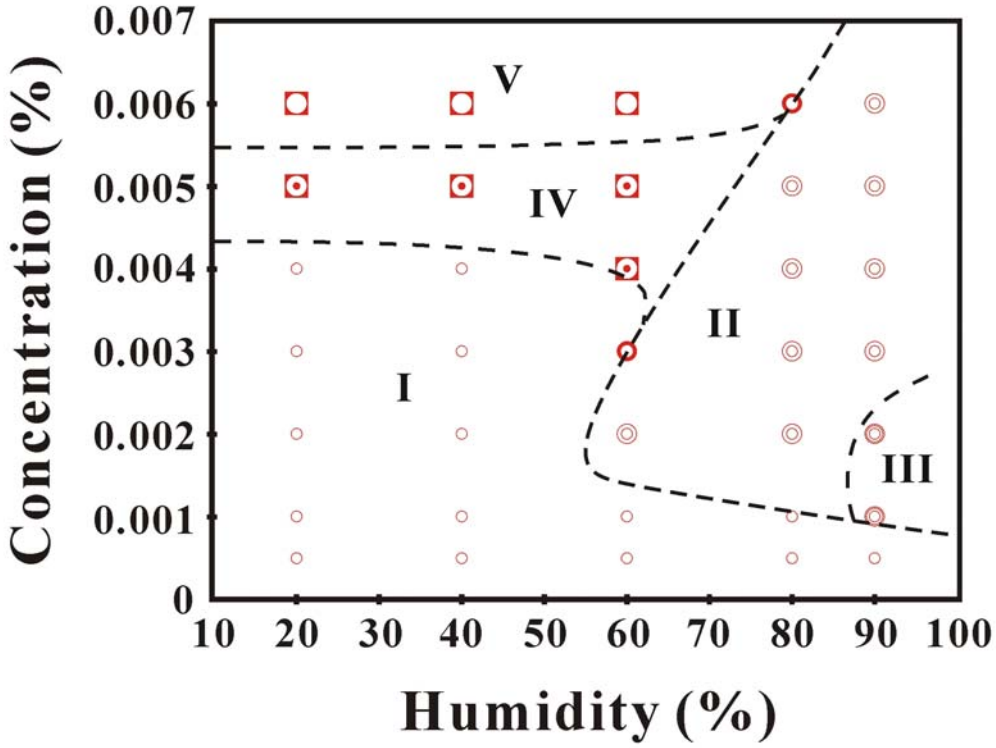

Figure 5.8. Feature diagram of diverse geometries. Region I: Single-ring feature. Region II: Double-ring feature. Region III: Triple-ring feature. Region IV : Nanotarget feature. Region V: Nanohole feature.

Conclusion

In this study, we have discussed the dominating factors in confining water stains in nano-scale water stain lithography. The concentration of surfactant, kinds of surfactant, relative humidity, and physical properties of template materials all determine the corresponding feature formation. By selecting appropriate experimental conditions, feature geometries were fabricated with a line width of ~15 nm without expensive equipment or sophisticated preparation procedures. A real-time observation of the feature formation process was demonstrated for the first time, providing valuable insight into these types of processes. This technique allows for a diversity of nano-scale features to be prepared easily which could be utilized for a diversity of plasmonic devices as well as electronic and biotechnical applications.

CHAPTER VI

EVAPORATIVE TEMPLATING FOR BENCH-TOP NANOHOLE FABRICATION

Introduction

Irreversible evaporation has drawn attention from scientists and engineers because of its potential applications in fabricating useful features for electronics, material science, photonic devices, and biotechnology.[6, 8, 14, 21, 30, 145-148, 165] This non-conventional patterning phenomenon provides an alternative route for fabricating large area uniform features in a much economical and simple way.[149-151, 156, 157] Recently, we have demonstrated an evaporative templating technique which achieved a feature resolution well below 30 nm using this process.[157] The basic concept of the evaporative templating technique is to localize the drying liquid evaporation process and thereby forcing the staining process to happen at specific positions. A variety of nanoscale features with superior resolutions could be easily achieved by this method.[166] Furthermore, nanoscale features comprising diverse materials could also be prepared in a very convenient way through this technique.[167]

Sub-wavelength nano structures have a wide variety of interesting properties and presents useful applications in chemistry, physics, biotechnology, and optics.[77-79, 168-172] One of the exciting observations was the strongly enhanced transmission of light through metallic nanohole array thin films.[173-179] When a thin metal film containing periodic sub-wavelength holes is irradiated by the light, an extraordinary transmission phenomenon

was observed.[173] This is because under proper conditions, the metallic periodic nanostructures can provide the necessary momentum conservation for a coupling process between the incident electromagnetic wave and the surface plasmons on the metal surface. This coupling process therefore converts the light into surface plasmons and gives rise to the transmission peaks observed in a metallic periodic array.[168, 173-178, 180-182] Because the spectral properties of these metallic periodic nanohole arrays could be well tuned through simply adjusting the geometrical parameters, this interesting phenomenon promises a varieties of possible applications in many fields, such as chemical and biological sensing, optoelectronics, optical filters, and useful plasmonic devices.[77-80, 165, 170-172, 174, 183-185]

Periodic nanohole arrays can be fabricated by electron/ion beam lithography, [173, 174, 177, 178, 185-189] soft lithography, [165, 170, 181, 190] and colloidal chemistry methods. [191, 192] These techniques, however, either require expensive equipment, or complicated and time consuming preparation processes. In addition, the prototyping of platforms with varying holes diameter and spacings (periodicity) for the examination of optical properties is cumbersome at best. Although the unique transmission properties of nanohole arrays have been demonstrated to be amenable for plasmonic devices, [165, 170-172, 183-185, 187, 190] a robust and simple fabrication technique regarding tunable spectral range would be highly desirable.

In this study, we demonstrated that a bench-top technique provides a simple route for quickly fabricating such periodic nanohole arrays, under ambient conditions, and without expensive equipment or sophisticated preparation processes. The geometrical

parameters are well-controlled. The optical properties of the fabricated platforms could therefore be rapidly interrogated. It was found that the adsorption wavelength of these structures could be tuned from the visible to the near-infrared region. Furthermore, remarkable sensitivity to the medium's refractive index change was also observed, which produced peak shifts up to hundreds of nanometers. Such properties would be highly desirable in bio-compatible sensing devices.

Experimental Section

The metal film substrates were prepared by evaporation deposition on planar glass slides, VWR Micro Cover Glass No. 2 (West Chester, PA). Each slide was first coated with 3 nm thick Cr and then 50 nm thick metal layers. A 20 nm thick Shipley 1805 polymer layer was then spun-coated onto the metal substrate. A 10.0 μL solution containing suspended monodispersed polystyrene spheres was mixed with a 10.0 μL aqueous solution containing a specific concentration of Triton QS-15 surfactant. (Note: The polystyrene spheres (Duke Scientific, CA) were first pretreated by repeated washing, sonication, and centrifugation in deionized water for 10 times to remove existing surfactant molecules from the suspension solution.) This solution was then gently spread onto the substrate dropwisely and the whole slide was allowed to dry under ambient conditions (Relative humidity ~ 40%) for approximately one hour. The template spheres were then removed via sonication in deionized water and the slide was then dried using N_2.

To fabricate same diameter but different periodicity Au nanohole arrays, Figure 6.2I A-F, slightly different Triton QS-15 surfactant concentrations were applied. For 2504 nm and 1998 nm periodicities, 0.02 % Triton QS-15 concentration (w/w) was applied. For 1745 nm, 1361 nm, 1020 nm, and 799 nm periodicities, 0.025 % Triton QS-15 concentration condition was applied. This would lead to all fabricated polymer features maintaining a 550 nm size in diameter for six different periodicities. Thereafter, the polymer features were transferred to Au through wet chemical etching. An aqueous solution containing 20 mM iron nitrate and 30 mM thiourea was applied in the experiments. A 15 min Au etching duration was applied to successfully transfer the polymer features to Au. In the following step, a 1 min Cr etching process by half diluted commercial etchant (1020 AC, Transene Company Inc., MA) was applied to remove the underneath Cr. Finally, the polymer was removed by copious amount of acetone and deionized water.

To fabricate same periodicity (2μm) but different diameter Au nanohole arrays, Figure 6.2II A-D, a 0.075 % Triton QS-15 surfactant concentration was applied. This led to a polymer feature with 700 nm in diameter. Different Au etching durations were applied to produce different sizes of Au holes through over-etching. 10 min, 16 min, 18 min, and 30 min etching durations were applied to produce 850 nm, 1150 nm, 1300 nm, and 1650 nm sizes Au hole arrays, respectively, with 2μm periodicity.

AFM measurements were made by using a Nanoscope IIIa instrument (Digital Instruments, Santa Barbara, CA). All measurements were made by tapping mode in air with a type J scanner employing etched silicon tips, VistaProbes T190R (Nanoscience Instruments, Phoenix, AZ). UV-Vis-NIR spectra were taken with a Hitachi U-4100 UV-Vis-NIR Spectrophotometer (Hitachi High-Technologies, Tokyo, Japan). The substrates were directly and conveniently seated inside the spectrometer. All experiments were done through normal incidence.

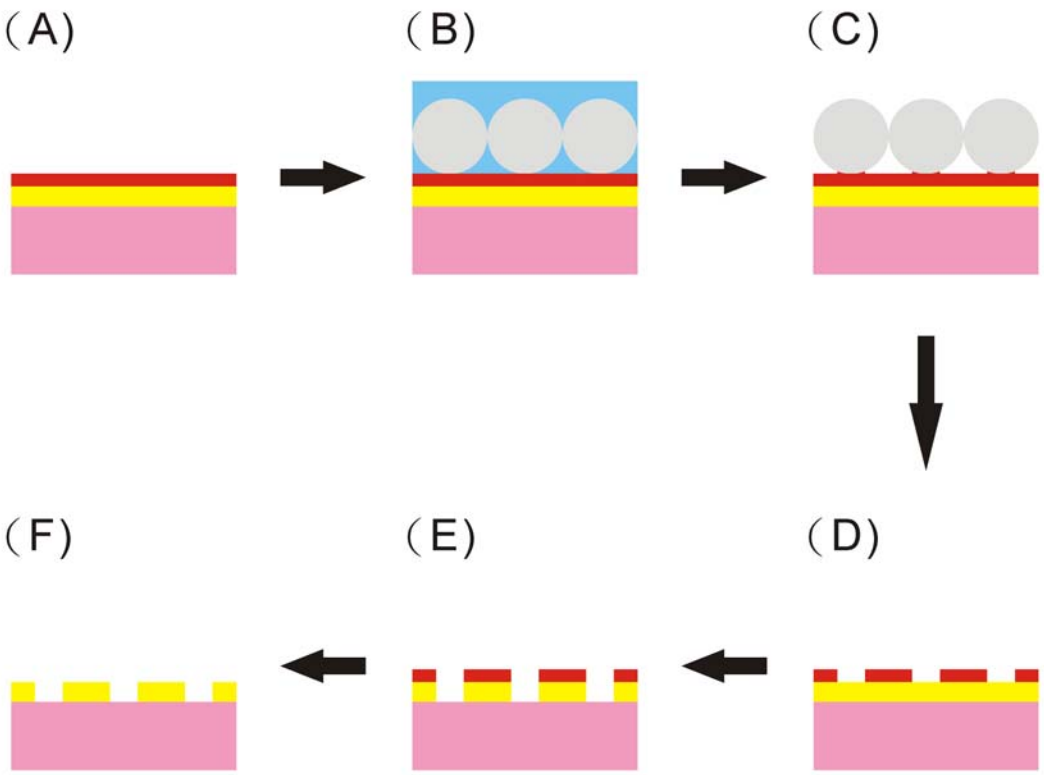

Figure 6.1. Schematic diagram of periodic nanohole features fabrication. (A) A thin layer of polymer is spun-coated on a gold coated glass substrate. (B) Polystyrene spheres are spread on top of the substrate. (C) The liquid is dried under ambient condition. (D) The template spheres are sonicated off in a water bath. Polymer nanohole features are left on top of Au. (E) Polymer features are transferred to Au through wet chemical etching. (F) The top polymer layer is removed by copious of acetone and water.

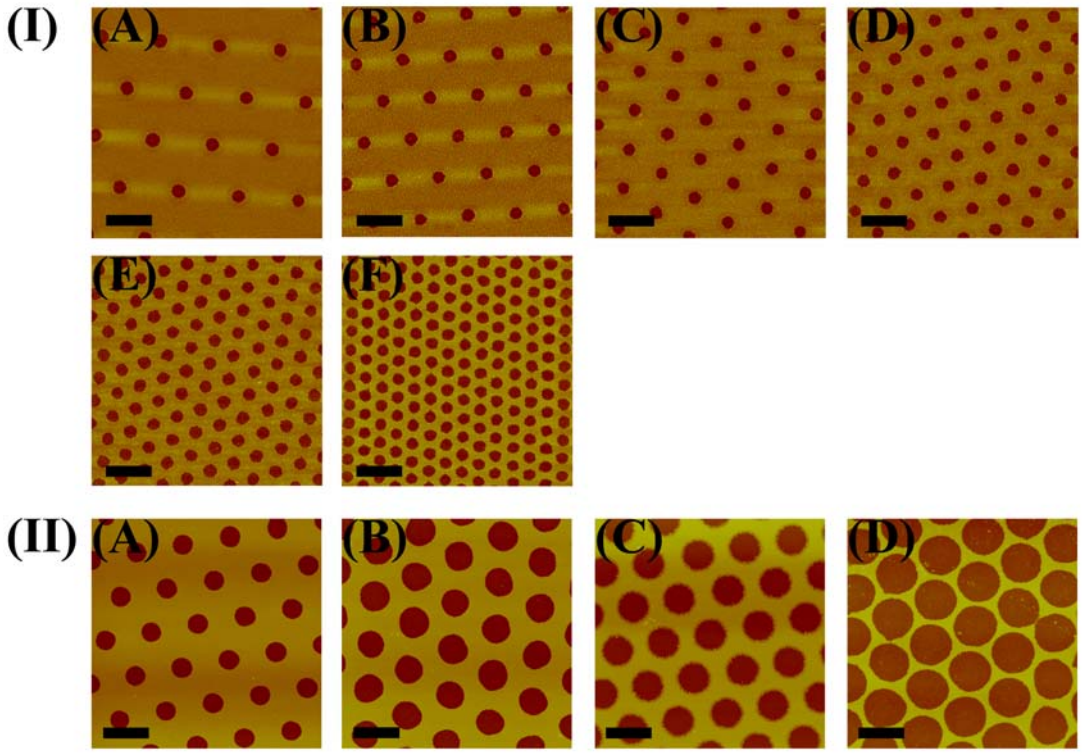

Figure 6.2. (I) 10 μm × 10 μm AFM images showing Au features fabricated with same hole diameter in 550 nm but different periodicities: (A) 2504 nm (B) 1998 nm (C) 1745 nm (D) 1361 nm (E) 1020 nm (F) 799 nm. Images are at the same height scale. Scale bars: 2 μm. (II) 10 μm × 10 μm AFM images showing Au features fabricated with same 2 μm hole periodicity but different sizes in diameter: (A) 850 nm (B) 1150 nm (C) 1300 nm (D) 1650 nm. Images are at the same height scale. Scale bars: 2 μm.

Results

When incident light interacts with a periodic array of sub-wavelength holes, an extraordinary transmission phenomenon [173, 177] arises due to a surface plasmon enhancement effect. In such plasmonic devices, geometric parameters influence the corresponding plasmonic properties. Based on our convenient bench-top technique, system studies of these parameter effects on the optical properties could be easily utilized. Therefore, several important factors were considered in our periodic nanohole array studies. Nanohole periodicity, material, diameter, and surrounding medium effects will be discussed in this section.

Periodic Metal Nanohole Array Preparation

Our strategy for fabricating periodic metal nanohole arrays is shown schematically in Figure 6.1. Planar glass slides were employed in all experiments as substrates. The substrates were first coated via sublimation with a 3 nm thick Cr wetting layer followed by a 50 nm thick metal film (Au, Ag, Cu, or Al). Next, the substrates were spin-coated with a 20 nm thick Shipley 1805 polymer layer. This led to the multilayer structure depicted in Figure 6.1A. A 20.0 μL solution containing the appropriate concentrations of suspended monodispersed polystyrene spheres and Triton QS-15 surfactant was then gently spread onto the substrate dropwisely. The solution was allowed to dry under ambient conditions (Temp = 20 ºC, relative humidity = 40%) for approximately 1 hour, Figure 6.1B-C.

It should be noted that sufficient concentrations of Triton QS-15 surfactant in aqueous solution can dissolve the Shipley polymer layer.[166] The template sphere position was the final place where the remaining surface liquid accumulated during evaporation. [157, 166] This produced a highly concentrated surfactant environment localized at the contact point of the spheres.[166] The polymer spheres and the adjacent polymer material could therefore easily be removed from the substrate in a sonication bath containing an aqueous solution for 1 min at room temperature (Figure 6.1D).[166] In contrast to these disk-shaped locations, other portions of the polymer covered surface maintained their integrity. The templating spheres assumed a hexagonal close packed pattern, which is conserved in the polymer layer. After blowing the sample dry under nitrogen, the patterned slide was then immersed in a metal etching solution to transfer the polymer's features to the underlying metal layer (Figure 6.1E). Finally, the polymer was stripped away by washing with acetone and deionized water. This created a periodic array of nanoholes in the thin metal film as depicted in Figure 6.1F.

With careful adjustment of the working surfactant concentration and metal wet etching time, the metal hole sizes in diameter and the periodicities could be well-tuned to interested ranges, as demonstrated in Figure 6.2. The detailed works will be described in the following sections.

Fabrication of Nanohole Arrays

In a first set of experiments, we fabricated hexagonal arrays of nanoholes in Au with varying periodicity, but fixed pore diameter. To do this, polystyrene spheres of varying diameters were employed. Both the surfactant concentration and metal etching

times were varied to produce nanopores with diameters of 550 ± 20nm. The exact experimental conditions are described in the experimental section. AFM images of substrates with periodicities ranging from 799 nm to 2504 nm are shown in Figure 6.2I A-F.

Next, Au nanohole arrays with constant periodicity, but with varying hole diameters were fabricated. This can be achieved by fixing the polystyrene sphere size, while varying the Au etch time in the last step of the fabrication process: 2 μm polystyrene sphere were employed in a solution containing 0.075 % Triton QS-15. The template fixed the hole array periodicity at 2 μm.[157, 166] Atomic force microscopy images of arrays with hole diameters ranging from 850 nm to 1650 nm are shown in Figure 6.2II A-D. To create this array, Au etch times of 10, 16, 18, and 30 min were used, respectively.

Absorption Spectra

Absorption measurements were made with the nanopore arrays from Figure 6.2 throughout the visible and near infrared regions of the electromagnetic spectrum. The transmission spectra corresponding to the films in Figure 6.2I A-F Au are provided in Figure 6.3A. As can be seen, there were some common signature absorption peaks in the spectra for each film. The overall spectral signatures are similar to each other, except the absorption bands continuously red-shifted as the distance between holes is increased. Moreover, the individual features become significantly broadened with the increasing periodicity. This made the fine structure in the short wavelength region of the spectrum

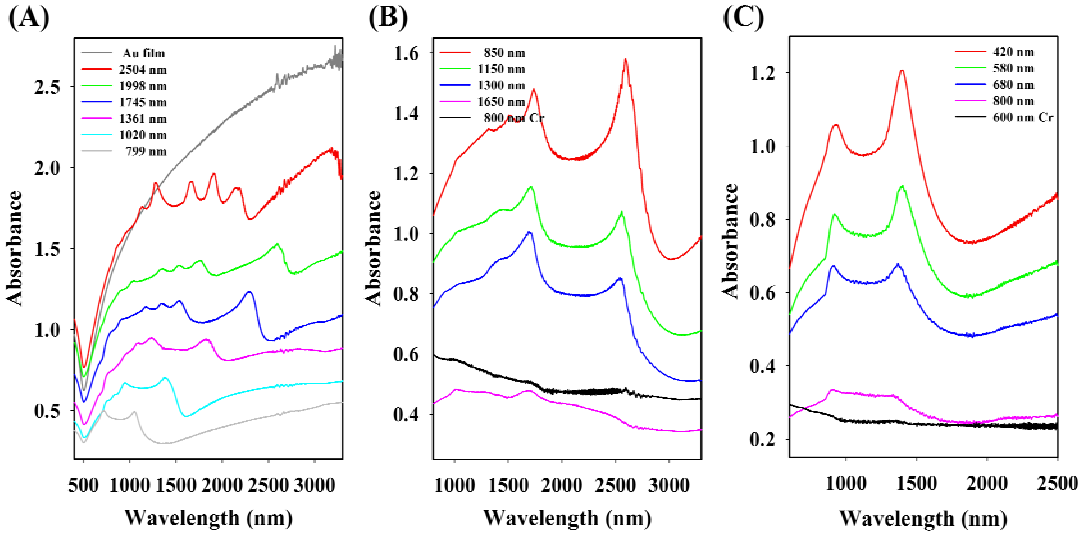

Figure 6.3. UV/VIS-NIR absorption spectrum of Au nanohole films: (A) 550 nm hole arrays with different periodicities, corresponding to Figure 6.2I. (B) 2 μm periodicity arrays with different hole sizes in diameter, corresponding to Figure 6.2II. (C) 1 μm periodicity arrays with different hole sizes in diameter.

easier to discern with increasing periodicity. Nevertheless, multiple more compressed peaks are still present even when the periodicity is 799 nm or 1020 nm.

The absorption features in Figure 6.3A can be attributed to surface plasmon polariton (SPP). [175, 176, 180] The extraordinary transmission spectra have been observed and simulated in periodic metal nanohole arrays.[169, 173-177, 179, 180, 182, 186, 193-195] The incident light should interact with the surface plasmon on either side of the metal film and the array of sub-wavelength holes should be treated as an array of evanescently coupled resonators.[177] Although the individual nanoholes are very small and do not allow propagation of light, the coupling between the introduced electromagnetic wave and the surface plasmons on the surface induced the extraordinary transmission phenomenon.[168] Provided the necessary momentum conservation for this coupling process, the metallic periodic nanostructures can convert the light into surface plasmons and an extraordinary transmission spectrum could be observed.[168] The absorption spectra in our experiments also represent an interesting optical property. Specific signature absorption peaks were clearly observed and the spectra were one of the most systematic results ever demonstrated. It is also interesting to note that the signature features in the spectra are highly correlated to the periodicity. Moreover, the relationship between the frequency of the signature peaks and the lattice periodicity is almost perfectly linear, as shown in Figure 6.4A.

Next, the absorption spectra from systems with constant periodicity, but varying hole size from Figure 6.2II A-D are shown in Figure 6.3B. It should be noted that hole size is often considered to be an important factor affecting surface plasmon modes.[77, 194,

As expected, absorption increases as the holes are made smaller; however, the peak shapes and positions remain nearly unchanged. Specifically, the two longer wavelength features blue shift only 25 nm to 30 nm as the hole size is increased from 850 nm to 1650 nm. It should also be noted that the smallest peaks in the shorter wavelength region were also shifted by changing hole diameters but were difficult to be distinguished in the spectra. Nevertheless, these small shifts were very tiny, Figure 6.4B, compared to the 1000+ nm shifts that can be obtained by changing periodicity rather than hole diameter. As an additional confirmation of this, we wished to repeat this experiment at a periodicity of 1 μm. The idea was to see if more closely spaced holes would lead to larger changes as the pore size is modulated. Experiments were run with hole diameters ranging from 420 nm to 800 nm. Again, only a slight blue shift in the two major features was observed as a function of pore size (Figure 6.3C). This result is a clear indication that periodicity rather than pore diameter is the key variable for modulating the adsorption frequency.

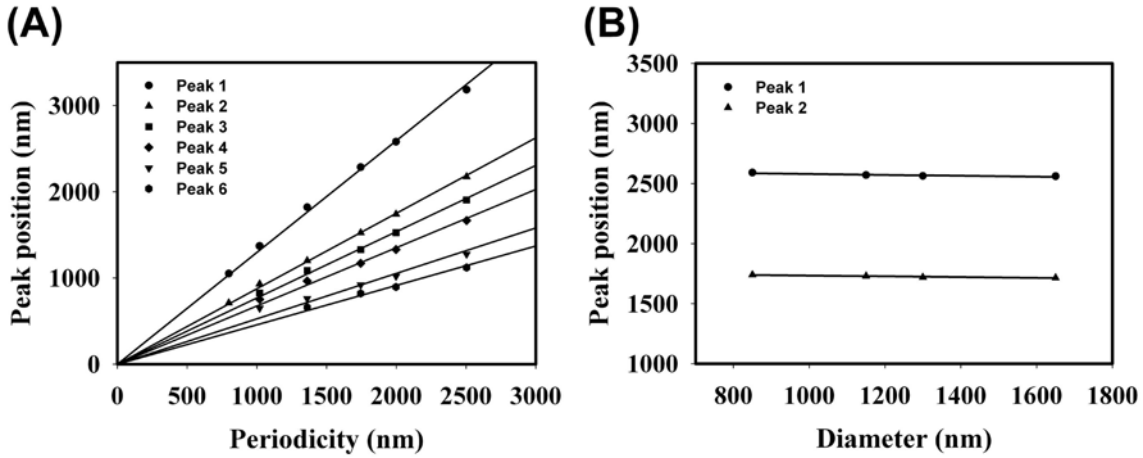

Figure 6.4. The relationship between (A) periodicities and their representing peak positions when hole size is fixed. (B) sizes and their representing peak positions when hole periodicity is fixed.

Tuning the Index of Refraction of the Surrounding Medium

In a next set of experiments, a series of different liquids were placed into contact with the nanohole array to investigate the effect of changes in index of refraction in the surrounding medium on the positions of the adsorption bands. Experiments were performed with a simple sandwich setup as shown in Figure 6.5A. Specifically, an organic or aqueous solution was introduced onto the substrate surface and another clean glass slide was placed on top of it. A transmission UV-Vis-NIR spectrum was then obtained by shedding the source light through the top glass slide. In all experiments, the pattern contained a 50 nm thick Au film with 750 nm diameter holes and a 2 μm periodicity. Seven liquids with different refractive indexes were employed with indices of refraction ranging from 1.33 to 1.5. The spectra obtained are shown in Figure 6.5B. A large wavelength shift (compared to the air) was observed in each case. For clarity, the corresponding peaks wavelength shifts were outlined in Table 6.1.

Significantly, only a part of signature features were greatly affected relative to the others. The second and the fifth absorption bands counting from the higher wavelength side shifted the most. It is believed that the shifting of these peaks is a plasmonic phenomenon, which is very sensitive to the refractive index of the surrounding medium. On the other hand, the first, the third, and the fourth hands were virtually unaffected. Figure 6.6 plots the peak shifts of the signature features as a function of the index of refraction and the corresponding numerical data is outline in Table 6.1. It is clear to see the peak wavelength shifts depends on the refractive index of the medium introduced. The higher the index, the more peak red shifts were observed

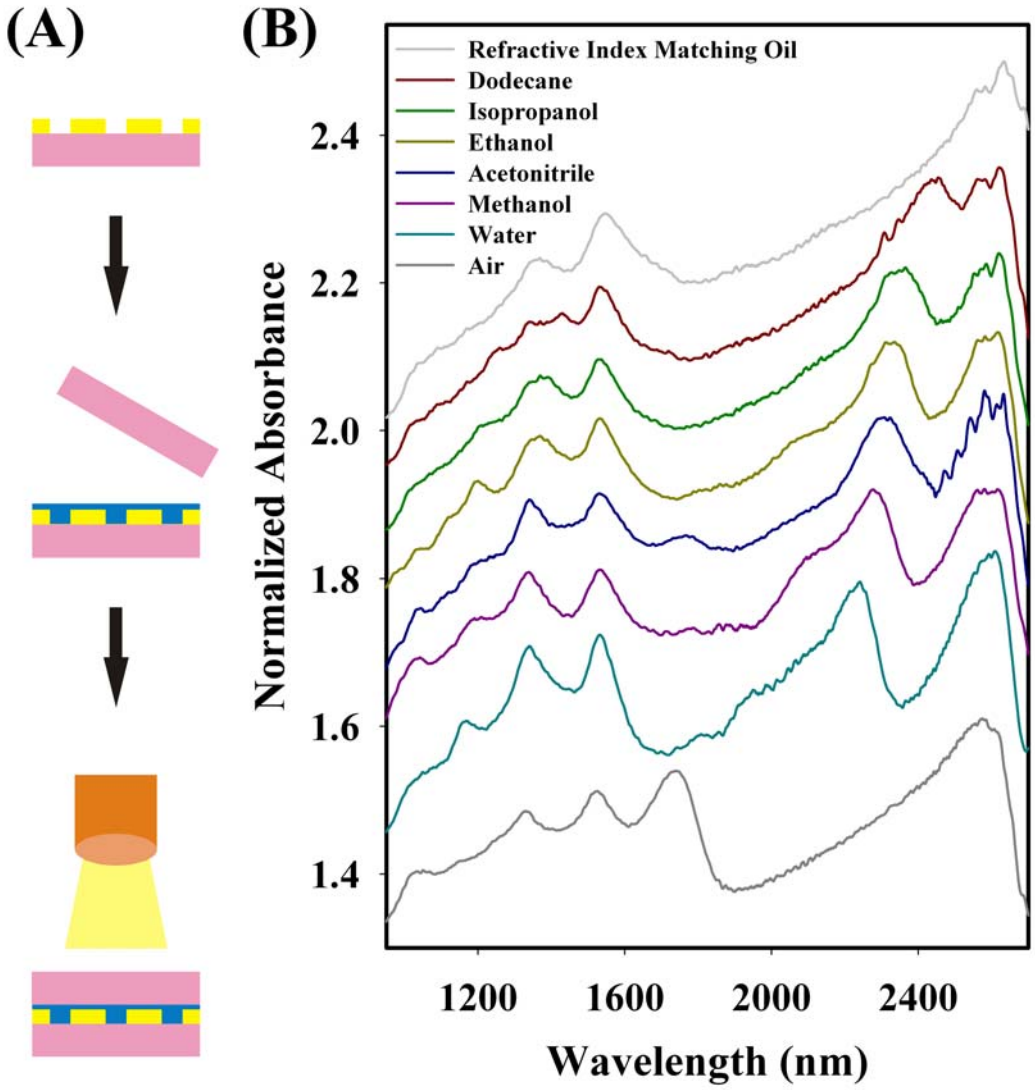

Figure 6.5. (A) Schematic diagram of the periodic Au nanohole array device in medium effect examination. (B) Normalized NIR absorption spectrum of a Au film with 750 nm holes in diameter and 2 μm in periodicity when treated with different refractive index medium.

Table 6.1. The refractive index of surrounding medium and the corresponding peak wavelength shifts (compare to air).

	Air	H_2O	Methanol	Acetonitrile	Ethanol	Isopropanol	Dodecane	Refractive Index Matching Oil
Refractive index	1	1.333	1.3288	1.3442	1.3611	1.3776	1.422	1.5
Peak 1 Shift (nm)	0	20	30	32	35	35	40	50
Peak 2 Shift (nm)	0	500	540	565	590	625	710	890
Peak 3 Shift (nm)	0	4	5	5	6	9	11	15
Peak 4 Shift (nm)	0	6	8	8	9	10	10	14
Peak 5 Shift (nm)	0	310	318	326	356	370	410	520

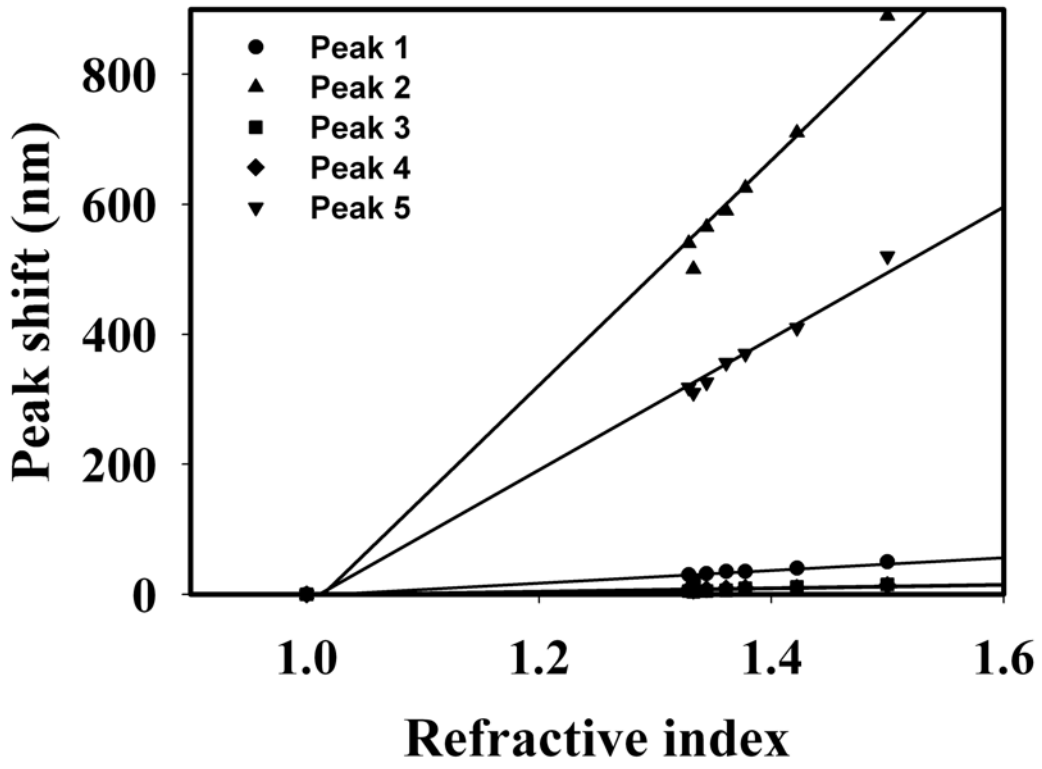

Figure 6.6. The relationship between signature feature peak shifts and the surrounding medium refractive index.

based on a nearly linear trend. However, the very different extends of peak shifting resulted in a dramatic trend line slope difference as can be seen in Figure 6.6. It is very interesting to note that this slope varying trend does not follow the signature absorption bands sequence in the spectra.

These novel active-inactive peak sets provides a possible route for fabricating highly sensitive plasmonic devices based with a built-in reference. It is also important to note that the active peak shift is fully reversible, allowing for the production of a reusable device for sensing applications. The details for the different bands based upon these observations will be elaborated in the discussion section.

Changing the Metal

Using our technique, the uniform nanohole polymer features could be easily transferred to any interest materials. Plasmonic architectures are known to be highly dependent on the specific metal from which they are made. Indeed, different metals give rise to different plasmonic bands with specific characteristic peak positions. To probe this relationship, we examined three additional different metal films: Ag, Cu, and Al. Similar sample preparation processes were applied to produce each metal film as was done for Au. All metal films were 50 nm thick with a hole periodicity of 2 μm. As can be seen in Figure 6.7, the features are generally the same as those found for Au. Specifically two prominent features are observed and a number of smaller features are found on the high energy side of the shorter wavelength peak.

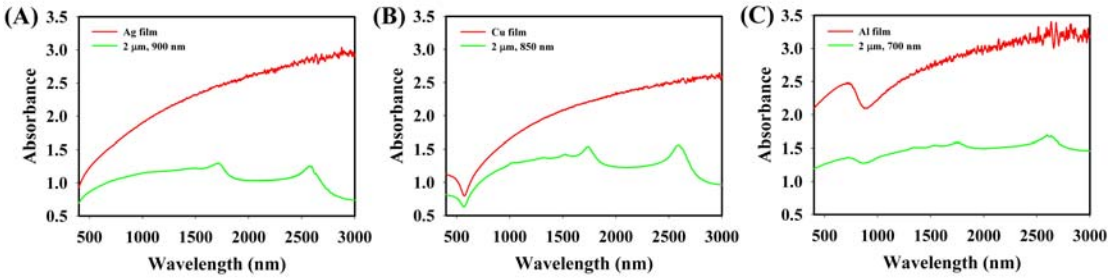

Figure 6.7. The UV-NIR absorption spectrum showing signature peaks of periodic nanohole array within different materials: (A) Ag (B) Cu (C) Al. The corresponding periodicities and hole sizes are demonstrated in the insets.

Discussion

Through our evaporative templating technique, a nanohole array with easily tunable parameters could be easily fabricated in a very simple and economical way. The whole preparation process requires only around one hour and produce highly uniform nanohole polymer features. These polymer structures can therefore be used as a mold to be transferred to different materials. This is one of the most convenient methods ever reported in being able to produce such high quality and large area useful metallic nanohole array films in a very short time. This technique therefore guarantees high productivity of these kinds of devices for fast property testing in a very economical way.

In our experiment, the optical spectrum is far more sensitive to periodicity than pore diameter, Figure 6.3. Changing the pore diameter, of course, should cause a perturbation in the effective index of refraction of the medium, which ultimately leads to a modest shift in the absorption peaks. On the other hand, the coupling between the plasmonic bands is altered as the distance between the pores is altered. In the present experiments, the incident light is perpendicular to the substrate surface which does not allow for in-plane momentum transfer to the surface plasmon resonances. Instead, the SPR frequency is solely dependent on the grating periodicity, which makes the adsorption frequencies particularly sensitive to the separation distance between the features as has been demonstrated both theoretically and experimentally.[176, 197]

The spectral features observed here were induced by surface plasmon enhancement phenomena. Au, Ag, Cu, and Al are typical plasmonic metals,[165, 198] and they all give rise to the same basic spectroscopic signature. However, Cr, which does not

give rise to this signature, is only marginally metallic and does not support surface plasmon modes.[176, 199] It should be noted that the signature peaks of different metal films did not represent remarkable dissimilarity as other plasmonic geometries could induce, Figure 6.7.[165, 198] This implies that the absorption peak structure was dominated by periodicity rather than the individual plasmonic properties of the metals. Nevertheless, only plasmonic metals represented this phenomenon in the experiment.

In the spectra of our experiment, many distinct absorption peaks were observed as demonstrated in Figure 6.3A. We categorized these signature peaks into two sets. The first, the third, and the fourth peaks counting from the higher wavelength side composed the first set. The second, the fifth, and the sixth peaks were the second set. It was believed the two sets of peaks come from surface plasmons on both sides of the Au film. In our experiment, the periodic nanohole array Au film was supported by a glass substrate. The top (air) and bottom (glass) sides of the Au film should support different surface plasmon modes. Consequently, the existence of two sets of plasmonic peaks is expected.[168, 180, 189] We assigned the first set of peaks to be the bottom (glass) side surface plasmon, while the second set was contributed by the top (air) side instead. This assignment is also supported by our surrounding medium refractive index changing experiment discussed as follows.

For plasmonic devices, the surrounding medium of the nanostructures causes dramatic property alteration. This is believed to be induced by surface plasmon changes due to different refractive index and dielectric constant of each medium.[165, 177, 179, 180, 200] In our results, Figure 6.5 and 6.6, a magnificent peak shifting was observed on peak 2

and 5 with hundreds of nm wavelength shifts. On the other hand, a comparably stable phenomenon was observed on peak 1, 3, and 4. As pointed out before, we assigned the peak 2 and 5 to be contributed by the top (air) side surface plasmons. Therefore, this set of peaks should be very sensitive to the changing of surrounding medium refractive index. On the other hand, the peak 1, 3, and 4 were assigned to the bottom (glass) side surface plasmon contributions and should not have much response to the top layer medium changes. The tiny shifts observed were believed induced by local environment change through filling the holes with different liquids. Furthermore, it is also important to note that when the refractive index matching oil was introduced to the system, only peak 1, 3, and 4 would exist in the spectrum since the plasmonic modes on both sides are now the same.

When a momentum matching condition happens on a periodic nanohole array, the incident light could be coupled to surface plasmons. If the light is a normal incidence and the periodic array maintains a hexagonal rigidity, the transmission peak positions could be expressed by:[168, 175, 177-180, 189, 201]

$$\lambda_{\max} = \frac{P}{\sqrt{\frac{4}{3}(i^2 + ij + j^2)}} \sqrt{\frac{\varepsilon_m \varepsilon_d}{\varepsilon_m + \varepsilon_d}}$$

where P is the periodicity of the array, i and j are the grating orders of the array, and ε_m and ε_d are the dielectric constants of the metal and the dielectric material in contact with the metal, respectively. Using this equation, we successfully assigned our two sets of absorption peaks as follows. In the air environment, peak 1, 3, and 4 are contributed by $(1,0)_{glass}$, $(1,1)_{glass}$, and $(2,0)_{glass}$; while peak 2, 5, and 6 are corresponding to $(1,0)_{air}$,

$(1,1)_{air}$, and $(2,0)_{air}$, respectively. This assignment is also supported by our surrounding medium refractive index changing results. When higher refractive index medium was introduced, the original air side plasmon mode was changed. A red shift of these peaks was expected and observed in the spectrum, Figure 6.5. At the mean time, the local environment of the glass substrate side was only slightly affected and a much less red shift of those corresponding peaks was expected. It is interesting to note that when the refractive index matching oil was introduced to the system, only one set of peaks would exist. Specifically, peak 2 is merged to peak 1; peak 5 is merged to peak 3; and peak 6 is merged to peak 4, respectively. It is also important to note that if the Au film is very thin, the simulation results through the above equation would be slight different from the observations. This is because the local environment of the top and bottom sides of the Au film would slightly affect each other and a prediction through bulk dielectric constants would have some alteration.

In summary, periodic metallic nanohole arrays can provide interesting optical properties. These phenomenons were believed to be dominated by the surface plasmon. In our films, unique plasmonic properties were also clearly observed. In addition, much richer signature features were obtained and could be clearly outlined. This is because the arrays produced through our technique maintained a very high quality in a large area, and the parameters could be easily well-tuned to a very wide range. Systematic studies are therefore much simpler and more economical. This technique consequently provides scientist and engineers a convenient way to prototype similar structures for their own requirements and to manipulate the relative property testing.

Conclusion

A robust technique is demonstrated in this study to produce periodic metal nanohole arrays under ambient conditions without sophisticated preparation or expensive equipment. Uniform nanohole arrays with different periodicities, sizes, and materials could be easily performed than any other comparable methods demonstrated before to fabricate similar features. The unique signature spectrum was found to be very sensitive to the environmental refractive index change, with peak shifts in the hundreds of nanometers. A novel active-inactive peak set was also observed and assigned in the spectrum. This active window could be well-tuned to any region between Vis to Near-IR range. Periodicity was found to be the dominating factor in the spectral signatures in comparison to hole diameter or material. This phenomenon was only observed in plasmonic materials, which suggested the important role of the surface plasmon in this system. A highly sensitive bio-compatible device is therefore possible based on this platform and could be widely applied to analytical, biomedical, industrial, agricultural, and clinical technologies.

CHAPTER VII

SUMMARY AND OUTLOOK

During my student life at Texas A&M University, my research was focused on rapid prototyping and bench-top techniques for nanofabrication. Modifications in nanostructures can be made quickly and efficiently to broadly test new physical properties and related applications in the chemical and biological sciences. In addition, the results provide a better understanding of material properties on the nanoscale which is also an interesting and intriguing scientific topic. Overall, my research is best viewed as a fundamental molecular-level understanding of surface patterning with chemistry, engineering, physics, and biotechnology. Herein, I am summarizing the research work I achieved and my current projects. In addition, I will also discuss some potential future directions of these techniques.

First of all, we demonstrate a simple, inexpensive, and rapid method for making metal nanoparticles ranging between 10 nm and 100 nm in size. The process can be competed in approximately 11 minutes without the use of a clean room environment or vacuum techniques. The method works by using a thin supported TiO_2 film as a photocatalyst and an alumina membrane as a template. The nanoparticle array formed in this manner is nearly monodispersed and the particle surface density and geometry are uniform over large areas. Depending on this bench-top technique, we successfully

demonstrate a simple label-free biosensor fabrication method based on transmission localized surface plasmon resonance (T-LSPR). The metal surface could be elaborated with thiol-linked ligands for binding protein molecules. For demonstration purposes, biotin-linked thiol ligands were employed for binding streptavidin from solution. For an array of 19 nm silver nanoparticles, a red shift in the T-LSPR of 24 nm was observed upon protein-ligand binding at saturation. Platforms were also fabricated with silver nanoparticles of different sizes, up to 73 nm in diameter. The maximum LSPR wavelength shift was found to be nanoparticle size dependent and the maximum sensitivity was found for the smallest nanoparticles.

Secondly, we demonstrate a nanoscale patterning technique for creating twin features in polymers and metals. The process works by combining evaporative ring staining with a colloidal templating process. Well-ordered hexagonally arrayed double rings were fabricated using hydrophobic spherical templates. The diameter of the rings, the width of individual rings, and the spacing between concentric and adjacent rings could be tuned by varying the solution conditions. Arrays could also be made without the outer ring by employing hydrophilic templates. Systematic studies of the evaporative templating to create the nanoscale geometric features on planar substrates were also demonstrated. The effects of solution conditions, colloidal sphere chemistry, size, and the relative humidity of the surroundings were discussed for creating a unique array of nanoscale architectures. For example, well-ordered hexagonally arrayed nanorings, double rings, triple rings, targets, and holes were all easily prepared. A line width as thin as ~15 nm can repeatably be performed with this technology. In addition, real-time

formation of the features can also be achieved which provides important insights into the physical-chemical mechanism of their formation.

Finally, fabrication of an ultra-sensitive plasmonic optical device is demonstrated. This technique provides an easy way to produce periodic hexagonal nanohole metal films quickly under ambient conditions without any expensive equipment or sophisticated preparation. It was observed that the absorption wavelength of the peaks produced by these structures could be shifted by hundreds of nanometers depending on the refractive index of the surrounding medium. Two sets of major signature absorption peaks were found; one of them was highly sensitive to changes in the surrounding medium, the other one was not. The peaks were assigned to the two surface plasmon modes contributed by the two metal surfaces. This sensitive spectral range can be well-tuned in the visible and near infrared region.

In summary, my research combines surface chemistry, physics, engineering, analytical chemistry, and biotechnology. These rapid prototyping bench-top techniques provide a much convenient and economical route to fabricate well defined nanostructures. We have shown that these processes can be precisely controlled and applied for many useful purposes. The results provide a better understanding of material properties on the nanoscale level. In addition, the nanostructures can be modified quickly and efficiently for testing a broad range of new physical properties and their related applications in the chemical and biological fields. In the future, these techniques could be easily combined with other techniques for advanced applications. Novel interesting nanostructures are therefore much easier to obtain. Fascinating properties and

their potential applications in plasmonics, biosensing, optoelectronics, and surface chemistry studies will no more be restricted to the sophisticated preparations and the expensive equipments.

REFERENCES

1. Chan, W. C. W.; Nie, S. M. *Science,* **1998,** *281*, 2016.

2. Elghanian, R.; Storhoff, J. J.; Mucic, R. C.; Letsinger, R. L.; Mirkin, C. A. *Science,* **1997,** *277*, 1078.

3. Haes, A. J.; Van Duyne, R. P. *Journal of the American Chemical Society,* **2002,** *124*, 10596.

4. Haes, A. J.; Zou, S. L.; Schatz, G. C.; Van Duyne, R. P. *J. Phys. Chem. B,* **2004,** *108*, 6961.

5. Han, M. Y.; Gao, X. H.; Su, J. Z.; Nie, S. *Nature Biotechnology,* **2001,** *19*, 631.

6. Jacobs, H. O.; Whitesides, G. M. *Science,* **2001,** *291*, 1763.

7. Joannopoulos, J. D.; Meade, R. D.; Winn, J. N., *Photonic Crystals: Modeling the Flow of Light*. Princeton University Press: Princeton, NJ, 1995.

8. Joannopoulos, J. D.; Villeneuve, P. R.; Fan, S. H. *Nature,* **1997,** *386*, 143.

9. Kohli, P.; Harrell, C. C.; Cao, Z. H.; Gasparac, R.; Tan, W. H.; Martin, C. R. *Science,* **2004,** *305*, 984.

10. Lee, K. B.; Park, S. J.; Mirkin, C. A.; Smith, J. C.; Mrksich, M. *Science,* **2002,** *295*, 1702.

11. Murphy, C. J. *Anal. Chem.,* **2002,** *74*, 520A.

12. Ostuni, E.; Chen, C. S.; Ingber, D. E.; Whitesides, G. M. *Langmuir,* **2001,** *17*, 2828.

13. Rosi, N. L.; Mirkin, C. A. *Chem. Rev.,* **2005,** *105*, 1547.

14. Thurn-Albrecht, T.; Schotter, J.; Kastle, C. A.; Emley, N.; Shibauchi, T.; Krusin-Elbaum, L.; Guarini, K.; Black, C. T.; Tuominen, M. T.; Russell, T. P. *Science,* **2000,** *290*, 2126.

15. Xia, Y. N.; Yang, P. D.; Sun, Y. G.; Wu, Y. Y.; Mayers, B.; Gates, B.; Yin, Y. D.; Kim, F.; Yan, Y. Q. *Advanced Materials,* **2003,** *15*, 353.

16. Brust, M.; Kiely, C. J. *Colloid Surf. A-Physicochem. Eng. Asp.,* **2002,** *202*, 175.

17. Daniel, M. C.; Astruc, D. *Chem. Rev.,* **2004,** *104*, 293.

18. Evanoff, D. D.; Chumanov, G. *J. Phys. Chem. B,* **2004,** *108*, 13948.

19. Haynes, C. L.; McFarland, A. D.; Smith, M. T.; Hulteen, J. C.; Van Duyne, R. P. *J. Phys. Chem. B,* **2002,** *106*, 1898.

20. Henglein, A. *Langmuir,* **1999,** *15*, 6738.

21. Ito, T.; Okazaki, S. *Nature,* **2000,** *406*, 1027.

22. Jana, N. R.; Gearheart, L.; Murphy, C. J. *Langmuir,* **2001,** *17*, 6782.

23. Kumbhar, A. S.; Kinnan, M. K.; Chumanov, G. *Journal of The American Chemical Society,* **2005,** *127*, 12444.

24. Mendes, P. M.; Jacke, S.; Critchley, K.; Plaza, J.; Chen, Y.; Nikitin, K.; Palmer, R. E.; Preece, J. A.; Evans, S. D.; Fitzmaurice, D. *Langmuir,* **2004,** *20*, 3766.

25. Peng, X. G.; Wickham, J.; Alivisatos, A. P. *Journal of The American Chemical Society,* **1998,** *120*, 5343.

26. Scott, R. W. J.; Wilson, O. M.; Crooks, R. M. *J. Phys. Chem. B,* **2005,** *109*, 692.

27. Tan, B. J. Y.; Sow, C. H.; Koh, T. S.; Chin, K. C.; Wee, A. T. S.; Ong, C. K. *J. Phys. Chem. B,* **2005,** *109*, 11100.

28. Wang, X. D.; Lao, C. S.; Graugnard, E.; Summers, C. J.; Wang, Z. L. *Nano Letters,* **2005,** *5*, 1784.

29. Moreau, W. M., *Semiconductor Lithography*. Plenum, New York, 1989; Chapter 8.

30. Gates, B. D.; Xu, Q. B.; Stewart, M.; Ryan, D.; Willson, C. G.; Whitesides, G. M. *Chem. Rev.,* **2005,** *105*, 1171.

31. Sze, S. M., *VLSI Technology*. McGraw-Hill: Singapore, 1988; p Chapter 4.3.

32. Sherry, L. J.; Chang, S. H.; Schatz, G. C.; Van Duyne, R. P.; Wiley, B. J.; Xia, Y. N. *Nano Letters,* **2005,** *5*, 2034.

33. Nehl, C. L.; Liao, H. W.; Hafner, J. H. *Nano Letters,* **2006,** *6*, 683.

34. Wiley, B.; Sun, Y. G.; Mayers, B.; Xia, Y. N. *Chem.-Eur. J.,* **2005,** *11*, 454.

35. Sun, Y. G.; Xia, Y. N. *Science,* **2002,** *298*, 2176.

36. Wiley, B.; Sun, Y. G.; Xia, Y. N. *Langmuir,* **2005,** *21*, 8077.

37. Im, S. H.; Lee, Y. T.; Wiley, B.; Xia, Y. N. *Angew. Chem.-Int. Edit.,* **2005,** *44*, 2154.

38. Bijkerk, F.; Shmaenok, L. A.; Louis, E.; Voorma, H. J.; Koster, N. B.; Bruineman, C.; Bastiaensen, R.; vanderDrift, E.; Romijn, J.; deGroot, L. E. M.; Rousseeuw, B. A. C.; Zijlstra, T.; Platonov, Y. Y.; Salashchenko, N. N. *Microelectron. Eng.,* **1996,** *30*, 183.

39. Yang, D.; Chang, S. W.; Ober, C. K. *J. Mater. Chem.,* **2006,** *16*, 1693.

40. Liu, Z. W.; Wei, Q. H.; Zhang, X. *Nano Letters,* **2005,** *5*, 957.

41. Solak, H. H.; David, C.; Gobrecht, J.; Golovkina, V.; Cerrina, F.; Kim, S. O.; Nealey, P. F. *Microelectron. Eng.,* **2003,** *67-8*, 56.

42. Boto, A. N.; Kok, P.; Abrams, D. S.; Braunstein, S. L.; Williams, C. P.; Dowling, J. P. *Physical Review Letters,* **2000,** *85*, 2733.

43. Li, H. W.; Muir, B. V. O.; Fichet, G.; Huck, W. T. S. *Langmuir,* **2003,** *19*, 1963.

44. Piner, R. D.; Zhu, J.; Xu, F.; Hong, S. H.; Mirkin, C. A. *Science,* **1999,** *283*, 661.

45. Hobbs, K. L.; Larson, P. R.; Lian, G. D.; Keay, J. C.; Johnson, M. B. *Nano Letters,* **2004,** *4*, 167.

46. Hulteen, J. C.; Treichel, D. A.; Smith, M. T.; Duval, M. L.; Jensen, T. R.; Van Duyne, R. P. *J. Phys. Chem. B,* **1999,** *103*, 3854.

47. Hulteen, J. C.; Vanduyne, R. P. *J. Vac. Sci. Technol. A-Vac. Surf. Films,* **1995,** *13*, 1553.

48. Kosiorek, A.; Kandulski, W.; Glaczynska, H.; Giersig, M. *Small,* **2005,** *1*, 439.

49. McLellan, J. M.; Geissler, M.; Xia, Y. N. *Journal of The American Chemical Society,* **2004,** *126*, 10830.

50. Nicewarner-Pena, S. R.; Freeman, R. G.; Reiss, B. D.; He, L.; Pena, D. J.; Walton, I. D.; Cromer, R.; Keating, C. D.; Natan, M. J. *Science,* **2001,** *294*, 137.

51. Pearson, D. H.; Tonucci, R. J.; Bussmann, K. M.; Bolden, E. A. *Advanced Materials,* **1999,** *11*, 769.

52. Xu, H.; Goedel, W. A. *Angew. Chem.-Int. Edit.,* **2003,** *42*, 4696.

53. Yan, F.; Goedel, W. A. *Nano Letters,* **2004,** *4*, 1193.

54. Zhu, F. Q.; Fan, D. L.; Zhu, X. C.; Zhu, J. G.; Cammarata, R. C.; Chien, C. L. *Advanced Materials,* **2004,** *16*, 2155.

55. Ji, R.; Lee, W.; Scholz, R.; Gosele, U.; Nielsch, K. *Advanced Materials,* **2006,** *18*, 2593.

56. Wang, Z. K.; Lim, H. S.; Liu, H. Y.; Ng, S. C.; Kuok, M. H.; Tay, L. L.; Lockwood, D. J.; Cottam, M. G.; Hobbs, K. L.; Larson, P. R.; Keay, J. C.; Lian, G. D.; Johnson, M. B. *Physical Review Letters,* **2005,** *94*.

57. Martin, C. R. *Science,* **1994,** *266*, 1961.

58. Goh, C.; Coakley, K. M.; McGehee, M. D. *Nano Letters,* **2005,** *5*, 1545.

59. Sander, M. S.; Gao, H. *Journal of The American Chemical Society,* **2005,** *127*, 12158.

60. Goldberger, J.; He, R. R.; Zhang, Y. F.; Lee, S. W.; Yan, H. Q.; Choi, H. J.; Yang, P. D. *Nature,* **2003,** *422*, 599.

61. Hou, S. F.; Harrell, C. C.; Trofin, L.; Kohli, P.; Martin, C. R. *Journal of The American Chemical Society,* **2004,** *126*, 5674.

62. Jirage, K. B.; Hulteen, J. C.; Martin, C. R. *Science,* **1997,** *278*, 655.

63. Kovtyukhova, N. I.; Mallouk, T. E.; Mayer, T. S. *Advanced Materials,* **2003,** *15*, 780.

64. Liang, Z. J.; Susha, A. S.; Yu, A. M.; Caruso, F. *Advanced Materials,* **2003,** *15*, 1849.

65. Sander, M. S.; Cote, M. J.; Gu, W.; Kile, B. M.; Tripp, C. P. *Advanced Materials,* **2004,** *16*, 2052.

66. Shin, H. J.; Jeong, D. K.; Lee, J. G.; Sung, M. M.; Kim, J. Y. *Advanced Materials,* **2004,** *16*, 1197.

67. Steinhart, M.; Jia, Z. H.; Schaper, A. K.; Wehrspohn, R. B.; Gosele, U.; Wendorff, J. H. *Advanced Materials,* **2003,** *15*, 706.

68. Steinhart, M.; Wehrspohn, R. B.; Gosele, U.; Wendorff, J. H. *Angew. Chem.-Int. Edit.,* **2004,** *43*, 1334.

69. Krishnamoorthy, K.; Zoski, C. G. *Anal. Chem.,* **2005,** *77*, 5068.

70. Jung, K. H.; Yoon, J. W.; Koshizaki, N.; Kwon, Y. S. *Jpn. J. Appl. Phys. Part 1 - Regul. Pap. Brief Commun. Rev. Pap.,* **2005,** *44*, 5300.

71. Liang, J. Y.; Chik, H.; Yin, A. J.; Xu, J. *J. Appl. Phys.,* **2002,** *91*, 2544.

72. Willets, K. A.; Van Duyne, R. P. *Annu. Rev. Phys. Chem.,* **2007,** *58*, 267.

73. Haes, A. J.; Haynes, C. L.; McFarland, A. D.; Schatz, G. C.; Van Duyne, R. R.; Zou, S. L. *MRS Bull.,* **2005,** *30*, 368.

74. Zhang, X. Y.; Young, M. A.; Lyandres, O.; Van Duyne, R. P. *Journal of The American Chemical Society,* **2005,** *127*, 4484.

75. Aizpurua, J.; Hanarp, P.; Sutherland, D. S.; Kall, M.; Bryant, G. W.; de Abajo, F. J. G. *Physical Review Letters,* **2003,** *90*.

76. Larsson, E. M.; Alegret, J.; Kall, M.; Sutherland, D. S. *Nano Letters,* **2007,** *7*, 1256.

77. Prikulis, J.; Hanarp, P.; Olofsson, L.; Sutherland, D.; Kall, M. *Nano Lett.,* **2004,** *4*, 1003.

78. Rindzevicius, T.; Alaverdyan, Y.; Dahlin, A.; Hook, F.; Sutherland, D. S.; Kall, M. *Nano Lett.,* **2005,** *5*, 2335.

79. Dahlin, A.; Zach, M.; Rindzevicius, T.; Kall, M.; Sutherland, D. S.; Hook, F. *J. Am. Chem. Soc.,* **2005,** *127*, 5043.

80. Jonsson, M. P.; Jonsson, P.; Dahlin, A. B.; Hook, F. *Nano Letters,* **2007,** *7*, 3462.

81. Yonzon, C. R.; Stuart, D. A.; Zhang, X. Y.; McFarland, A. D.; Haynes, C. L.; Van Duyne, R. P. *Talanta,* **2005,** *67*, 438.

82. Malinsky, M. D.; Kelly, K. L.; Schatz, G. C.; Van Duyne, R. P. *Journal of The American Chemical Society,* **2001,** *123*, 1471.

83. Smith, E. A.; Corn, R. M. *Appl. Spectrosc.,* **2003,** *57*, 320A.

84. Brockman, J. M.; Nelson, B. P.; Corn, R. M. *Annu. Rev. Phys. Chem.,* **2000,** *51*, 41.

85. Endo, T.; Kerman, K.; Nagatani, N.; Takamura, Y.; Tamiya, E. *Anal. Chem.,* **2005,** *77*, 6976.

86. Berger, C. E. H.; Beumer, T. A. M.; Kooyman, R. P. H.; Greve, J. *Anal. Chem.,* **1998,** *70*, 703.

87. Raschke, G.; Kowarik, S.; Franzl, T.; Sonnichsen, C.; Klar, T. A.; Feldmann, J.; Nichtl, A.; Kurzinger, K. *Nano Letters,* **2003,** *3*, 935.

88. Nie, S. M.; Emery, S. R. *Science,* **1997,** *275*, 1102.

89. Pipino, A. C. R.; Schatz, G. C.; Vanduyne, R. P. *Phys. Rev. B,* **1994,** *49*, 8320.

90. Pipino, A. C. R.; VanDuyne, R. P.; Schatz, G. C. *Phys. Rev. B,* **1996,** *53*, 4162.

91. Srituravanich, W.; Fang, N.; Sun, C.; Luo, Q.; Zhang, X. *Nano Letters,* **2004,** *4*, 1085.

92. Sundaramurthy, A.; Schuck, P. J.; Conley, N. R.; Fromm, D. P.; Kino, G. S.; Moerner, W. E. *Nano Letters,* **2006,** *6*, 355.

93. Haes, A. J.; Van Duyne, R. P. *Anal. Bioanal. Chem.,* **2004,** *379*, 920.

94. Zhao, J.; Zhang, X. Y.; Yonzon, C. R.; Haes, A. J.; Van Duyne, R. P. *Nanomedicine,* **2006,** *1*, 219.

95. Frederix, F.; Friedt, J. M.; Choi, K. H.; Laureyn, W.; Campitelli, A.; Mondelaers, D.; Maes, G.; Borghs, G. *Anal. Chem.,* **2003,** *75*, 6894.

96. Homola, J.; Yee, S. S.; Gauglitz, G. *Sens. Actuator B-Chem.,* **1999,** *54*, 3.

97. Hoffmann, M. R.; Martin, S. T.; Choi, W. Y.; Bahnemann, D. W. *Chem. Rev.,* **1995,** *95*, 69.

98. Nishimoto, S.; Ohtani, B.; Kajiwara, H.; Kagiya, T. *Journal of The Chemical Society-Faraday Transactions I,* **1983,** *79*, 2685.

99. Shchukin, D.; Ustinovich, E.; Sviridov, D.; Pichat, P. *Photochem. Photobiol. Sci.,* **2004,** *3*, 142.

100. Szabo-Bardos, E.; Czili, H.; Horvath, A. *J. Photochem. Photobiol. A-Chem.,* **2003,** *154*, 195.

101. Litter, M. I. *Appl. Catal. B-Environ.,* **1999,** *23*, 89.

102. Sahyun, M. R. V.; Serpone, N. *Langmuir,* **1997,** *13*, 5082.

103. Castellana, E. T.; Kataoka, S.; Albertorio, F.; Cremer, P. S. *Anal. Chem.,* **2006,** *78*, 107.

104. Green, R. J.; Frazier, R. A.; Shakesheff, K. M.; Davies, M. C.; Roberts, C. J.; Tendler, S. J. B. *Biomaterials,* **2000,** *21*, 1823.

105. Homola, J. *Anal. Bioanal. Chem.,* **2003,** *377*, 528.

106. Roy, D.; Fendler, J. *Advanced Materials,* **2004,** *16*, 479.

107. Rothenhausler, B.; Knoll, W. *Nature,* **1988,** *332*, 615.

108. Nelson, B. P.; Grimsrud, T. E.; Liles, M. R.; Goodman, R. M.; Corn, R. M. *Anal. Chem.,* **2001,** *73*, 1.

109. Shumaker-Parry, J. S.; Aebersold, R.; Campbell, C. T. *Anal. Chem.,* **2004,** *76*, 2071.

110. Wolf, L. K.; Fullenkamp, D. E.; Georgiadis, R. M. *Journal of The American Chemical Society,* **2005,** *127*, 17453.

111. Phillips, K. S.; Wilkop, T.; Wu, J. J.; Al-Kaysi, R. O.; Cheng, Q. *Journal of The American Chemical Society,* **2006,** *128*, 9590.

112. Okamoto, T.; Yamaguchi, I.; Kobayashi, T. *Opt. Lett.,* **2000,** *25*, 372.

113. Kalyuzhny, G.; Vaskevich, A.; Ashkenasy, G.; Shanzer, A.; Rubinstein, I. *J. Phys. Chem. B,* **2000,** *104*, 8238.

114. Nath, N.; Chilkoti, A. *Anal. Chem.,* **2002,** *74*, 504.

115. Nath, N.; Chilkoti, A. *Anal. Chem.,* **2004,** *76*, 5370.

116. Sherry, L. J.; Jin, R. C.; Mirkin, C. A.; Schatz, G. C.; Van Duyne, R. P. *Nano Letters,* **2006,** *6*, 2060.

117. Kreibig, U.; Vollmer, M., *Optical Properties of Metal Clusters*. Springer-Verlag: Heidelberg, Germany, 1995; Vol. 25.

118. Kalyuzhny, G.; Vaskevich, A.; Schneeweiss, M. A.; Rubinstein, I. *Chem.-Eur. J.,* **2002,** *8*, 3850.

119. Doron-Mor, I.; Cohen, H.; Barkay, Z.; Shanzer, A.; Vaskevich, A.; Rubinstein, I. *Chem.-Eur. J.,* **2005,** *11*, 5555.

120. Kalyuzhny, G.; Schneeweiss, M. A.; Shanzer, A.; Vaskevich, A.; Rubinstein, I. *Journal of The American Chemical Society,* **2001,** *123*, 3177.

121. Hutter, E.; Pileni, M. P. *J. Phys. Chem. B,* **2003,** *107*, 6497.

122. Spadavecchia, J.; Prete, P.; Lovergine, N.; Tapfer, L.; Rella, R. *J. Phys. Chem. B,* **2005,** *109*, 17347.

123. Tokareva, I.; Minko, S.; Fendler, J. H.; Hutter, E. *Journal of The American Chemical Society,* **2004,** *126*, 15950.

124. Zhang, F. X.; Guan, N. J.; Li, Y. Z.; Zhang, X.; Chen, J. X.; Zeng, H. S. *Langmuir,* **2003,** *19*, 8230.

125. Liao, W. S.; Yang, T. L.; Castellana, E. T.; Kataoka, S.; Cremer, P. S. *Advanced Materials,* **2006,** *18*, 2240.

126. Stathatos, E.; Lianos, P.; Falaras, P.; Siokou, A. *Langmuir,* **2000,** *16*, 2398.

127. He, J. H.; Ichinose, I.; Fujikawa, S.; Kunitake, T.; Nakao, A. *Chem. Commun.,* **2002**, 1910.

128. Zakrzewska, K.; Radecka, M.; Kruk, A.; Osuch, W. *Solid State Ion.,* **2003,** *157*, 349.

129. Kelly, K. L.; Coronado, E.; Zhao, L. L.; Schatz, G. C. *J. Phys. Chem. B,* **2003,** *107*, 668.

130. Sosa, I. O.; Noguez, C.; Barrera, R. G. *J. Phys. Chem. B,* **2003,** *107*, 6269.

131. Zeman, E. J.; Schatz, G. C. *J. Phys. Chem.,* **1987,** *91*, 634.

132. Jin, R. C.; Cao, Y. C.; Hao, E. C.; Metraux, G. S.; Schatz, G. C.; Mirkin, C. A. *Nature,* **2003,** *425*, 487.

133. Sun, Y. G.; Xia, Y. N. *Advanced Materials,* **2003,** *15*, 695.

134. Jin, R. C.; Cao, Y. W.; Mirkin, C. A.; Kelly, K. L.; Schatz, G. C.; Zheng, J. G. *Science,* **2001,** *294*, 1901.

135. Perez-Luna, V. H.; O'Brien, M. J.; Opperman, K. A.; Hampton, P. D.; Lopez, G. P.; Klumb, L. A.; Stayton, P. S. *Journal of The American Chemical Society,* **1999,** *121*, 6469.

136. Smith, E. A.; Thomas, W. D.; Kiessling, L. L.; Corn, R. M. *Journal of The American Chemical Society,* **2003,** *125*, 6140.

137. Jung, L. S.; Nelson, K. E.; Stayton, P. S.; Campbell, C. T. *Langmuir,* **2000,** *16*, 9421.

138. Nelson, K. E.; Gamble, L.; Jung, L. S.; Boeckl, M. S.; Naeemi, E.; Golledge, S. L.; Sasaki, T.; Castner, D. G.; Campbell, C. T.; Stayton, P. S. *Langmuir,* **2001,** *17*, 2807.

139. Chilkoti, A.; Stayton, P. S. *Journal of The American Chemical Society,* **1995,** *117*, 10622.

140. Dandliker, R.; Gray, S.; Clube, F.; Herzig, H. P.; Volkel, R. *Microelectron. Eng.,* **1995,** *27*, 205.

141. Gale, M. T.; Rossi, M.; Pedersen, J.; Schutz, H. *Opt. Eng.,* **1994,** *33*, 3556.

142. Wu, M. H.; Whitesides, G. M. *Appl. Phys. Lett.,* **2001,** *78*, 2273.

143. Wu, M. H.; Paul, K. E.; Whitesides, G. M. *Appl. Optics,* **2002,** *41*, 2575.

144. Guo, Q. J.; Teng, X. W.; Yang, H. *Nano Letters,* **2004,** *4*, 1657.

145. Deegan, R. D.; Bakajin, O.; Dupont, T. F.; Huber, G.; Nagel, S. R.; Witten, T. A. *Nature,* **1997,** *389*, 827.

146. Deegan, R. D. *Physical Review E,* **2000,** *61*, 475.

147. Deegan, R. D.; Bakajin, O.; Dupont, T. F.; Huber, G.; Nagel, S. R.; Witten, T. A. *Physical Review E,* **2000,** *62*, 756.

148. Rabani, E.; Reichman, D. R.; Geissler, P. L.; Brus, L. E. *Nature,* **2003,** *426*, 271.

149. Hong, S. W.; Xu, J.; Xia, J. F.; Lin, Z. Q.; Qiu, F.; Yang, Y. L. *Chemistry of Materials,* **2005,** *17*, 6223.

150. Xu, J.; Xia, J. F.; Hong, S. W.; Lin, Z. Q.; Qiu, F.; Yang, Y. L. *Physical Review Letters,* **2006,** *96*.

151. Hong, S. W.; Xu, J.; Lin, Z. Q. *Nano Letters,* **2006,** *6*, 2949.

152. Kim, E.; Xia, Y. N.; Zhao, X. M.; Whitesides, G. M. *Advanced Materials,* **1997,** *9*, 651.

153. Deckman, H. W.; Dunsmuir, J. H. *Appl. Phys. Lett.,* **1982,** *41*, 377.

154. Deckman, H. W.; Dunsmuir, J. H. *J. Vac. Sci. Technol. B,* **1983,** *1*, 1109.

155. Nguyen, V. X.; Stebe, K. J. *Physical Review Letters,* **2002,** *88*.

156. Yabu, H.; Shimomura, M. *Advanced Functional Materials,* **2005,** *15*, 575.

157. Liao, W. S.; Chen, X.; Chen, J.; Cremer, P. S. *Nano Lett.,* **2007,** *7*, 2452.

158. Sefiane, K. *Journal of Colloid and Interface Science,* **2004,** *272*, 411.

159. Dugas, V.; Broutin, J.; Souteyrand, E. *Langmuir,* **2005,** *21*, 9130.

160. Deng, Y.; Zhu, X. Y.; Kienlen, T.; Guo, A. *Journal of the American Chemical Society,* **2006,** *128*, 2768.

161. Edmonstone, B. D.; Matar, O. K. *Journal of Colloid and Interface Science,* **2004,** *274*, 183.

162. Pierce, S. M.; Chan, K. B.; Zhu, H. P. *Journal of Agricultural and Food Chemistry,* **2008,** *56*, 213.

163. Chandra, S.; diMarzo, M.; Qiao, Y. M.; Tartarini, P. *Fire Safety Journal,* **1996,** *27*, 141.

164. Warner, M. R. E.; Craster, R. V.; Matar, O. K. *Physics of Fluids,* **2004,** *16*, 2933.

165. Stewart, M. E.; Anderton, C. R.; Thompson, L. B.; Maria, J.; Gray, S. K.; Rogers, J. A.; Nuzzo, R. G. *Chem. Rev.,* **2008,** *108*, 494.

166. Liao, W. S.; Chen, X.; Shi, J.; Chen, J.; Pace, H. P.; Cremer, P. S. *In preparation,* **2009**.

167. Chen, J. X.; Liao, W. S.; Chen, X.; Yang, T. L.; Wark, S. E.; Son, D. H.; Batteas, J. D.; Cremer, P. S. *ACS Nano,* **2009,** *3*, 173.

168. Genet, C.; Ebbesen, T. W. *Nature,* **2007,** *445*, 39.

169. Alaverdyan, Y.; Sepulveda, B.; Eurenius, L.; Olsson, E.; Kall, M. *Nat. Phys.,* **2007,** *3*, 884.

170. Stewart, M. E.; Mack, N. H.; Malyarchuk, V.; Soares, J.; Lee, T. W.; Gray, S. K.; Nuzzo, R. G.; Rogers, J. A. *Proc. Natl. Acad. Sci. U. S. A.,* **2006,** *103*, 17143.

171. Brolo, A. G.; Gordon, R.; Leathem, B.; Kavanagh, K. L. *Langmuir,* **2004,** *20*, 4813.

172. Yao, J. M.; Stewart, M. E.; Maria, J.; Lee, T. W.; Gray, S. K.; Rogers, J. A.; Nuzzo, R. G. *Angew. Chem.-Int. Edit.,* **2008,** *47*, 5013.

173. Ebbesen, T. W.; Lezec, H. J.; Ghaemi, H. F.; Thio, T.; Wolff, P. A. *Nature,* **1998,** *391*, 667.

174. Barnes, W. L.; Murray, W. A.; Dintinger, J.; Devaux, E.; Ebbesen, T. W. *Phys. Rev. Lett.,* **2004,** *92*.

175. Degiron, A.; Ebbesen, T. W. *J. Opt. A-Pure Appl. Opt.,* **2005,** *7*, S90.

176. Lezec, H. J.; Thio, T. *Opt. Express,* **2004,** *12*, 3629.

177. Krishnan, A.; Thio, T.; Kima, T. J.; Lezec, H. J.; Ebbesen, T. W.; Wolff, P. A.; Pendry, J.; Martin-Moreno, L.; Garcia-Vidal, F. J. *Opt. Commun.,* **2001,** *200*, 1.

178. Ghaemi, H. F.; Thio, T.; Grupp, D. E.; Ebbesen, T. W.; Lezec, H. J. *Physical Review B-Condensed Matter,* **1998,** *58*, 6779.

179. Baida, F. I.; Van Labeke, D. *Opt. Commun.,* **2002,** *209*, 17.

180. Chang, S. H.; Gray, S. K.; Schatz, G. C. *Opt. Express,* **2005,** *13*, 3150.

181. Lin, L.; Reeves, R. J.; Blaikie, R. J. *Phys. Rev. B,* **2006,** *74*.

182. Liu, H. T.; Lalanne, P. *Nature,* **2008,** *452*, 728.

183. Brolo, A. G.; Arctander, E.; Gordon, R.; Leathem, B.; Kavanagh, K. L. *Nano Lett.,* **2004,** *4*, 2015.

184. Brolo, A. G.; Kwok, S. C.; Cooper, M. D.; Moffitt, M. G.; Wang, C. W.; Gordon, R.; Riordon, J.; Kavanagh, K. L. *J. Phys. Chem. B,* **2006,** *110*, 8307.

185. Sharpe, J. C.; Mitchell, J. S.; Lin, L.; Sedoglavich, H.; Blaikie, R. J. *Anal. Chem.,* **2008,** *80*, 2244.

186. Kim, J. H.; Moyer, P. J. *Opt. Express,* **2006,** *14*, 6595.

187. Brolo, A. G.; Kwok, S. C.; Moffitt, M. G.; Gordon, R.; Riordon, J.; Kavanagh, K. L. *J. Am. Chem. Soc.,* **2005,** *127*, 14936.

188. Gordon, R.; Brolo, A. G.; McKinnon, A.; Rajora, A.; Leathem, B.; Kavanagh, K. L. *Phys. Rev. Lett.,* **2004,** *92*.

189. Wang, Q. J.; Li, J. Q.; Huang, C. P.; Zhang, C.; Zhu, Y. Y. *Appl. Phys. Lett.,* **2005,** *87*.

190. Henzie, J.; Lee, M. H.; Odom, T. W. *Nat. Nanotechnol.,* **2007,** *2*, 549.

191. Ctistis, G.; Papaioannou, E.; Patoka, P.; Gutek, J.; Fulnagalli, P.; Giersig, M. *Nano Lett.,* **2009,** *9*, 1.

192. Ctistis, G.; Patoka, P.; Wang, X.; Kempa, K.; Giersig, M. *Nano Lett.,* **2007,** *7*, 2926.

193. de Abajo, F. J. G. *Rev. Mod. Phys.,* **2007,** *79*, 1267.

194. Chen, Y. G.; Wang, Y. H.; Zhang, Y.; Lu, S. T. *Opt. Commun.,* **2007,** *274*, 236.

195. Gao, H. W.; Henzie, J.; Odom, T. W. *Nano Lett.,* **2006,** *6*, 2104.

196. Park, T. H.; Mirin, N.; Lassiter, J. B.; Nehl, C. L.; Halas, N. J.; Nordlander, P. *ACS Nano,* **2008,** *2*, 25.

197. Kocabas, A.; Dana, A.; Aydinli, A. *Appl. Phys. Lett.,* **2006,** *89*.

198. Chan, G. H.; Zhao, J.; Schatz, G. C.; Duyne, R. P. V. *J. Phys. Chem. C,* **2008,** *112*, 13958.

199. Thio, T.; Ghaemi, H. F.; Lezec, H. J.; Wolff, P. A.; Ebbesen, T. W. *J. Opt. Soc. Am. B-Opt. Phys.,* **1999,** *16*, 1743.

200. Jain, P. K.; El-Sayed, M. A. *Nano Lett.,* **2008,** *8*, 4347.

201. Sambles, J. R.; Bradbery, G. W.; Yang, F. Z. *Contemp. Phys.,* **1991,** *32*, 173.

VITA

Name: Wei-Ssu Liao

Address: Department of Chemistry, Texas A&M University,

College Station TX 77843-3012

Email Address: wsliao@mail.chem.tamu.edu

Education: B.S., National Cheng Kung University, Taiwan, 2000

M.S., National Taiwan University, Taiwan, 2002

Ph.D., Texas A&M University, TX, 2009